

2017

Enhancing Wireless Received Signal Strength-based Indoor Location Systems

Li, Yuqi

Li, Y. (2017). Enhancing Wireless Received Signal Strength-based Indoor Location Systems (Doctoral thesis, University of Calgary, Calgary, Canada). Retrieved from <https://prism.ucalgary.ca>. doi:10.11575/PRISM/25912

<http://hdl.handle.net/11023/3718>

Downloaded from PRISM Repository, University of Calgary

UNIVERSITY OF CALGARY

Enhancing Wireless Received Signal Strength-based Indoor Location Systems

by

Yuqi Li

A THESIS

SUBMITTED TO THE FACULTY OF GRADUATE STUDIES
IN PARTIAL FULFILMENT OF THE REQUIREMENTS FOR THE
DEGREE OF DOCTOR OF PHILOSOPHY

GRADUATE PROGRAM IN ELECTRICAL AND COMPUTER ENGINEERING

CALGARY, ALBERTA

APRIL, 2017

© Yuqi Li 2017

Abstract

The ever-growing demand for Location Based Services has significantly boosted the research and development need for indoor positioning systems. Of various indoor positioning solutions, techniques making use of Received Signal Strength (RSS) of wireless signals of opportunity have gained extensive interest due to the ubiquitous wireless signal infrastructure and the readily available RSS measurements with standard mobile devices. However, the performance of RSS-based indoor positioning systems is highly affected by significant uncertainties in RSS due to many factors affecting wireless propagations. To enhance the performance of an RSS-based indoor positioning system, from a Bayesian filtering theory perspective, a better estimation of the a posteriori distribution of position is needed. This can be done through a better modelling of RSS measurements to mitigate uncertainties and/or incorporating prior information. This thesis specifically explores mitigating RSS uncertainties by modelling those due to human body shadowing and incorporating prior information from widely available security cameras and building maps.

The characterization of RSS measurements indoors is first demonstrated using data collected in various environments. Experimental results characterize the RSS sensitivity to location and the uncertainty incurred by body shadowing effects on RSS measurements.

Based on the characterization, an empirical model with a small number of parameters estimated from training data is proposed to model the RSS loss due to body shadowing. An estimator based on this model is proposed to improve positioning. Experimental results show that when the user heading is known, the positioning obviously improves. When the heading is unknown, and thus needs to be jointly estimated, the improvement becomes less apparent.

This thesis then investigates the use of security cameras and building maps to enhance RSS-based positioning. An estimator based on computer vision processing is proposed to estimate user's heading in corridors. Based on this, a camera-aided RSS system based on Kalman-filter is proposed and it is experimentally shown that a 37.5% improvement in horizontal position estimation occurs. To further incorporate building map information, a map-camera-aided RSS system based on particle filters is proposed. Experimental results indicate that the use of map constraints further bring 44.4% improvement in the across track direction.

Acknowledgements

First, I would like to express my deepest gratitude to my supervisor, Dr. John Nielsen, for his guidance, support and encouragement during my research. Second, I would like to thank my co-supervisor, Dr. Gérard Lachapelle for his support for my research and providing me with the opportunity to be a part of the prestigious Position Location And Navigation (PLAN) Group.

I would like to thank Dr. Zhe He for his expertise, support and encouragement during my research.

I would like to thank Appropolis Inc. for financial support, experimental system setup and field test data for my research.

I am thankful to my friends and colleagues, Zhixing Zhao, You Li, Ngon Le, Ammar Al Masri, Yasser Abdelhamed, Ali Saleh, Sina Arman Rezai and Shizheng Chen for all their help during my studies.

Finally and most importantly, I would like to thank my parents and my wife, Yuanyuan, for their unconditional love, understanding and encouragement. This work would not have been possible without their support.

Table of Contents

Abstract	ii
Acknowledgements	iv
Table of Contents	v
List of Tables	viii
List of Figures and Illustrations	ix
List of Symbols, Abbreviations and Nomenclature	xiv
CHAPTER ONE: INTRODUCTION	1
1.1 Background	1
1.1.1 Indoor Positioning Technology	1
1.1.2 Indoor Positioning based on Wireless Received Signal Strength	2
1.1.3 Challenges in Indoor Positioning with RSS Measurements	4
1.1.4 Integration of RSS and other Sensors for Indoor Positioning	7
1.1.5 Incorporating Building Map Information for Indoor Positioning	9
1.2 Limitations of Previous Research	11
1.2.1 RSS Body Shadowing Effects on RSS-based Positioning	11
1.2.2 Integration of RSS with Security Camera and Building Maps for Indoor Positioning	12
1.3 Objective and Contributions	15
1.4 Thesis Outline	17
CHAPTER TWO: BACKGROUND	19
2.1 RSS-based Indoor Positioning	19
2.1.1 IEEE 802.11 Wi-Fi Channel Allocations and RSS Collection Mechanism	20
2.1.2 Fisher Information and Cramer-Rao Lower Bound of RSS for Positioning	22
2.1.2.1 One RSS measurement case	23
2.1.2.2 Multiple RSS measurements case	27
2.1.3 RSS-based Positioning Techniques	29
2.1.3.1 RSS Fingerprinting	30
2.1.3.2 RSS Positioning based on Pathloss Model	31
2.2 Use of Prior Information to Enhance State Estimation in Bayesian Filters	37
2.2.1 Bayesian Filter	38
2.2.2 Kalman Filtering	40
2.2.3 Particle Filtering	42
2.3 Static Camera Positioning and CV Processing for Object Detection	45
2.3.1 Background Subtraction for Object Detection	47
CHAPTER THREE: INDOOR RECEIVED SIGNAL STRENGTH MEASUREMENT CHARACTERIZATION	50
3.1 Experimental Equipment and Environments	50
3.2 Pathloss Characterization	53
3.2.1 Outdoor Experiment for Pathloss Characterization	53
3.2.2 Indoor Experiment for Pathloss Characterization	55

3.3 Body Shadowing Effects on RSS Measurements	60
3.3.1 Human Body Shadowing Effect as a Function of Blocking Distance.....	62
3.3.1.1 Outdoor Experiment for Analysis of Blocking Distance Affecting Body Shadowing.....	62
3.3.1.2 Indoor Experiment for Analysis of Blocking Distance Affecting Body Shadowing.....	64
3.3.2 Human Body Shadowing Effect as a Function of Blocking Angle.....	67
3.3.2.1 Outdoor Experiment for Analysis of Blocking Angle Affecting Body Shadowing.....	67
3.3.2.2 Indoor Experiment for Analysis of Blocking Angle Affecting Body Shadowing.....	68
3.3.2.3 Indoor Experiment with Multiple APs.....	70
3.4 Conclusion	72
 CHAPTER FOUR: ENHANCING RSS BASED INDOOR POSITIONING BY CONSIDERING BODY SHADOWING EFFECTS	
	75
4.1 Empirical RSS Body Shadowing Loss Model	75
4.2 Joint Estimation of Position and Heading using Body Shadowing Loss Model	81
4.2.1 Problem Formulation for Joint Estimation of Position and Heading	82
4.3 Experimental Data Processing and Results	86
4.3.1 Experimental setup and data collection	86
4.3.2 RSS Body Shadowing Loss Distribution at Test Points.....	89
4.3.3 Position Performance Evaluation and Comparison	90
4.3.3.1 Results at one test point	92
4.3.3.2 Results at all test points	100
4.4 Summary	105
 CHAPTER FIVE: ENHANCING RSS-BASED INDOOR POSITIONING WITH SECURITY CAMERAS AND BUILDING MAPS	
	106
5.1 Unaided RSS Positioning System based on Kalman Filtering	107
5.2 Fusing Security Cameras into RSS-based Indoor Positioning System.....	109
5.2.1 Heading Estimation with a Security Camera in Corridors	111
5.2.2 Camera-aided RSS Positioning System based on Kalman Filtering	116
5.2.3 Experimental Setup and Results Analysis.....	124
5.2.3.1 Experiment Setup and Data Collection.....	124
5.2.3.2 Heading Estimation Using CV Object Detection	128
5.2.3.3 Camera-aided RSS Positioning System Enhancement	135
5.3 Fusing Building Map and Security Cameras to Enhance RSS-based Positioning	141
5.3.1 Map Constraint Information Representation	141
5.3.2 Map-camera-aided RSS Positioning System based on Particle Filtering.....	143
5.3.3 Experimental Results and Analysis	147
5.4 Summary	154
 CHAPTER SIX: CONCLUSIONS AND RECOMMENDATIONS	
	155
6.1 Conclusions.....	155

6.2 Recommendations for future work	158
REFERENCES	160

List of Tables

Table 1. IEEE 802.11 physical layer standards (Tektronix, 2013).....	20
Table 4.1: Trained parameters of RSS body shadowing loss model for the test area in Appropolis office	81
Table 4.2 Average RMSE positions over all RPs	104
Table 5.1. Position RMSE for unaided RSS and camera-aided RSS systems.....	140
Table 5.2. Position RMSE for unaided RSS, camera-aided RSS and map-camera-aided RSS systems	153

List of Figures and Illustrations

Figure 1.1: Indoor wireless signal propagations	5
Figure 1.2: Body shadowing effect caused by device user and/or people nearby	6
Figure 1.3: Flow chart of thesis structure	18
Figure 2.1: RSS acquiring in IEEE 802.11 Wi-Fi systems.....	22
Figure 2.2 Two dimensional wireless link	25
Figure 2.3: RSS mean value heat maps of an AP (Li et al 2015)	31
Figure 2.4: Static camera positioning system	46
Figure 2.5: Original image(a) and object detected (b) (Nielsen et al 2016)	49
Figure 3.2: Indoor environments for data collection: hallway in ENA building (top left), hallway in ICT building (top right), hallway in EEEL building (bottom left), Appropolis office (bottom right).....	52
Figure 3.3: Experiment for pathloss characterization	54
Figure 3.4: : Scatter plot, mean, standard deviation of RSS measurements and pathloss model fitted in an outdoor environment (a) 2.4 GHz signals (b) 5 GHz signals	55
Figure 3.5: Scatter plot, mean, standard deviation of RSS measurements and pathloss model fitted in ENA building (a) 2.4 GHz signals (b) 5 GHz signals	56
Figure 3.6: Scatter plot, mean, standard deviation of RSS measurements and pathloss model fitted in ICT building (a) 2.4 GHz signals (b) 5 GHz signals	57
Figure 3.7: Scatter plot, mean, standard deviation of RSS measurements and pathloss model fitted in EEEL building (a) 2.4 GHz signals (b) 5 GHz signals	57
Figure 3.8: Experimental setup for RSS characterization in Appropolis office	58
Figure 3.9: Scatter plot, mean, standard deviation of RSS measurements and pathloss model fitted in Appropolis building (a) 2.4 GHz signals (b) 5 GHz signals	59
Figure 3.10: Histogram of RSS measurements at the location identified by an arrow in Figure 3.8 for (a) 2.4 GHz signals, (b) 5 GHz signals	60
Figure 3.11: Body shadowing effect caused by device user and/or people nearby	61
Figure 3.12: A generalized human body shadowing scenario	62

Figure 3.13: Experiment design for analyzing dependence of RSS body shadowing loss on blocking distance	63
Figure 3.14: Mean and standard deviation of RSS shadowing loss as a function of blocking distance in an outdoor environment (a) 2.4 GHz signals, (b) 5 GHz signals.....	63
Figure 3.15: Mean and standard deviation of RSS shadowing loss as a function of blocking distance in ENA building (a) 2.4 GHz signals, (b) 5 GHz signals	65
Figure 3.16: Mean and standard deviation of RSS shadowing loss as a function of blocking distance in ICT building (a) 2.4 GHz signals, (b) 5 GHz signals	65
Figure 3.17: Mean and standard deviation of RSS shadowing loss as a function of blocking distance in EEL building (a) 2.4 GHz signals, (b) 5 GHz signals	66
Figure 3.18: Experiment for dependence of RSS body shadowing loss on blocking angle	67
Figure 3.19: Mean and standard deviation of 5 GHz RSS shadowing loss as a function of blocking angle in outdoor and indoor environments	68
Figure 3.20: APs and mobile deployment in Appropolis office for body shadowing effect experiments	69
Figure 3.21: Multipath effects on 5 GHz RSS body shadowing loss for different APs	70
Figure 3.22: 5 GHz RSS body shadowing loss versus blocking angle for 11 APs at 3 mobile locations in Appropolis office.....	72
Figure 4.1: Mobile user's body blocks RSS from an AP.....	76
Figure 4.2: Geometry of T-R line, user's heading and blocking angle in (a) 3D scenario (b) 2D scenario	76
Figure 4.3: 5 GHz RSS shadowing loss data versus blocking angle in Appropolis office.....	79
Figure 4.4: RSS shadowing loss model fitted to experimental training data.....	79
Figure 4.5: Position and heading joint estimation using RSS from multiple APs	83
Figure 4.6: Experimental environment in Appropolis office.....	87
Figure 4.7: Test area floor plan, AP setup and test points	88
Figure 4.8: (a) RSS collection without body shadowing (b) RSS collection with user pointing south.....	88

Figure 4.9: RSS body shadowing loss data collected at test points compared to the trained model.....	90
Figure 4.10: Data processing scheme for positioning performance evaluation.....	92
Figure 4.11: Error percentile of positioning errors at TP1, pointing north.....	93
Figure 4.12: RSS body shadowing loss at TP1 with user pointing north	94
Figure 4.13: Sum of square residuals in different test scenarios at TP1, pointing north	95
Figure 4.14: Negative Likelihoods over <i>E-N</i> state space.....	96
Figure 4.15: Minimum negative log-likelihoods over heading state space	98
Figure 4.16: Heading estimate errors at TP1 with user pointing north.....	98
Figure 4.17: Position errors as a function of location (a) pointing north, heading not constrained, (b) pointing south, heading not constrained, (c) pointing north, heading constrained, (d) pointing south, heading constrained	102
Figure 4.18: RSS body shadowing loss at TP2, pointing south.....	103
Figure 4.19: Error percentile of positioning errors at TP2, pointing south.....	103
Figure 4.20: Error percentile of positioning errors of all TPs.....	104
Figure 5.1: Unaided RSS positioning system	108
Figure 5.2: Security camera setup in a corridor (a) 2D depiction (b) 3D depiction	112
Figure 5.3: (a) A person captured by camera (b) Object detection result.....	112
Figure 5.4: Bounding box (green) and ground touch point (red) of a detected object	115
Figure 5.5: Camera-aided RSS positioning system	117
Figure 5.6: Reference trajectory, position observations, unaided RSS Kalman filtering position estimates and camera-aided RSS Kalman filtering position estimates in local coordinates	119
Figure 5.7 Reference heading, unaided RSS and camera-aided RSS heading estimates	120
Figure 5.8: Updated variances of position state in west-east direction.....	122
Figure 5.9: Updated variances of position state in south-north direction, as well as heading estimates of camera-aided RSS system.....	122

Figure 5.10: Position errors in (a) west-east direction (cross track) and (b) south-north direction (along track).....	123
Figure 5.11: Position error percentiles in (a) west-east direction (cross track) and (b) south-north direction (along track)	124
Figure 5.12: (a) Experimental environment in field of view of a security camera (b) a security camera	125
Figure 5.13: Floor plan, experimental setup and test route reference.....	126
Figure 5.14: Method to obtain position reference solution.....	128
Figure 5.15: CV object detection results: (top left) good detection, (top right) detection with considerable error, (bottom left) false detection, (bottom right) missed detection.....	129
Figure 5.16: Object detected in image v axis by camera during the first 105 seconds	130
Figure 5.17: RMES and availability of heading estimates versus threshold of pixel change rate.....	132
Figure 5.18: Object detected in image v axis for three cases and heading estimates: (a) heading obtained correctly, (b) low pixel change rate carrying no heading information, (c) heading obtained wrongly due to outliers.....	132
Figure 5.19: Heading estimation errors and root of normalized SSR.....	134
Figure 5.20: RMSE and availability of heading estimates versus threshold of root of mean SSR	134
Figure 5.21: Heading state tracked in camera-aided RSS system	136
Figure 5.22: Position results of unaided RSS and camera-aided RSS systems	138
Figure 5.23: Position for unaided RSS and camera-aided RSS systems (a) errors in west-east (cross track), (b) errors in south-north (along track) and (c) horizontal errors	139
Figure 5.24: Position performance of unaided RSS and camera-aided RSS systems (a) errors in west-east (cross track), (b) errors in south-north (along track) and (c) horizontal errors	140
Figure 5.25: (a) Floor plan and (b) map constraints (polygons with different outline colors represent different regions)	142
Figure 5.26: Map-camera-aided RSS positioning system based on particle filtering.....	144
Figure 5.27: Position particle distribution and estimated positions (a) without map constraints and (b) with map constraints.....	148

Figure 5.28: Position for camera-aided RSS and map-camera-aided RSS systems (a) errors in west-east (cross track), (b) errors in south-north (along track) and (b) horizontal errors... 151

Figure 5.29: Position error percentiles of unaided RSS, camera-aided RSS and map-camera-aided systems (a) error percentiles in west-east (cross track), (b) error percentiles in south-north (along track) and (c) horizontal error percentiles 152

Figure 5.30: Position results of camera-aided RSS and map-camera-aided RSS systems 153

List of Symbols, Abbreviations and Nomenclature

Symbol	Definition
a	Decay rate in RSS body shadowing loss model
α	Elevation angle
$bel(\bullet)$	Belief or a posteriori distribution of state in Bayesian filter
$\overline{bel}(\bullet)$	Prediction of state in Bayesian filter
β	Body shadowing blocking angle
d	Transmitter-Receiver distance
D_p	Dilution of Precision
E, N	Position in east and north
\mathbf{H}	Observation matrix
J	Fisher information
\mathbf{J}	Fisher information matrix
k	Pixel change rate in image pixel plane v axis
$L(\bullet)$	Loss function
L_x	Log-likelihood function of \mathbf{x}
m_{RSS}	Mean value of RSS measurements
n	Exponent of pathloss model
N_{eff}	Effective number of particle in particle filter
$p(\bullet)$	Probability density function
P_r	Received power in linear unit
P_0	Received power in linear unit at 1 m from transmitter
\mathbf{p}_m	Position of the m th access point
\mathbf{p}	Position of mobile device
\mathbf{P}	Covariance matrix of a state vector in Kalman filter
\mathbf{R}	Measurement covariance matrix in Kalman filter
\mathbf{Q}	Covariance matrix
r	Received Signal Strength in dBm
\mathbf{r}	Received signal strength vector in dBm
\mathbf{r}_{res}	Measurement residual vector
\mathbf{u}, \mathbf{v}	Axes of image pixel coordinate
v_E, v_N	Velocity in east and north
w	Noise or uncertainty
\mathbf{w}	Noise vector
\mathbf{x}	State vector
\mathbf{x}_{ML}	Maximum likelihood estimator of state \mathbf{x}
\mathbf{z}	Measurement vector
σ	Standard deviation of a random variable

θ	User's heading
Θ	Parameter vector
$\Phi_{k-1,k}$	State transition matrix in Kalman filter
χ	A particle set
ω_n^t	Weight of the n th particle at time t
$\delta(\bullet)$	Dirac function
η	Received signal strength loss due to body shadowing effect

Abbreviation	Definition
AOA	Angle-of-Arrival
AP	Access Point
BGS	Background Subtraction
BSSID	Basic Service Set Identifier
CRLB	Cramer-Rao Lower Bound
CV	Computer Vision
FI	Fisher Information
FOV	Field of View
GNSS	Global Navigation Satellite System
GTP	Ground Touching Point
IMU	Inertial Measurement Unit
ISM	Industrial, Scientific and Medical
LOS	Line-of-Sight
LS	Least Square
MAP	Maximum a Posteriori
MLE	Maximum Likelihood Estimator
MVU	Minimum Variance Unbiased
NLOS	Non-Line-of-Sight
PDF	Probability Density Function
PDR	Pedestrian Dead Reckoning
RMSE	Root Mean Square Error
RP	Reference Point
RTLS	Real-Time Location System
SSID	Service Set Identifier
SSR	Sum of Square Residual
TDOA	Time-Difference-of-Arrival
TOA	Time-of-Arrival
TP	Test Point
T-R	Transmitter-Receiver

Chapter One: Introduction

1.1 Background

1.1.1 Indoor Positioning Technology

There has been increasing interest in Location Based Services (LBS) for the past decade. The LBS exploits the ability of current navigation technology to obtain a person's location and provide services such as personal navigation, people tracking, smart retail, medical alerts, workforce management, etc. (Barcelo et al 2006). Since positioning systems and technologies are fundamental for LBS, the ever-growing demand in the past decade has significantly boosted the research and development of seamless outdoor and indoor positioning systems in both academia and industry. The ultimate objective of a positioning system is to provide continuous, reliable and accurate positioning solutions to support LBS (Xiao et al 2014).

While a Global Navigation Satellite System (GNSS) meets the requirements of most outdoor positioning applications, it generally provides an unsatisfactory solution for indoor positioning due to poor signal reception, multipath fading and high variability of the indoor propagation channel. Therefore, alternative indoor positioning systems and technologies have drawn extensive research and development. So far, there are currently over 150 companies involved in Real-Time Location System (RTLS), indoor tracking and other indoor pedestrian applications (Li, 2015). Various techniques have been proposed for indoor positioning. Some typical indoor positioning solutions include cell of origin method with Bluetooth beacons (Aalto et al 2004), pathloss-based positioning with Wi-Fi Access Points (APs) (Langendoen and Reijers, 2003), fingerprinting with Wi-Fi APs and/or magnetometers (Bahl and Padmanabhan, 2000, King et al 2006, Li et al 2015), pedestrian dead-reckoning using Inertial Measurement Units (IMU) (Jimenez et al 2009), vision-aided tracking by incorporating cameras (Van den Berghe et al

2011), integration with high sensitivity Global Navigation Satellite System (GNSS) receivers (He et al 2013, He et al 2014), etc. However, there is apparently no single predominant solution that is able to perform satisfactorily in most indoor environments. Many solutions are proposed based on the integration of disparate sensors resulting in a diversity of measurements, but hitherto no clear solution has emerged as a generalized satisfactory solution for indoor positioning.

1.1.2 Indoor Positioning based on Wireless Received Signal Strength

Today, wireless signals are ubiquitous in most indoor environments. For example, the IEEE 802.11 Wi-Fi network infrastructure is widely deployed in hotels, hospitals, airports, train stations, office buildings, etc. Indoor positioning with wireless signals has become very popular in the past decade (Liu et al 2007). A detailed wireless indoor positioning technique can be found in Gu et al (2009). In general, the most commonly used measurements in wireless positioning include Time-of-Arrival (TOA) (Peterson et al 1998), Time-Difference-of-Arrival (TDOA) (Li et al 2000), Angle-of-Arrival (AOA) (Stoica and Moses, 1997) and Received Signal Strength (RSS). Since the range from a transmitter to a receiver is directly proportional to the propagation time, the TOA technique uses the ranges from transmitters to mobile devices for positioning, while for TDOA, the relative distance from a mobile to the transmitters is used. In general, the use of TOA and TDOA results in increasing the complexity of a positioning system: all transmitters and receivers in the system must be synchronized (TOA); or all transmitters have to be synchronized (TDOA). In an AOA positioning system, the intersection of several pairs of angle direction lines are used to locate a target (Liu et al 2007). However, directional antennae or array antennae are required to obtain AOA measurements, which also increase the complexity of

a positioning system. On the contrary, RSS is a simple measurement to make, as no synchronization is required and only the signal magnitude is needed. Also, wireless signal RSS measurements are supplied by wireless receivers as a by-product of the processing required to facilitate data communications and hence are readily available in most wireless receivers (Nielsen and Nielsen, 2016). Therefore, indoor positioning making use of wireless signal RSS has become the most widespread approach. Today, many companies provide their indoor positioning and navigation solutions based on wireless systems including Skyhook, Ekahau, Cisco, Ericsson, Qualcomm Atheros, WiFiSLAM/Apple, CSR/Broadcom, to name a few (Li, 2015).

In general, RSS positioning techniques fall into three categories: cell of origin, pathloss-based methods and map-based methods (fingerprinting) (Mautz, 2012). The “cell of origin” is a straightforward method where the location of the transmitter (e.g., Wi-Fi AP, Bluetooth beacon) with the highest RSS value is used as the location of the mobile device, reducing the positioning method from a 2D to a 1D approach. Cell of origin methods thus only provide very coarse positions. Fingerprinting techniques localize a mobile by pattern-matching RSS measurements with an RSS offline database using deterministic or probabilistic models (Honkavirta et al 2009, Li et al 2015). The positioning performance of fingerprinting relies on an accurate database which is obtained by laborious offline pre-surveys and/or complex crowdsourcing. On the other hand, pathloss-based techniques estimate signal RSS propagation from the mobile device to a set of transmitters with known locations using pathloss models, and then estimate the location of the mobile device using methods such as a trilateration algorithm (Langendoen and Reijers, 2003). Generally speaking, trilateration determines the mobile locations as the intersection of a set of circles in 2D, where each circle is centered at the coordinate of a transmitter with radius being

the range from the transmitter to the mobile. The parameters of the pathloss model are environment-dependent and need to be trained in an offline stage, in which less labor is needed as compared to that in fingerprinting, due to the use of a model to characterize wireless channels. The details of the pathloss-based methods will be reviewed in Chapter 2 and the pathloss-based methods will be used throughout the thesis to assess various algorithms proposed to enhance an RSS-based positioning system. In general, positioning performance of fingerprinting is better than that of the pathloss-based algorithms due to an extensive pre-survey for characterizing the complicated indoor wireless channels; however, combinations of pathloss-based algorithms with other sensors can improve positioning performance while avoiding the laborious pre-survey required by fingerprinting.

According to the RSS positioning techniques introduced above, it is obvious that the effectiveness of the RSS positioning relies on the consistency of the RSS measurements with the model or database. Therefore, the main challenge of the RSS positioning is the significant noise uncertainty in RSS measurements, which will be discussed next.

1.1.3 Challenges in Indoor Positioning with RSS Measurements

There are many factors which can affect the electromagnetic coupling between the transmitter and receiver antennae and cause significant uncertainty in RSS measurements, which have proven to be a major challenge in RSS-based indoor positioning systems. Figure 1.1 depicts an example of a wireless signal propagation scenario in indoor environments. While a user device may receive a signal directly from the transmitter which is the Line-of-Sight (LOS) signal, signals from penetrated, reflected, diffracted and scattered paths will also reach the user device with different arrival times, amplitudes and arrival angles, which is the multipath scenario (Li,

2014). The small scale fading caused by multipath is a well-known challenge for wireless positioning including RSS-based positioning (Krishnakumar and Krishnan, 2005). In addition to multipath, other factors can introduce uncertainty to RSS including internal structure changes of a building, displacement of furniture (Chen et al 2005), different RSS readings made by different wireless receiver chipsets (Lui et al 2011), opened/closed doors (Chen et al 2005), varying humidity levels (Chen et al 2005), changing attitude of receiver antennae (Xiang et al 2004, Della Rosa et al 2011), human hand-grip effects (Della Rosa et al 2011, Della Rosa et al 2012) and absence/presence of human body blockage (shadowing) in the signal propagation path (Bahl and Padmanabhan, 2000, King et al 2006, Della Rosa et al 2012, Schmitt et al 2014). Some sources of uncertainty in RSS could be addressed by routinely repeating calibrations to update the RSS pathloss model or database (e.g., internal structure changes of a building), however, some sources of uncertainty are highly dynamic, such as human body shadowing, and lead to significant signal strength fluctuation during positioning, which has shown to be a major problem when trying to improve RSS based positioning system performance.

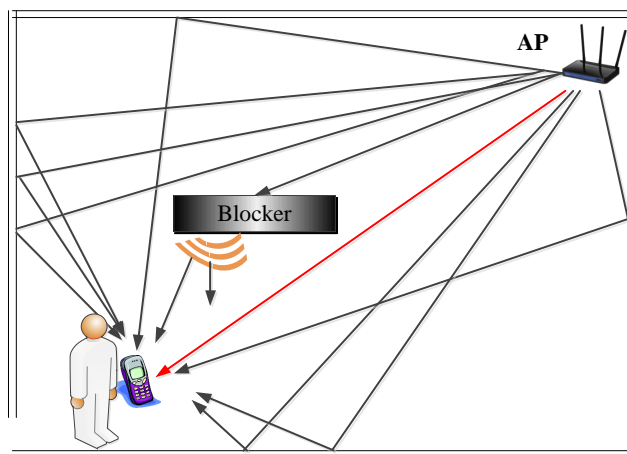


Figure 1.1: Indoor wireless signal propagations

Figure 1.2 depicts the body shadowing scenarios during positioning: a user tries to self-locate by receiving signals from APs using a mobile. As the user moves around and changes heading, the body of the user and/or people nearby may block the direct signal propagation path and hence affects the RSS reading. Human body shadowing effects on RSS positioning system based on Wi-Fi network have gained much research interest. Most current Wi-Fi AP devices transmit signals over the 2.4 GHz and 5 GHz frequency bands simultaneously. Many researchers have studied the blocking effect on the 2.4 GHz band (Chen et al 2005, King et al 2006, Li et al 2015, Amani et al 2016). Research into exploiting the 5 GHz signal RSS for positioning is on-going and needed and some publications (Farshad et al 2013, Yu et al 2014) provide evidence of lower RSS variations at 5 GHz than at 2.4 GHz. Therefore, it is of interest to investigate the RSS body blocking loss for the 5 GHz signal for positioning purpose. One main focus of this thesis is to characterize the human body shadowing effects on both Wi-Fi 2.4 GHz and 5 GHz RSS and to investigate the possibility of modeling and mitigation of the uncertainty in RSS due to this effect for positioning. Relevant research and limitations will be discussed in Section 1.2.

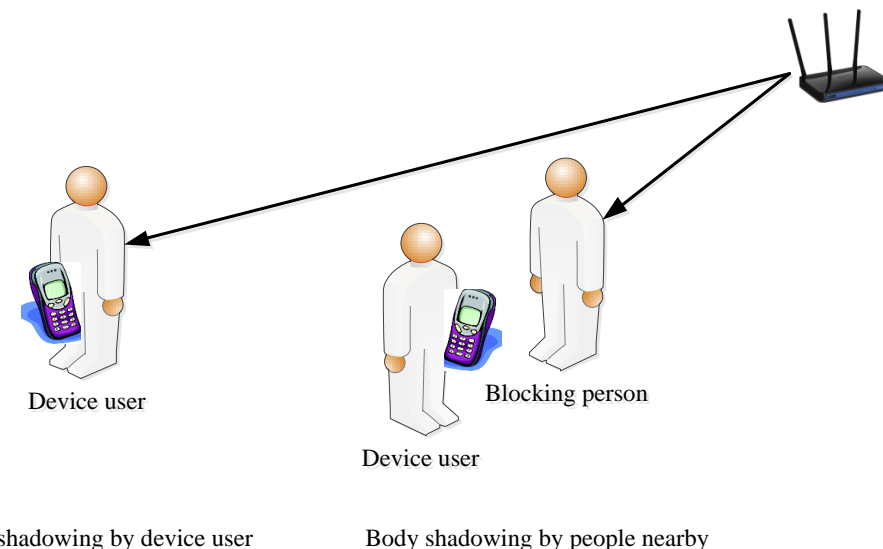


Figure 1.2: Body shadowing effect caused by device user and/or people nearby

1.1.4 Integration of RSS and other Sensors for Indoor Positioning

As introduced in the previous section, an RSS-based positioning system suffers from significant uncertainty in RSS measurements due to harsh signal propagations including body shadowing effects, which limits positioning performance. To enhance an RSS-based indoor positioning system, two strategies can be considered: first, better modeling and estimation of the uncertainty components in measurements; second, incorporation of prior information to constrain the measurement likelihood model. Corresponding to the first strategy, this thesis will look into modeling the RSS loss (or error) due to body shadowing effects for positioning improvement purposes. The second strategy seeks to incorporate prior information from additional sensors or knowledge sources into an RSS positioning system to ultimately enhance positioning performance. As introduced above, all the existing indoor positioning techniques have respective advantages and shortcomings. A key to provide reliable, continuous and accurate positioning solutions is to integrate various techniques considering their complementary characteristics (Li, 2015).

So far, numerous techniques have been proposed to integrate RSS with various forms of sensor data for positioning, including integration of Wi-Fi or Radio-frequency identification (RFID) with IMU for Pedestrian Dead Reckoning (PDR) (Evennou and Marx, 2006, Ruiz et al 2012), fingerprinting with Wi-Fi and magnetometer (Li et al 2015), Wi-Fi fingerprinting with user heading estimate by magnetometer to select database (King et al 2006), etc. The additional information from other sensors provides certain constraints that help to enhance an RSS-based positioning system. For example, the adverse effects of human body shadowing on RSS positioning has shown to be associated with a device user's heading and gesture (handheld,

phoning, dangling, etc.) (Li et al 2015). The use of IMU and magnetometers can provide user's gesture recognition and heading estimation (Benbasat and Paradiso, 2001, King et al 2006, Pei et al 2012, Pei et al 2013). Such information could be utilized to model the body shadowing effects and improve the ultimate positioning performance.

Techniques using static cameras for object detection and tracking have been researched for decades by the Computer Vision (CV) community (Yilmaz et al 2006). With increasing use of security camera in large public or commercial space (e.g. airports, shopping centers, museums and industrial plant, etc.), using static cameras for positioning is becoming of interest (Mautz and Tilch, 2011). A security camera system normally involves servers running CV algorithms to process video data transmitted from a network of cameras that are distributed in an area of interest. The development of such a system for tracking people in large-scale public spaces must take into consideration the efficiency of CV algorithms and requirements on networking and computing. With advances in CV algorithm, computation power of computers and networking infrastructure, the development of a security camera network system for object detection and tracking is becoming feasible (Krumm et al 2000, Breitenstein et al 2011, Luo et al 2014, Nielsen et al 2016). Also, object tracking has proven to be of great potential for many high-level tasks including face and behavioral recognition (Luo et al 2014). A full review of the details of object tracking can be found in Yilmaz et al (2006) and Luo et al (2014). Although positioning with security cameras can generally provide high accuracy, it can suffer from many issues, including ambiguous identity of the people tracked. Object tracking needs to maintain the uniqueness of the track of a tracked person which is known as a data association issue (Zhang et al 2008, Wu et al 2012). For positioning purpose, a track needs to be further associated to the corresponding person, however, a visual tracking system is not able to identify people without

additional information. Another issue for object tracking is due to inter-human or scene occlusion. Occlusion results in failure in object detection and interruption of the data association already established (Tang et al 2014). A few contributions have been reported to combine security camera and Wi-Fi RSS for positioning (Miyaki et al 2007, Van den Berghe et al 2011, Perš et al 2011). One main focus of the thesis is to utilize the information from security cameras to enhance the RSS-based positioning. Other relevant research and limitations will be discussed in detailed in Section 1.2.

1.1.5 Incorporating Building Map Information for Indoor Positioning

In addition to using prior information from sensor data to provide constraints and thus enhance ultimate positioning performance, for indoor positioning in places such as shopping malls, office and campus building, etc., existing building maps have been widely used to provide prior information and complement the positioning. This process of fusing a positioning system with map information is usually called map-matching (Davidson et al 2010).

In general, map-matching is used as an aid for a positioning system, e.g., RSS-based, IMU-based, GNSS-based. The idea of map-matching is to utilize map information to constrain or correct user's motion to remove errors in the positioning system. Two key components of map-matching techniques are building map information representation and matching methods. For example, map represented by a Computer Aided Drawing (CAD) floor plan provides information of the walls inside a building (Khan and Syrjäinne, 2013). The wall information can be used to assess if a positioning solution is reasonable, e.g., position estimates cannot appear in non-walkable areas, or mobile trajectories cannot pass through walls without opening and so forth. The assessment then can be used by the following matching methods. Another key component of

map-matching techniques, namely matching methods, is the way that map information is used to complement positioning. One type of matching algorithm can directly correct the position estimates from a positioning system using some regulations derived from map constraints and use the corrected results as ultimate positioning solutions, without feedback to the positioning system. Work based on this type of matching includes White et al (2000), Walder and Bernoulli, (2010), SPASSO (2007). Normally, these types of approach are straightforward and computationally efficient, but are sensitive to outliers producing unexpected results (Jiang et al 2016). Contrary to the first type, the second type of matching methods is essentially an element of the positioning system which applies map constraints inside the positioning system. For these types of methods, probabilistic approaches based on particle filters are widely used (Ferris et al 2006, Barcelo et al 2006, Evennou and Marx, 2006, Evennou et al 2005, Khan and Syrjarinne, 2013, Nurminen et al 2014). Generally, particle filter map-matching approaches apply map constraints to the particle propagation motion model or the weights of particles to influence the a posteriori distribution of position state. For example, weights of particles crossing walls are reduced or set to zero. Normally, these approaches can generate more reliable results, but are computationally expensive.

Map-matching has been used to assist various positioning system such as IMU-PDR (Klepal and Beauregard, 2008, Ascher et al 2010, Nurminen et al 2016), Wi-Fi RSS fingerprinting (Evennou et al 2005), Wi-Fi/IMU(Evennou and Marx, 2006, Khan and Syrjarinne, 2013), GPS/IMU/Wi-Fi (Attia et al 2011), to name a few. One main focus of the thesis is to integrate map-matching and security cameras into an RSS-based positioning system. More relevant research will be reviewed in Section 1.2.

1.2 Limitations of Previous Research

1.2.1 RSS Body Shadowing Effects on RSS-based Positioning

As emphasized before, considerable uncertainty in RSS measurements is the main challenge of a RSS-based positioning system. For positioning using a mobile device, RSS fluctuations due to shadowing or absorption introduced by the human body are inevitable and have gained research attention. In general, body shadowing effects reported in the literature fall into two categories: effects introduced by a device user's body and those introduced by people near the user. Normally, the user's body blocks signals with a certain orientation referenced to a local level frame for a specific user's gesture (e.g. handheld, phoning, dangling, etc.). Hence the user's body shadowing effect can be related to the user's gestures and heading given the location of an AP (Li et al 2015, King et al 2006). The dependence of the heading of a mobile user on RSS body shadowing loss has previously been reported (Bahl and Padmanabhan, 2000, King et al 2006, Li et al 2015). Some research has reported shadowing effects in the Wi-Fi 2.4 GHz signal band. It was reported by Bahl and Padmanabhan (2000) that the RSS fluctuation at a given location as the user rotates can be 5 dB without mention of the distance between user and AP. In King et al (2006), the AP was 5 m from a user and the RSS was measured every 45° as the user holding the mobile turned around. A 15 dB RSS body blocking loss when the AP was totally blocked and more than 5 dB blocking loss when the AP was partially blocked were reported. In Della Rosa et al (2012), a 15 dB RSS body blocking loss was reported when the AP is 6 m distant from the user and more than a 5 m ranging error was reported in this case, as compared to 1 m ranging error in the no-shadowing case. For shadowing caused by other people in the vicinity, Chen et al (2005) investigated the effect by creating a 'blocking-around' scenario, where a formation of six people was arranged surrounding a device user in a fixed location. It was reported that the average RSS

value over APs decreases 8 *dB*, and the average positioning accuracy deteriorates from 2.13 *m* to 3.96 *m* due to the blocking-around effect, however, the distance between the blocking people and device was not reported and shadowing was simply treated as a two-state scenario. The limitations of previous research are:

1. How the user's heading influences the RSS loss due to body shadowing was only compared at the same location for the same AP. However, for positioning purposes, the loss should be measured and analyzed at multiple locations at different APs in a suitable test area. Abundant measurements will enable a statistical analysis of the RSS loss due to body shadowing and its effects on positioning performance.
2. Only measurements of RSS loss due to body shadowing were reported and the adverse effects on positioning performance were given, without attempting to model the RSS body shadowing loss to improve positioning performance. The modeling of the RSS body shadowing loss could be used to mitigate the RSS uncertainty due to body shadowing and mitigate the adverse effects on positioning performance.
3. Only the Wi-Fi 2.4 GHz signal was studied. As mentioned previously, most Wi-Fi AP devices now transmit signals in the 2.4 GHz and 5 GHz frequency bands simultaneously, and 5 GHz RSS observations have lower variation than those of the 2.4 GHz signals (Farshad et al 2013, Yu et al 2014). Therefore, it is of interest to investigate the RSS body blocking loss for the 5 GHz signal for positioning purposes.

1.2.2 Integration of RSS with Security Camera and Building Maps for Indoor Positioning

Integration of RSS and security cameras is still a new area and only a few contributions have been reported so far (Van den Berghe et al 2011, Papaioannou et al 2014, Radaelli et al 2014). In

general, the fusion approaches fall into three categories: camera-aided radio, radio-aided camera and radio/camera integration. The work reported by Radaelli et al (2014) is an example of camera-aided radio, where security cameras are used to assist automatic collection of RSS fingerprints and achieve room-level accuracy positioning performance. In their work, surveillance cameras were assumed to have high room-level accuracy and were used to detect the room a user is in. Once a user is detected, the RSS measurements of the user will be uploaded to a server for training input to a radio map. For the radio-aided camera scheme, a security camera system is used as the main positioning system and wireless signals are used to assist to solve the CV tracking issue such as occlusion, dim lighting, ambiguous object's identity, and object disappearance from the camera Field of View (FOV). The work reported by (Van den Berghe et al 2011) is an example of this, whereby the object tracking segments (tracklets) generated by a visual tracking system are broadcast to a radio-aided tracker. With these tracklets, a multi-hypothesis probabilistic approach is used by the radio-aided tracker to cross reference the user's private radio footprint generated by Wi-Fi RSS measurements and produce the complete trajectory of a specific user. It was reported that this system yields typical position errors below 1 *m*. A radio/camera integration scheme is proposed in work by Van den Berghe et al (2011), where the measurement likelihood models of Wi-Fi RSS and camera data are combined in a particle filter frame to produce the position a posteriori distribution and then the position estimates.

A common point in these approaches is that the object detection (or tracking) results in images must be mapped to positions, either to calibrate the RSS database, provide ultimate positioning solutions, or calculate the observation likelihood models. To do this, a CV system normally needs to detect (may also track) an object on an image pixel plane and then maps the object's

position from the image pixel coordinate to local coordinate. To map the detected object to local coordinates accurately, a CV system needs to be very carefully calibrated to obtain accurate camera intrinsic and extrinsic parameters, as will be described in Appendix B. Even if a well-calibrated CV tracking system under ideal conditions can reach sub-metre accuracy, however, as compared to the coverage of wireless signal, the Field of View (FOV) of cameras is relatively limited. On the contrary, an RSS-based location system is almost ubiquitous in coverage. Therefore, it would be interesting to investigate how to set up a security camera system without complex calibration, and obtain information efficiently from CV processing to enhance an RSS-based system to provide continuous and accurate positioning solutions.

Map-matching techniques have been used in various positioning systems. An RSS positioning system often suffers from large errors in position solutions due to the considerable fluctuations in RSS measurements, and thus map-matching is quite promising to aid the RSS-based positioning system by constraining the position solutions based on map information. As introduced previously, map-matching based on a probabilistic approach calculates the probability of a target to be located at a position and can generate a more reliable result. The map constraints applied to position estimation are normally highly nonlinear transformations. One merit of a particle filter is its ability to model the nonlinear transformation of random variable (Thrun et al 2005), hence particle filters are widely used in probabilistic map-matching. Many research results have reported the use of particle filter map-matching in positioning systems involving RSS. In these contributions, the map constraints are essentially incorporated by updating the weights of particles in different positions to influence the position state a posteriori distribution. These contributions differ in the sensors and positioning methods used, and thus the structure to integrate the sensors and map information. For example, in the work done by Evennou and Marx

(2006), a structure to integrate Wi-Fi RSS fingerprinting, IMU PDR and map information using a particle filter was proposed. For the work report by Khan and Syrjarinne, (2013), Wi-Fi RSS trilateration, IMU PDR and map information are integrated. For this thesis, based on the integration of security camera and RSS, it is of interest to further incorporate building map information to enhance the overall positioning performance.

1.3 Objective and Contributions

Due to the limitations of the previous research mentioned above, the overall aim of this thesis is to model the body shadowing effect on RSS measurement and incorporate prior information from security camera and building map to enhance an RSS-based indoor positioning system.

Given the limitations discussed in the previous sections, the specific objectives of this thesis are to investigate the following aspects:

- 1) Since the body shadowing effect on RSS is a complex phenomenon of physics, modeling its mechanism from a physical basis would be very difficult if not impossible due to a large number of continuously changing parameters. Is it possible to come up with an empirical model with a small number of parameters to partially model and mitigate the RSS uncertainty due to body shadowing? Can the parameters of the model be estimated from moderate amount of training data? Most importantly, is this model able to improve the ultimate RSS-based positioning performance?
- 2) Is it feasible to quickly setup a security camera without complex calibration and extract information effectively from the CV processing to enhance an RSS-based positioning system?

- 3) Map-matching is widely used to assist positioning systems. If the above camera-aided RSS system is feasible, then is it also feasible to incorporate building map information to the system to further improve the RSS-based indoor positioning?

The major contributions of this thesis are summarized as follows

- 1) Experimental data collection and characterization of RSS sensitivity to location and uncertainty incurred by human body shadowing for both 2.4 GHz and 5 GHz Wi-Fi signals in various indoor and outdoor environments.
- 2) Proposing an empirical model based on the above characterization for 5 GHz RSS to model the RSS loss due to body shadowing, estimation of the model parameters based on limited amount of training data, and proposing a Maximum Likelihood Estimator (MLE) that makes use of this model to jointly estimate a user's location and heading. Experimental data is used to test the proposed MLE and verify the utility of the RSS body shadowing model proposed.
- 3) Proposing an estimator to estimate user's heading in corridors based on the CV processing results using a security camera. Development of a camera-aided RSS positioning system based on Kalman filtering to fuse heading estimates from security cameras to enhance the RSS-based positioning. The performance of the camera-aided RSS positioning system is tested and compared with that of an unaided RSS system with experimental data.
- 4) Development of a prototype map-camera-aided RSS positioning system based on particle filtering to further incorporate building map information to enhance RSS-based positioning. Its performance is analyzed and compared with that of the unaided RSS system and the camera-aided RSS positioning systems.

1.4 Thesis Outline

This thesis consists of six chapters. The subsequent chapters are organized as follows:

Chapter 2 reviews some fundamental techniques and methodologies used in the thesis.

Chapter 3 characterizes RSS pathloss sensitivity, as well as uncertainties incurred by human body shadowing effects through experimental data collected in various outdoor and indoor environments. The pathloss model characterization forms the basis of the pathloss-model-based positioning algorithms used throughout the thesis. The characterization of body shadowing effect on RSS supports the modelling of RSS loss due to body shadowing in Chapter 4, which is one main focus of the thesis.

Chapter 4 focuses on modeling the RSS body shadowing loss based on the characterization made in Chapter 3. An empirical model called the body shadowing loss model is proposed to characterize dependence of RSS loss on user's heading. A MLE based on this model is proposed to jointly estimate user's location and heading. Experimental data is collected to evaluate the utility of the proposed model and algorithm.

Chapter 5 focuses on using an uncalibrated security camera and building map to enhance the RSS-based positioning system. A heading estimator based on CV processing results is proposed, and a camera-aided RSS system based on Kalman filtering is proposed to incorporate the heading estimates into the RSS-based positioning system. A map-camera-aided RSS system based on particle filtering is proposed to further incorporate building map constraints in order to enhance RSS-based positioning. Experimental results are shown to assess the benefits of the proposed algorithms.

Chapter 6 presents conclusions and recommendations.

The flow chart depicting the thesis chapters is shown in Figure 1.3.

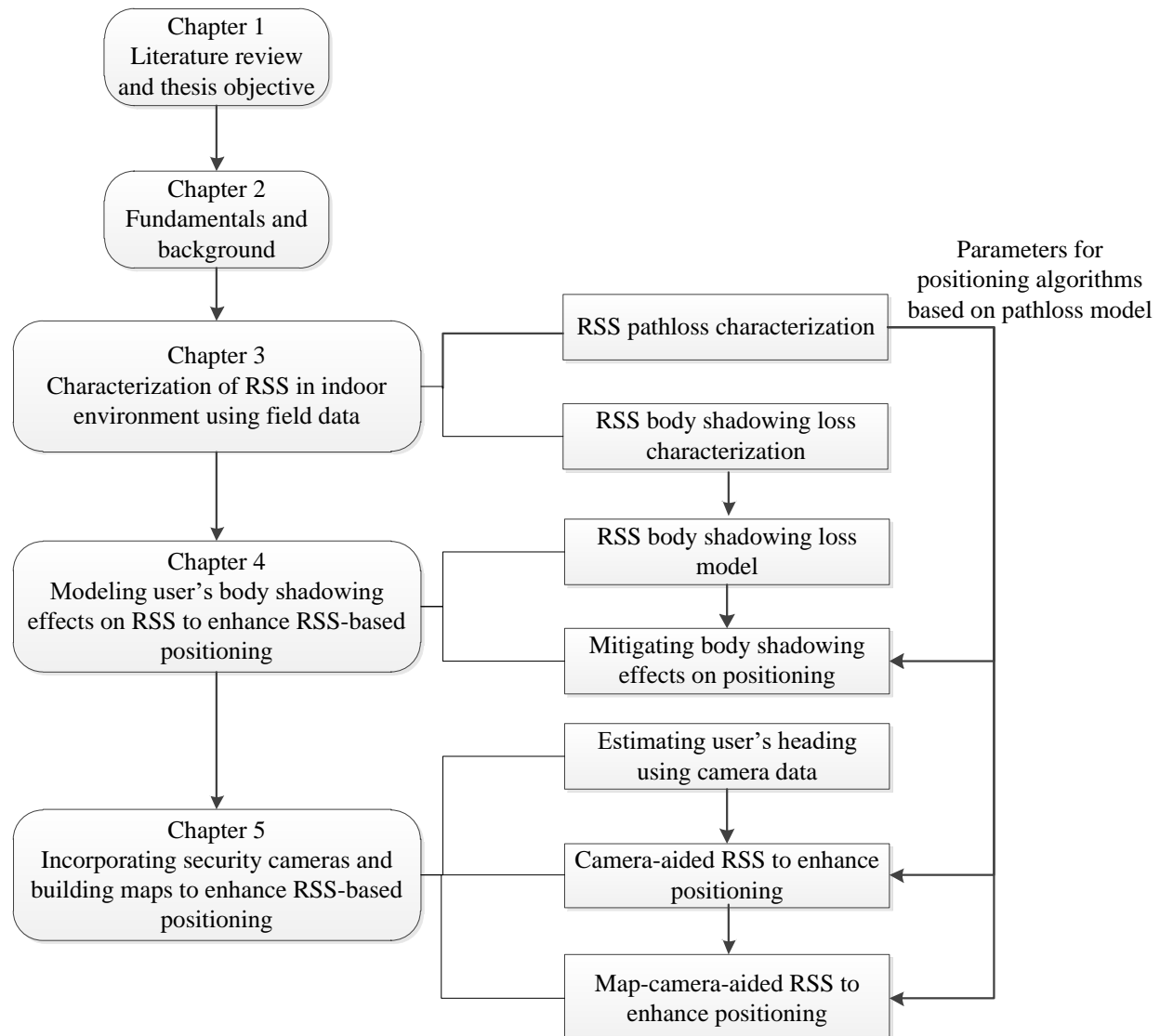


Figure 1.3: Flow chart of thesis structure

Chapter Two: **Background**

This chapter covers the basic knowledge and techniques related to RSS-based positioning, Computer Vision (CV) and estimation algorithms that are prerequisites for this thesis. Firstly, the background, fundamentals and common techniques of RSS-based positioning systems are introduced. As discussed in Chapter 1, one main objective of the thesis is to enhance RSS-based indoor positioning by incorporating prior information from security cameras and building maps. Bayesian filtering theory is reviewed with emphasis on how the prior information enhances the state estimation. Two implementations of Bayesian filter, namely the Kalman filter and particle filter, are introduced as they form the basis of the discussion in Chapter 5, where a camera and building map are incorporated for enhancing an RSS-based positioning system. CV processing for object detection is also introduced, which is the prerequisite for the method proposed in this thesis that uses security cameras to enhance RSS-based positioning.

2.1 RSS-based Indoor Positioning

This section reviews the background, fundamentals and common techniques of an RSS-based positioning system. Firstly, the background of IEEE 802.11 Wi-Fi network related to RSS reading is introduced as the RSS experimental data in this thesis are based on Wi-Fi transceivers. The Fisher information of RSS for positioning are reviewed, with emphasis on how the uncertainties in RSS reduce this information, and RSS-based positioning algorithms are introduced as they form the basis of the proposed RSS-enhancing techniques in the thesis.

2.1.1 IEEE 802.11 Wi-Fi Channel Allocations and RSS Collection Mechanism

‘Wi-Fi’ is a superset of IEEE 802.11 standards (Mautz, 2012). Table 1 summarizes some main parameters of IEEE 802.11 Wi-Fi physical layer of different standards. These standards are widely used today except for the IEEE 802.11-1997. Most Wi-Fi AP devices today transmit signals in the 2.4 GHz and 5 GHz frequency bands simultaneously, and the analysis of this thesis will be based on both bands. The “2.4 GHz band” refers to the 2.4-2.5 GHz spectrum located in the Industrial, Scientific and Medical (ISM) band, while the “5 GHz band” refers to the 4.915-5.825 GHz spectrum. The 2.4 GHz band is divided into 14 channels with spacing of 5 MHz, starting at channel 1 centered on 2.412 GHz. On the 5 GHz band, the channel center frequencies are defined at every integral multiple of 5 MHz above 5 GHz. The exact relationship between center frequency and channel number for 5 GHz band is less intuitive, and more details can be found in IEEE 802.11™ - 2012 (2012).

Table 1. IEEE 802.11 physical layer standards (Tektronix, 2013)

IEEE 802.11 PHY Standards						
Release Date	Standard	Frequency Band (GHz)	Bandwidth (MHz)	Modulation	Advanced Antenna Technologies	Maximum Data Rate
1997	802.11	2.4 GHz	20 MHz	DSSS, FHSS	N/A	2 Mbits/s
1999	802.11b	2.4 GHz	20 MHz	DSSS	N/A	11 Mbits/s
1999	802.11a	5 GHz	20 MHz	OFDM	N/A	54 Mbits/s
2003	802.11g	2.4 GHz	20 MHz	DSSS, OFDM	N/A	542 Mbits/s
2009	802.11n	2.4 GHz, 5 GHz	20 MHz, 40 MHz	OFDM	MIMO, up to 4 spatial streams	600 Mbits/s
2013	802.11ac	5 GHz	40 MHz, 80 MHz, 160 MHz	OFDM	MIMO, MU-MIMO, up to 8 spatial streams	6.93 Gbits/s

Generally, a Wi-Fi Access Point (AP) sends out beacon frames periodically in order to announce its presence. The beacon interval is often set to 100 ms by default. A Wi-Fi station (e.g., a mobile device) scans the beacons periodically to extract information from an AP. As will be discussed for RSS-based positioning algorithms, the relevant information includes the unique Basic Service

Set Identifier (BSSID) of an AP, RSS measurement of an AP in dBm , timestamp of measurement, signal band of RSS measurements (2.4 GHz or 5 GHz), and the data rate. The data rate varies between different Wi-Fi chipsets. For example, the chipset in the device used for this thesis (Google Nexus tablet) has a measurement update interval of about 0.7 s.

Figure 2.1 depicts a general scenario for measuring RSS. Generally, the signals transmitted by an AP undergo effects such as pathloss, shadowing, small scale fading, interference, etc. in the wireless propagation channel and are received by a mobile receiver. The received signals are then processed to produce RSS readings using certain measuring algorithms. The RSS measuring algorithms are proprietary to the Wi-Fi chipset and/or mobile device manufacturers (Lui et al 2011). For Wi-Fi 2.4 GHz signals which operate at the highly-crowded industrial, scientific and medical (ISM) band, the considerable inference sources may cause the measuring algorithms fail to measure the RSS correctly and hence produce outliers in RSS measurements. To summarize, an RSS measurement based on a Wi-Fi network RSS reading is influenced by the effects in wireless channels and proprietary measuring algorithms that varies between chipsets or mobile devices. As discussed in Chapter 1, the considerable uncertainty in the RSS reading due to channel adverse effects is a major challenge for RSS-based positioning. How this uncertainty in RSS affect positioning will be discussed next using Fisher information.

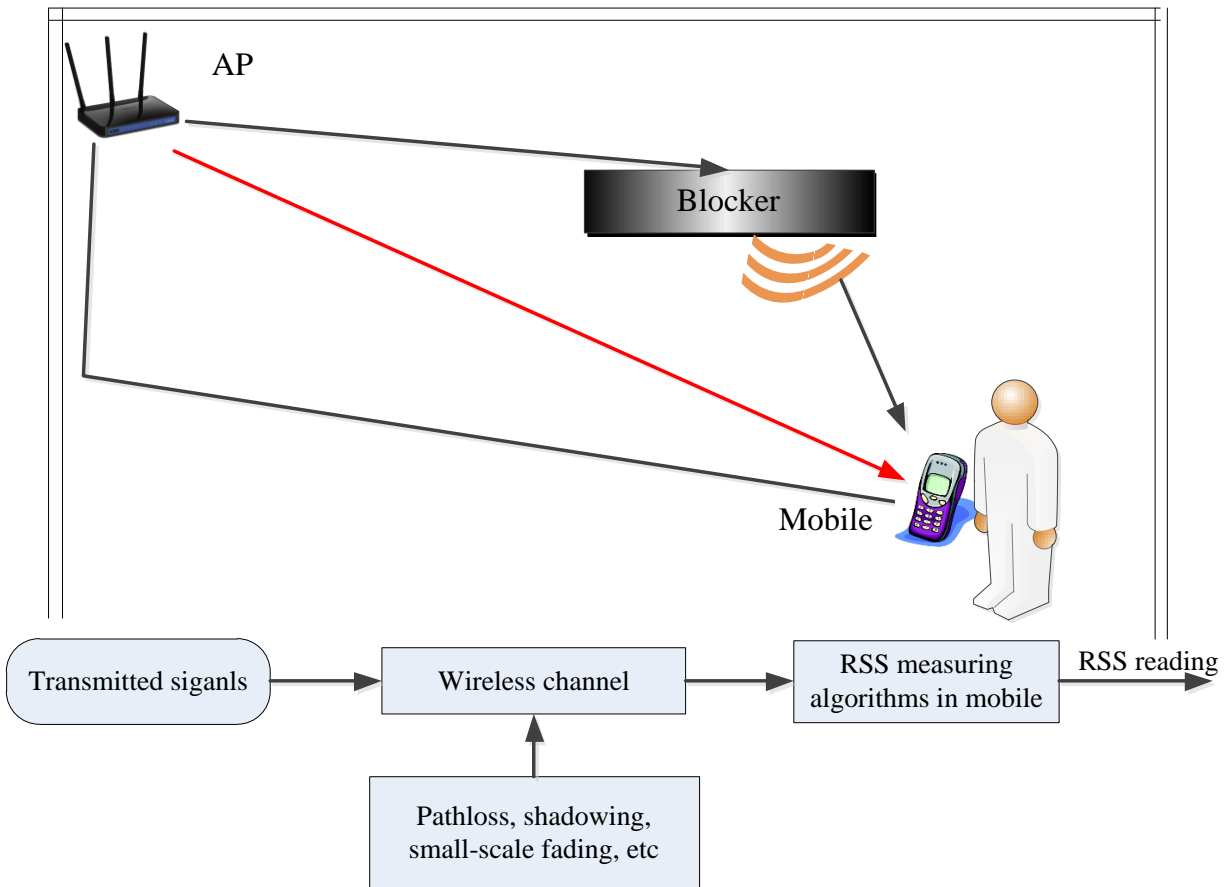


Figure 2.1: RSS acquiring in IEEE 802.11 Wi-Fi systems

2.1.2 Fisher Information and Cramer-Rao Lower Bound of RSS for Positioning

Because one main objective of this thesis is to enhance an RSS-based indoor positioning system by better modeling RSS to remove uncertainties, it is useful to understand how the uncertainty in RSS affects the ultimate positioning performance. Also, prior to the discussions of positioning algorithms, it is necessary to quantify the information contained in the RSS measurement in the context of positioning and understand the best possible positioning performance that can be achieved. A commonly used tool for quantitative assessment of the information contained in measurements is the Fisher Information (FI), and FI can be transformed directly into the Cramer-

Rao Lower Bound (CRLB) which gives the minimum variance of estimate errors for a Minimum Variance Unbiased (MVU) estimator (Kay, 1993, Van Trees, 2004).

2.1.2.1 One RSS measurement case

The derivation of the FI of RSS measurements is best introduced by first considering signal propagation from a single transmitter. Both theoretical analysis and measurement-based results indicate that received signal power decreases exponentially with distance, which can be expressed as

$$P_r(d) = P_r(d_0) \left(\frac{d}{d_0} \right)^{-n} \quad (2.1)$$

where P_r is the power of the transmitted signal in linear unit (e.g., milliwatt) measured by a receiver antenna at a distance of d m from the transmitter antenna. d_0 is a reference distance for the antenna far field and n is the pathloss exponent (Goldsmith, 2005). (2.1) can be simplified by letting the reference distance to be 1 m, which yields

$$P_r = P_0 d^{-n} \quad (2.2)$$

where P_0 is the received power at 1 m. Generally, the RSS is expressed in dBm. By defining r as the RSS in dBm, one has

$$\begin{aligned} r &= 10 \log_{10}(P_r) \\ &= 10 \log_{10}(P_0 d^{-n}) \\ &= 10 \log_{10}(P_0) - 10 n \log_{10}(d) \\ &= r_0 - 10 n \log_{10}(d) \end{aligned} \quad (2.3)$$

where r_0 is the RSS in dBm measured at 1 m distance from the transmitter antenna. (2.3) is the expression of the log-distance pathloss model that is commonly used. Note that (2.3) models the

RSS only considering the pathloss effect. In practice, RSS is subject to many other factors which include signal shadowing, small scale multipath fading and radio interference that impairs the ability of the receiver to generate an accurate RSS reading, variable output power of wireless routers which are sometimes configured to adapt to fluctuating data traffic, (Nielsen and Nielsen, 2016), as well as body shadowing that will be investigated in the thesis. Correspondingly, an RSS measurement should be model as a random variable and hence (2.3) is written as

$$r = r_0 - 10n \log_{10}(d) + w \quad (2.4)$$

where w is a random variable that represents the uncertainty or “noise” component in the RSS measurements. (2.4) is the data model of RSS measurements with the interested parameter d for positioning purpose, from which the RSS measurement FI analysis can be conducted. Denote the Probability Density Function (PDF) of the RSS conditioned on the parameter d as $p(r|d)$, the FI is computed as (Kay, 1993)

$$J(d) = E_r \left[\left(\frac{\partial \ln p(r|d)}{\partial d} \right)^2 \right] \quad (2.5)$$

where $E_r[\bullet]$ represents the expectation value taken with respect to the random variable r . Note that (2.5) only provides the general FI expression regardless of the PDF of the noise. To proceed, an assumption regarding the RSS measurement PDF $p(r|d)$ is needed. The uncertainty in RSS measurement typically is assumed to be a Gaussian random variable with PDF

$$p(r|d) = \frac{1}{\sqrt{2\pi\sigma_r^2}} \exp \left[-\frac{(r - r_0(d))^2}{2\sigma_r^2} \right] \quad (2.6)$$

where $r_0(d)$ and σ_r are the mean and standard deviation of the RSS measurement r , respectively (Nielsen and Nielsen, 2016). Inserting the PDF of RSS in (2.6) to (2.5) gives

$$\begin{aligned} J(d) &= \frac{1}{\sigma_r^2} \left(\frac{dr_0(d)}{dd} \right)^2 \\ &= \frac{1}{\sigma_r^2} \left(\frac{10n}{d \ln 10} \right)^2 \end{aligned} \quad (2.7)$$

which is the FI of the RSS measurement from one single transmitter for estimating d , the range from the transmitter to receiver. Next extend the above FI analysis into a two-dimensional (2D) space for positioning purposes, with a receiver location in a 2D space represented by (x, y) , and with the transmitter located at origin, as shown in Figure 2.2. The parameter d , the distance from the transmitter and receiver, is

$$d = \sqrt{x^2 + y^2} \quad (2.8)$$

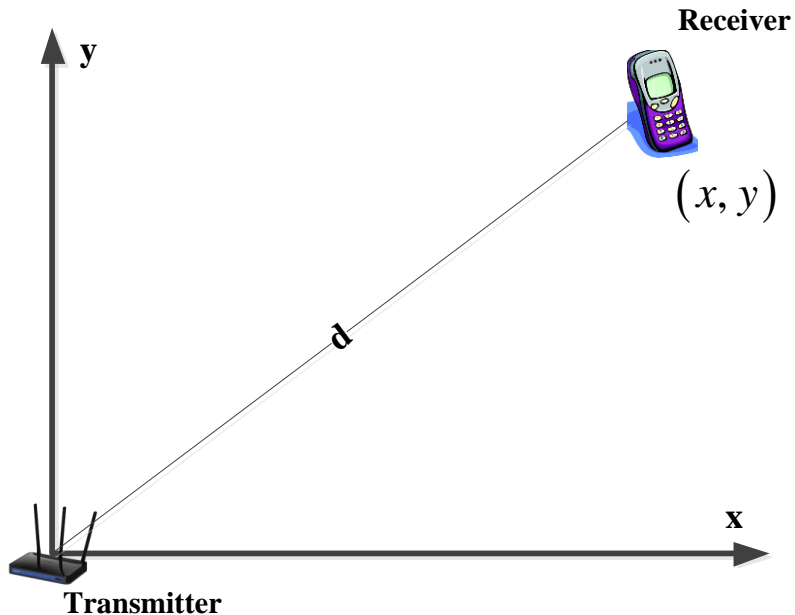


Figure 2.2 Two dimensional wireless link

Although the receiver location (x, y) cannot be jointly estimated using the RSS from a single transmitter, the Fisher Information Matrix (FIM) can be computed by using the FI for d in (2.7) as well as the relationship between d and (x, y) given in (2.8) (Nielsen and Nielsen, 2016). Specifically, denote the FIM of a single RSS measurement by \mathbf{J}_r which can be expressed as

$$\mathbf{J}_r = \begin{bmatrix} J_{xx} & J_{xy} \\ J_{yx} & J_{yy} \end{bmatrix} = \begin{bmatrix} g_x^2 & g_x g_y \\ g_y g_x & g_y^2 \end{bmatrix} \quad (2.9)$$

where

$$\begin{aligned} g_x &= \frac{dr(d)}{dx} = \frac{dr(d)}{dd} \frac{dd}{dx} \\ g_y &= \frac{dr(d)}{dy} = \frac{dr(d)}{dd} \frac{dd}{dy} \end{aligned} \quad (2.10)$$

By using (2.7), (2.8) and (2.10), one obtains

$$\begin{aligned} J_{xx} &= \frac{1}{\sigma_r^2} \left(\frac{10n}{\ln 10} \right)^2 \frac{x^2}{d^4} \\ J_{yy} &= \frac{1}{\sigma_r^2} \left(\frac{10n}{\ln 10} \right)^2 \frac{y^2}{d^4} \end{aligned} \quad (2.11)$$

It can be seen from (2.11) that the FI decays quickly as T-R distance. Also note that the FIM is singular and cannot be inverted, since the determinant of the FIM, $|\mathbf{J}_r|$, is equal to 0 all the time.

This means that receiver location (x, y) cannot be jointly estimated by using the single RSS measurement as expected (Nielsen and Nielsen, 2016).

2.1.2.2 Multiple RSS measurements case

To estimate (x, y) , multiple RSS measurements from spatially separated APs must be combined so that the aggregate FIM of the combined RSS measurements becomes non-singular. Suppose a receiver measures RSS from M APs simultaneously, and denote the M RSS measurement as a vector as

$$\mathbf{r} \triangleq [r_1 \quad \cdots \quad r_m \quad \cdots \quad r_M]^T \quad (2.12)$$

Note that this RSS vector is conditioned on the location of the receiver denoted by

$$\boldsymbol{\theta} \triangleq (x, y) \quad (2.13)$$

In addition, it is generally assumed that the uncertainties associated with each RSS measurements are mutually independent (Nielsen and Nielsen, 2016). Hence, the PDF of the RSS vector conditioned on the receiver's location can be written as

$$p(\mathbf{r} | \boldsymbol{\theta}) = \prod_{m=1}^M p(r_m | \boldsymbol{\theta}) \quad (2.14)$$

Denote the FIM of the m th RSS measurement as \mathbf{J}_m and the \mathbf{J}_T as the FIM of the RSS vector \mathbf{r} .

\mathbf{J}_T can be written as (Kay, 1993)

$$[\mathbf{J}_T(\boldsymbol{\theta})]_{i,j} = -E_{\mathbf{r}} \left[\frac{\partial^2}{\partial \theta_i \partial \theta_j} \ln \left(\prod_{m=1}^M p(r_m | \boldsymbol{\theta}) \right) \right], \quad i, j = 1, 2 \quad (2.15)$$

which can be further expanded as

$$\begin{aligned}
[\mathbf{J}_T(\boldsymbol{\theta})]_{i,j} &= -E_r \left[\sum_{m=1}^M \frac{\partial^2}{\partial \theta_i \partial \theta_j} \ln p(r_m | \boldsymbol{\theta}) \right] \\
&= -\sum_{m=1}^M E_r \left[\frac{\partial^2}{\partial \theta_i \partial \theta_j} \ln p(r_m | \boldsymbol{\theta}) \right] \\
&= \sum_{m=1}^M [\mathbf{J}_m(\boldsymbol{\theta})]_{i,j}
\end{aligned} \tag{2.16}$$

which indicates that the FIM of the aggregate RSS measurements equals the sum of the FIMs of individual RSS measurements. Therefore, by combining (2.16) and the FIM of a single RSS measurement discussed previously, one obtains the FIM of a set of RSS measurements for 2D position estimation. To use the $\mathbf{J}_T(\boldsymbol{\theta})$ to gain more understanding regarding the factors that affect the ultimate positioning performance, denote $\mathbf{J}_T(\boldsymbol{\theta})$ as

$$\mathbf{J}_T(\boldsymbol{\theta}) = \begin{bmatrix} J_{xx} & J_{xy} \\ J_{yx} & J_{yy} \end{bmatrix} \tag{2.17}$$

and its inverse, $\mathbf{J}_T^{-1}(\boldsymbol{\theta})$, as $\mathbf{Q}(\boldsymbol{\theta})$ which is the covariance matrix of the position estimate $\hat{\boldsymbol{\theta}}$ or (\hat{x}, \hat{y}) (Kay, 1993), that is

$$\mathbf{Q}(\boldsymbol{\theta}) = \mathbf{J}_T^{-1}(\boldsymbol{\theta}) = D_p^2 \begin{bmatrix} 1/J_{xx} & 1/J_{xy} \\ 1/J_{yx} & 1/J_{yy} \end{bmatrix} \tag{2.18}$$

where D_p is the so-called Dilution of Precision (DOP):

$$D_p = \left(1 - \frac{J_{xy}^2}{J_{xx} J_{yy}} \right)^{-1/2} \tag{2.19}$$

The CRLB of the variance of the estimate are given by the diagonal components of the $\mathbf{Q}(\boldsymbol{\theta})$ (Kay, 1993). Specifically, the CRLB values of (\hat{x}, \hat{y}) are

$$\begin{aligned}\sigma_{x_M}^2 &= \frac{D_p}{J_{xx}} \\ \sigma_{y_M}^2 &= \frac{D_p}{J_{yy}}\end{aligned}\tag{2.20}$$

Thus the CRLB of the position estimate error is

$$\sigma_{x_M}^2 + \sigma_{y_M}^2 = D_p \left(\frac{1}{J_{xx}} + \frac{1}{J_{yy}} \right).\tag{2.21}$$

It can be seen that positioning performance based on a set of RSS measurements from APs are affected mainly by the DOP and the FI provided by individual RSS measurements. The DOP is associated with the geometry of APs' distribution and can be optimized to enhance positioning by considering the AP deployment. However, the significant uncertainty in the RSS reduces the FI of individual measurement and degrades performance. Some mechanisms that give rise to uncertainty can be partially modeled. This reduces the uncertainty of the RSS measurement and thus the information available for the location estimate is enhanced. Correspondingly, one main objective of this thesis is to mitigate body shadowing effects by modeling the RSS loss brought by this shadowing. In Chapter 3, experimental data will be used to characterize the uncertainty in RSS due to body shadowing. Based on this, an empirical body shadowing model is proposed in Chapter 4 which is shown to have practical utility to mitigate the effect of body shadowing on positioning performance.

2.1.3 RSS-based Positioning Techniques

In general, positioning techniques making use of RSS measurements can be classified into three categories: cell of origin method, pathloss-model-based methods and fingerprinting method. Cell of origin is a straightforward method where the location of the AP with highest RSS is used

as the location the mobile device, and thus it only provide very coarse position(Mautz, 2012). The following sections introduce the two latter methods in detail, especially the pathloss-model-based methods which will be used to build positioning systems throughout the thesis.

2.1.3.1 RSS Fingerprinting

Generally speaking, RSS fingerprinting techniques localize a mobile target by pattern-matching RSS online measurements with an RSS offline database using deterministic or probabilistic models (Li et al 2015, Honkavirta et al 2009). In this method, the signal propagation is described empirically by creating a database (or radio-map) that covers the area of interest in an offline training stage (Honkavirta et al 2009), which is different from the pathloss-model-based methods where signal propagation is expressed using a pathloss model. Specifically, in the training stage, RSS measurements of APs are collected in predefined locations in the area of interest, also known as Reference Points (RPs). These RSS measurements are then compiled into deterministic or probabilistic models and stored along with the corresponding BSSID and ground-truth location in a database, also known as a radio map. This original radio map could be further smoothed or interpolated to increase the spatial resolution and hence improve the ultimate positioning performance (Letchner et al 2005, Ferris et al 2006). For example, Figure 2.3 is an RSS mean value radio map created by manually collecting RSS measurements in a set of discrete RPs and using Gaussian processes to perform spatial interpolation (Ferris et al 2006, Li et al 2015, Richter et al 2015). During the online positioning stage, RSS measurements from user devices are used to find the best matches in the radio map to determine the user's location by deterministic or probabilistic metrics (Honkavirta et al 2009). RSS-based fingerprinting positioning was pioneered by Bahl and Padmanabhan (2000). and has gained significant

commercial interest (Mautz, 2012). A major drawback is that it requires a laborious and costly offline pre-survey for the creation and maintenance of radio maps. Pathloss-model-based methods use a pathloss model to predict the signal propagation as a function of transmitter-receiver-distance, which are introduced next.

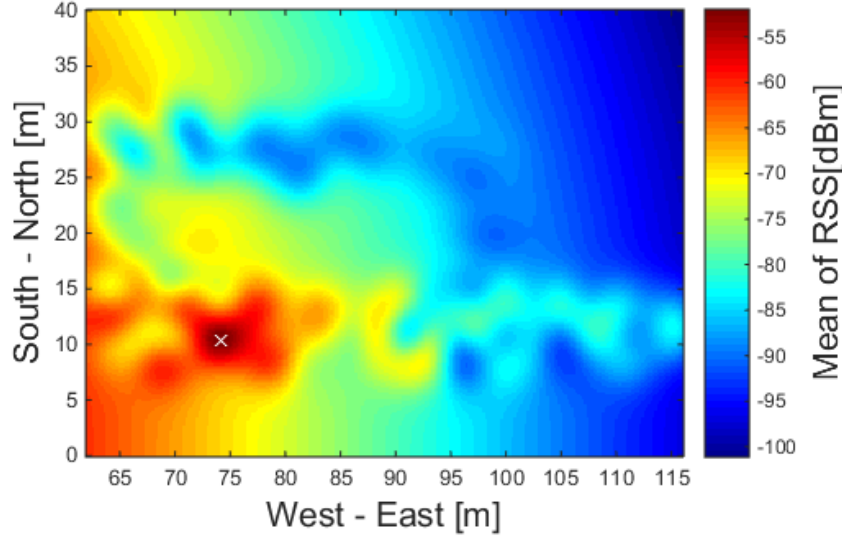


Figure 2.3: RSS mean value heat maps of an AP (Li et al 2015)

2.1.3.2 RSS Positioning based on Pathloss Model

The range between a transmitter and a receiver can be related to RSS measurements through the classic radio propagation log-distance pathloss model (Li, 2006, Rappaport, 1996). This pathloss model was briefly introduced in Section 2.1.2 and is rewritten below for more discussion prior to the description of the algorithm based on it.

$$r = r_0 - 10n \log_{10}(d) + w \quad (2.22)$$

In (2.22), r is an RSS measurement in dBm associated with a transmitter (e.g., Wi-Fi AP) at a distance d from the mobile, r_0 is the RSS in dBm measured at 1 m distance from the AP and n is the pathloss exponent (also known as distance-power gradient). w is a random variable

representing the uncertainty in the RSS incurred by the factors not modeled such as multipath, shadowing, antenna orientation, etc., as discussed previously. Depending on the assumptions made on the PDF of w , different positioning algorithms can be developed.

There are two steps when utilizing the pathloss model for positioning. The first step is to train the parameters r_0 and n in the pathloss model for each AP. This is done in a calibration stage using the RSS measurements collected in a set of known locations which are also known as Reference Points (RPs) (Khan and Syrjäinne, 2013). Less labor is needed for the pathloss model calibration herein as compared to fingerprinting due to the use of models to characterize wireless channels. With the pathloss model parameters ready, the second step is to estimate the mobile's location using RSS measurements based on the positioning algorithm selected. Suppose a mobile target is located at an unknown location \mathbf{p} , and at a certain epoch the mobile device receives the RSS vector

$$\mathbf{r} = [r_1 \quad \cdots \quad r_m \quad \cdots \quad r_M]^T \quad (2.23)$$

from M APs located at known locations \mathbf{p}_m , $m = 1, \dots, M$. Note that for the fingerprinting method introduced above, such a condition is not necessary; however, more RSS measurements are needed therefore to describe signal propagation. The problem in RSS-based positioning is to estimate \mathbf{p} using the received RSS measurements \mathbf{r} from multiple APs. Based on the assumptions made on the PDF of noise in the RSS measurement as expressed in (2.22), two commonly used methods, namely trilateration and Maximum Likelihood Estimators (MLE) will be introduced and used or extended in this thesis for design RSS-based indoor positioning algorithms.

- Maximum Likelihood Estimator

In generally, the MLE technique assumes that the PDF of the measurements is known and the MLE is given by the value of the parameter vector $\boldsymbol{\theta}$ that maximizes the log-likelihood function (Kay, 1993, Van Trees, 2004), that is

$$\hat{\boldsymbol{\theta}}_{ML} \triangleq \arg \max_{\boldsymbol{\theta}} \{ \ln p(\mathbf{z} | \boldsymbol{\theta}) \} \quad (2.24)$$

For the RSS-based positioning case, the parameter of interest $\boldsymbol{\theta}$ is the mobile location \mathbf{p} and the measurement \mathbf{z} is the received RSS vector defined in (2.23). Correspondingly, the MLE of RSS-based positioning is given by

$$\hat{\mathbf{p}}_{ML} \triangleq \arg \max_{\mathbf{p}} \{ \ln p(\mathbf{r} | \mathbf{p}) \} \quad (2.25)$$

where $p(\mathbf{r} | \mathbf{p})$ is the joint PDF of the RSS components in \mathbf{r} . As introduced in the previous FI discussion, it is generally assumed that the PDF values associated with the individual RSS measurements are mutually independent, thus the joint PDF of the RSS vector can be written as

$$p(\mathbf{r} | \mathbf{p}) = \prod_{m=1}^M p(r_m | \mathbf{p}) \quad (2.26)$$

Thus the log-likelihood of the RSS vector is

$$\begin{aligned} L_r(\mathbf{p}) &\triangleq \ln p(\mathbf{r} | \mathbf{p}) \\ &= \ln \prod_{m=1}^M p(r_m | \mathbf{p}) \\ &= \sum_{m=1}^M \ln p(r_m | \mathbf{p}) \end{aligned} \quad (2.27)$$

which states that the log-likelihood function of the RSS vector is the summation of the likelihood functions of the RSS components. Inserting (2.27) to (2.25) yields the following position MLE:

$$\begin{aligned}\mathbf{p}_{ML} &= \arg \max_{\mathbf{p}} \left\{ L_r(\mathbf{p}) \right\} \\ &= \arg \max_{\mathbf{p}} \left\{ \sum_{m=1}^M \ln p(r_m | \mathbf{p}) \right\}\end{aligned}\tag{2.28}$$

For large measurement records, the MLE is optimum in a way that it is asymptotically unbiased, achieves the CRLB and has a Gaussian PDF (Kay, 1993). Note that the position MLE in (2.28) only models the pathloss effect on RSS, however, as discussed previously, other unmodeled factors that incurred considerable uncertainties will highly affect performance. In Chapter 4, the position MLE in (2.28) is extended by further modeling the RSS loss due to body shadowing effect. A MLE will be proposed therein to jointly estimate the user's location and heading.

- Trilateration

The MLE discussed in the last section is optimal based on the assumption that the PDF of measurement is known and a large amount of data is available. However, usually the exact PDF of measurements is unknown. On the other hand, trilateration based on Least-Squares (LS) algorithm makes no assumption on the PDF of the measurements, and is the most commonly range-based algorithm based on geometry principles (Zanca et al 2008, Langendoen and Reijers, 2003). The range estimator using the pathloss model in (2.22) takes the form of

$$\hat{d} = 10^{\frac{r_0 - r}{10n}}\tag{2.29}$$

The ranging performance is affected by the uncertainties shown in (2.22). While the noise increases the variance of ranging, the unmodeled systematic error offsets the range estimates and hence the ultimate position solutions.

Given the range estimates d_m , $m=1,2,\dots,M$ from the mobile device to the M APs using (2.29) and the known locations of M APs

$$\mathbf{p}_m = [x_m, y_m]^T, \quad m=1,2,\dots,M \quad (2.30)$$

the follow system equations can be obtained

$$\begin{aligned} d_1 &= (x - x_1)^2 + (y - y_1)^2 \\ &\vdots \\ d_m &= (x - x_m)^2 + (y - y_m)^2 \\ &\vdots \\ d_M &= (x - x_M)^2 + (y - y_M)^2 \end{aligned} \quad (2.31)$$

It can be seen that (2.31) is nonlinear with respect to the mobile's position $\mathbf{p} = [x \ y]$, which can be written as

$$\mathbf{d} = \mathbf{h}(\mathbf{p}) + \mathbf{w} \quad (2.32)$$

which is the trilateration observation model. In the observation model, \mathbf{p} , the mobile's position, is the state that needs to be estimated, $\mathbf{d} = [d_1 \ \dots \ d_m \ \dots \ d_M]$ is the range observation vector, \mathbf{w} is a $M \times 1$ random variable vector representing the noise associated with the range observation vector \mathbf{d} and $\mathbf{h}(\bullet)$ represents a set of non-linear equations. Equation (2.32) can be solved to estimate \mathbf{p} by using a non-linear LS technique (e.g. Petovello, 2013).

An LS estimator estimates a state or parameter from redundant measurements using an observation model (Zhuang, 2015). With the observation model given by (2.32), the goal of the LS estimator is to produce an estimate, $\hat{\mathbf{x}}$, given range observation \mathbf{d} to minimize the loss function

$$L(\hat{\mathbf{x}}) = (\mathbf{d} - \mathbf{h}(\hat{\mathbf{x}}))^T \mathbf{Q}^{-1} (\mathbf{d} - \mathbf{h}(\hat{\mathbf{x}})) \quad (2.33)$$

where $L(\bullet)$ is the loss function, \mathbf{Q}^{-1} is the inverse of the covariance matrix of the observations.

To do this, (2.32) is expanded around the current state estimate using a Taylor series expansion as

$$\begin{aligned}
 \mathbf{d} &= \mathbf{h}(\mathbf{x}) + \mathbf{v} \\
 &= \mathbf{h}(\hat{\mathbf{x}}) + \frac{d\mathbf{h}(x)}{d\mathbf{x}} \Big|_{\mathbf{x}=\hat{\mathbf{x}}} (\mathbf{x} - \hat{\mathbf{x}}) + \dots + \mathbf{w} \\
 &\approx \mathbf{h}(\hat{\mathbf{x}}) + \frac{d\mathbf{h}(x)}{d\mathbf{x}} \Big|_{\mathbf{x}=\hat{\mathbf{x}}} (\mathbf{x} - \hat{\mathbf{x}}) + \mathbf{w} \\
 &= \mathbf{h}(\hat{\mathbf{x}}) + \mathbf{H}\delta\mathbf{x} + \mathbf{w}
 \end{aligned} \tag{2.34}$$

where

$$\delta\mathbf{x} = (\mathbf{x} - \hat{\mathbf{x}}) \tag{2.35}$$

represents the “error” in the state vector and

$$\mathbf{H} = \frac{d\mathbf{h}(x)}{d\mathbf{x}} \tag{2.36}$$

is the design matrix (Petovello, 2013). In (2.34), the observation model is linearized by retaining the first order term in the Taylor series expansion. By re-arranging (2.34), one obtains

$$\begin{aligned}
 \mathbf{d} - \mathbf{h}(\hat{\mathbf{x}}) &= \mathbf{H}\delta\mathbf{x} + \mathbf{w} \\
 \delta\mathbf{d} &= \mathbf{H}\delta\mathbf{x} + \mathbf{w}
 \end{aligned} \tag{2.37}$$

where $\delta\mathbf{d}$ is a measurement misclosure vector. The derivation of the solution, $\delta\hat{\mathbf{x}}$, of the (2.37) and its covariance matrix, $C_{\delta\hat{\mathbf{x}}}$, are

$$\begin{aligned}
 \delta\hat{\mathbf{x}} &= (\mathbf{H}^T \mathbf{Q}^{-1} \mathbf{H})^{-1} \mathbf{H}^T \mathbf{Q}^{-1} \delta\mathbf{d} \\
 C_{\delta\hat{\mathbf{x}}} &= (\mathbf{H}^T \mathbf{Q}^{-1} \mathbf{H})^{-1}
 \end{aligned} \tag{2.38}$$

Note that $C_{\delta\hat{\mathbf{x}}}$ provides a confidence level of the estimate and is very useful when the estimate needed to be further processed, e.g., filtering, integration with estimates from other systems. The current estimate of state vector is calculated as

$$\hat{\mathbf{x}}_{update} = \hat{\mathbf{x}} + \delta\hat{\mathbf{x}} . \quad (2.39)$$

Similarly, the observation model now needs to be expanded around $\hat{\mathbf{x}}_{update}$. The final solution is obtained by repeating this iterative process until $|\delta\hat{\mathbf{x}}|$ is smaller than a threshold. In Chapter 5 the trilateration based on RSS will be used to provide positioning observations to a Kalman filter or particle filter, where additional information for a security camera or/and building map are also incorporated to develop RSS-enhancing techniques.

2.2 Use of Prior Information to Enhance State Estimation in Bayesian Filters

As discussed previously, the considerable uncertainties in RSS measurements in indoor environments reduce the Fisher information in the RSS for positioning and thus degrade the performance of an RSS-based indoor positioning system. One way to improve the Fisher information is to add constraints to the measurement model. From a Bayesian filtering perspective, this is to improve state a posteriori distribution estimation by incorporating states prior distribution from prior information. The prior information can be in the form of sensor data, motion dynamic model, building map, etc. As discussed in Chapter 1, this thesis seeks to utilize security cameras data and building maps to enhance RSS-based positioning systems. This section uses Bayesian filtering concepts to explain how the prior information from various sources helps in enhancing the state estimation. Two Bayesian filter implementations, namely the Kalman filter

and particle filter are introduced and will be used in Chapter 5 to develop algorithms to incorporate camera and building map information in order to enhance the RSS-based positioning.

2.2.1 Bayesian Filter

A Bayesian filter estimates the a posteriori distribution of state recursively over time by using measurements and state transition models (Arulampalam et al 2002). Specifically, the a posteriori distribution of states (also called belief) as denoted by $bel(\mathbf{x}_t)$ is the probability distribution over the states \mathbf{x}_t at time t conditioned on all the past measurements $\mathbf{z}_{1:t-1}$, that is

$$bel(\mathbf{x}_t) \triangleq p(\mathbf{x}_t | \mathbf{z}_{1:t}) \quad (2.40)$$

Note that in (2.40) the a posteriori distribution of \mathbf{x}_t is taken after incorporating the current measurement \mathbf{z}_t . The distribution of \mathbf{x}_t before incorporating the current measurement is often referred to as prediction and defined as

$$\overline{bel}(\mathbf{x}_t) \triangleq p(\mathbf{x}_t | \mathbf{z}_{1:t-1}) \quad (2.41)$$

A Bayesian filter recursively calculates the state a posteriori distribution $bel(\mathbf{x}_t)$ at time t from $bel(\mathbf{x}_{t-1})$ at $t-1$ using current measurements \mathbf{z}_t . The two essential steps of a Bayesian filter to calculate the a posteriori distributions are (Thrun et al 2005)

$$\overline{bel}(\mathbf{x}_t) = \underbrace{\int p(\mathbf{x}_t | \mathbf{x}_{t-1})}_{\text{State transition distribution}} bel(\mathbf{x}_{t-1}) d\mathbf{x}_{t-1} \quad (2.42)$$

$$bel(\mathbf{x}_t) = \eta \underbrace{p(\mathbf{z}_t | \mathbf{x}_t)}_{\text{Measurement likelihood}} \underbrace{\overline{bel}(\mathbf{x}_t)}_{\text{State prior distribution}} \quad (2.43)$$

In (2.42), the state prediction $\overline{bel}(\mathbf{x}_t)$ is made by combining the state a posteriori distribution $bel(\mathbf{x}_{t-1})$ from last time and a state transition distribution $p(\mathbf{x}_t | \mathbf{x}_{t-1})$. This step is referred to as the prediction step. In (2.43), the state a posteriori distribution is computed by multiplying a measurement likelihood model with $\overline{bel}(\mathbf{x}_t)$, where η is a normalization constant to make $bel(\mathbf{x}_t)$ integral to 1. Finally, the state estimate $\hat{\mathbf{x}}_t$ is determined from the state a posteriori distribution $bel(\mathbf{x}_t)$ based on some criterion, e.g., maximum likelihood or Maximum a posteriori (MAP). Therefore, (2.43) is directly related to the state estimation. Examine the update step in (2.43) where the measurement likelihood function is weighed or constrained by the state prior distribution. If there is no prior information regarding the state prior distribution, the state a posteriori distribution reduces to the measurement likelihood function. In this case, an accurate measurement model for removing uncertainty in measurements is the best way to improve state estimation. For example in Chapter 4, a body shadowing loss model is proposed for modelling the RSS likelihood more accurately and maximum likelihood criteria was applied to the RSS likelihood function to estimate the position state. With state prior information, the measurement likelihood function is weighed and the resulted state a posteriori distribution contained more information regarding the states. Next examine (2.42), which describes how $\overline{bel}(\mathbf{x}_t)$ is produced.

It can be seen that $\overline{bel}(\mathbf{x}_t)$ is computed using the state a posteriori in the last time step weighed by $p(\mathbf{x}_t | \mathbf{x}_{t-1})$, the state transition distribution. A state transition model provides information regarding how a state evolves over time. Prior information from the knowledge of the target's motion, sensor data, building map and other sources can be utilized to better model the state transition distribution and hence predict $\overline{bel}(\mathbf{x}_t)$. For example, a system model describes the

time evolution of the state and is widely used in filtering techniques to constrain target's motion in positioning. As will be seen in Chapter 5, heading information from security cameras data can be used to better constrain the position state propagation to avoid drift; the use of a building map can avoid that the position state propagates into an impossible location (e.g., position in inaccessible area). To summarize, the use of prior information in Bayesian filter better models the state transition and hence the state prior distribution. The state prior distribution then weighs the measurement likelihood function, resulting in a more accurate state a posteriori distribution and hence the state estimate.

The forms of the prior information also suggest ways to implement the Bayesian filter. For example, if the measurement likelihood model and state transition model are linear and Gaussian, plus if the initial state distribution is Gaussian, the Bayesian filter can be implemented by the Kalman filter. As will be explored in Chapter 5, this is the case when incorporating the heading information using a (Pedestrian Dead reckoning) PDR model. When it comes to using a building map as constraints, which normally are high nonlinear, a particle filter is commonly used. Two ways in which the Bayesian filter can be implemented will be discussed next.

2.2.2 Kalman Filtering

A widely used technique for implementing Bayesian filtering is Kalman filtering (Thrun et al 2005, Arulampalam et al 2002). The Kalman filter assumes the state a posteriori distribution is Gaussian at each time step that can be parameterized simply by a mean and covariance (Arulampalam et al 2002), provided the so-called linear/Gaussian assumptions can hold. Since the measurements used in the thesis are in discrete-time, the Kalman filter introduced herein takes a discrete-time form.

- Linear/Gaussian Assumptions

A Kalman filter assumes the state vector \mathbf{x} is a random process that can be described with a linear discrete-time model as

$$\mathbf{x}_k = \Phi_{k-1,k} \mathbf{x}_{k-1} + \mathbf{w}_{k-1} \quad (2.44)$$

where \mathbf{x}_k is the state vector at k time step, $\Phi_{k-1,k}$ is the state transition matrix from $k-1$ to k time step and \mathbf{w}_{k-1} the process noise. The model described by (2.44) is termed the system state model or motion model. The observation model is assumed available and into the following linear form:

$$\mathbf{z}_k = \mathbf{H}_k \mathbf{x}_k + \mathbf{v}_k \quad (2.45)$$

where \mathbf{z}_k is the measurement vector at k time step, \mathbf{H}_k is the design matrix at k time step and \mathbf{v}_k is the observation noise. Similar to the least-squares case, the model in (2.45) is called the observation model. Moreover, the process and measurement noise values are assumed to be white Gaussian noise and uncorrelated with each other, as well as uncorrelated with the state vector.

- Kalman filtering steps

Corresponding to the system model and observation models assumptions, the Kalman filtering consists of two main steps: predicting the state vector using the previous state estimates and the system model, and then updating the state vector using the predict state and observation model. The steps of Kalman filtering are listed herein. The prediction step is formulated by

$$\hat{\mathbf{x}}_k^- = \Phi_{k-1,k} \hat{\mathbf{x}}_{k-1}^+ \quad (2.46)$$

$$\mathbf{P}_k^- = \Phi_{k-1,k} \mathbf{P}_{k-1}^+ \Phi_{k-1,k} + \mathbf{Q}_{k-1} \quad (2.47)$$

where the superscript $(-)$ denotes the estimate value by prediction, while $(+)$ denotes the estimate value after update. \mathbf{P} is the covariance matrix of the state vector, and \mathbf{Q} is the covariance matrix of the process noise. In this step, the Kalman filter uses the state vector estimate and the covariance matrix from the previous step, i.e., $\hat{\mathbf{x}}_{k-1}^+$ and \mathbf{P}_{k-1}^+ , to predict the current state vector and its covariance matrix ($\hat{\mathbf{x}}_k^-$ and \mathbf{P}_k^-), with the aid of the system model (embodied in $\Phi_{k-1,k}$ and \mathbf{Q}_{k-1}). The update step is formulated by:

$$\mathbf{K}_k = \mathbf{P}_k^- \mathbf{H}_k^T \left(\mathbf{H}_k \mathbf{P}_k^- \mathbf{H}_k^T + \mathbf{R}_k \right)^{-1} \quad (2.48)$$

$$\hat{\mathbf{x}}_k^+ = \hat{\mathbf{x}}_k^- + \mathbf{K}_k \left(\mathbf{z}_k - \mathbf{H} \mathbf{x}_k^- \right) \quad (2.49)$$

$$\mathbf{P}_k^+ = \left(\mathbf{I} - \mathbf{K}_k \mathbf{H}_k^T \right) \mathbf{P}_k^- \quad (2.50)$$

where \mathbf{K} is defined as the Kalman gain, \mathbf{R} is the measurement covariance matrix. In this step, the state prediction and measurement are used to update the state estimation and the covariance matrix ($\hat{\mathbf{x}}_k^+$ and \mathbf{P}_k^+). The prediction and update steps from (2.46) to (2.50) run recursively to track the state vector.

2.2.3 Particle Filtering

As discussed in the last section, the assumptions of using Kalman filtering to implement the Bayesian filter are that of linear/Gaussian. However, such assumptions do not hold in many applications of interest. For example, estimation of the state of a user indoors taking into account building map information is normally a high non-linear filtering problem. If a local linearization of equation is sufficient to describe the nonlinearity, then an Extended Kalman filter (EKF) can

be applied to such problem. An EKF normally utilizes the first term in a Taylor expansion of the nonlinear equation, however, for the high-nonlinear filtering problem, the EKF become less effective (Arulampalam et al 2002). On the other hand, a particle filter implements the Bayesian filter by Monte Carlo simulations, and has the ability to model nonlinear transformations of random variables and to represent a much broader space of distributions (Thrun et al 2005), and thus particle filters have been widely used in map-matching techniques.

The key idea of particle filtering is to represent the a posteriori distribution by a set of particles with associated weights. As the number of particles becomes very large, the Monte Carlo characterization can approximate the usual parametric description of the state a posteriori distribution. The estimate of state can be computed based on these particles and the associated weights. In particular, the state at time step t is represented by a particle set denoted by

$$\chi_t \triangleq \{\mathbf{x}_t^1, \mathbf{x}_t^2, \dots, \mathbf{x}_t^n, \dots, \mathbf{x}_t^N\} \quad (2.51)$$

where \mathbf{x}_t^n is the n th particle and N is the number of particles. The state a posteriori distribution defined in (2.40) now can be approximated by

$$bel(\mathbf{x}_t) \triangleq p(\mathbf{x}_t | \mathbf{z}_{1:t}) \approx \sum_{n=1}^N \omega_n^t \delta(\mathbf{x}_t - \mathbf{x}_t^n) \quad (2.52)$$

where ω_n^t is the weight of the n th particle and $\delta(\bullet)$ the Dirac function. Just like in the implementation of the Bayesian filer, a particle filter constructs the state a posteriori distribution recursively over time. Since a particle filter represents the distribution by sets of particles, it constructs the particle set χ_t recursively from χ_{t-1} . A particle filter comprises the following steps:

- Particle initialization

The initial set of particles χ_0 is simulated from the state initial distribution $p(\mathbf{x}_0)$ and the associated weights are set to $\omega_n^t = 1/N, n = 1, 2, \dots, N$.

- Prediction

In this step, each particle in χ_{t-1} from the previous step is propagated according to the known system state model. The particle set obtained in this step represents the state prediction $p(\mathbf{x}_t | \mathbf{z}_{1:t-1})$ or $\overline{bel}(\mathbf{x}_t)$. This step implements the prediction step of Bayesian filer as defined in (2.42).

- Particle weight update

This step updates the weight for each particle by

$$\omega_t^n = p(\mathbf{z}_t | \mathbf{x}_t^n) \omega_{t-1}^n \quad (2.53)$$

As can be seen, the measurement likelihood condition on the particle \mathbf{x}_t^n is used to weight the corresponding particle. This is to incorporate the measurements into the particle set. Other information can be incorporated into the particle set in this step. With map-matching, for example, the particles can be weighted according to the map constraints, e.g., a particle associated with the position in inaccessible areas will be assigned a low weight. Up to this step, the particles set χ_t as well as the particle weights $\omega_t^n = 1/N, n = 1, 2, \dots, N$ can be used to approximate the state a posteriori distribution $p(\mathbf{x}_t | \mathbf{z}_{1:t})$ or $bel(\mathbf{x}_t)$.

- Resampling

In principle, the state a posteriori distribution $p(\mathbf{x}_t | \mathbf{z}_{1:t})$ was obtained in the last step and the filter can move forward to the next iteration. In practice, however, a common problem with the

particle filter is the so-called degeneracy problem; that is, after a few iterations, a large number of particles have weights close to zero and they cannot approximate the state a posteriori distribution. From this point of view, a resampling step is a critical point for the particle filter. The basic idea of resampling is to remove the particles with weights that are too low and multiple the numbers of particles with high weights. However, frequent resampling may lead to a loss of diversity due to the repetition of many particles. Therefore, prior to the resampling, a suitable measure of the degeneracy is needed and the effective number of particles, N_{eff} , is normally used which is calculated by

$$N_{\text{eff}} = \frac{1}{\sum_n^N (\omega_n^k)^2} \quad (2.54)$$

A small N_{eff} means a severe degeneracy, and when N_{eff} is below a threshold, resampling is triggered. After resampling, the particle weights are reset to $1/N$ and the filter can move forward to next iteration.

- State estimation

The state vector can be estimated in every iteration by using the state a posteriori distribution and a certain criterion such as maximum likelihood or maximize a posteriori.

2.3 Static Camera Positioning and CV Processing for Object Detection

Given advances in CV algorithms and increased computation power of computers, the ability to localize and track people using security cameras is now important. Figure 2.4 depicts a static camera positioning system which mainly consists of two key components, namely object

detection and coordinate transformation. Suppose that a user moves in the Field of View (FOV) of a static camera and is captured on video. For each video frame, a CV processing must first detect the object in the image plane and determine its position in the image coordinate in terms of pixels. Then a transformation is used to transform the detected object from image coordinates to the local or other coordinates. The transformation of the object detection resulting in the pixel coordinates to another coordinates system involves camera calibration. Appendix B describes this process in detail. It is shown that the camera calibration process involves the joint estimation of a set of parameters, namely intrinsic and extrinsic parameters, a complex processing. As discussed in Chapter 1, one main objective of the thesis is to quickly set up a security camera and extract useful information for positioning. In Chapter 5, a method is proposed where object detection results from an uncalibrated security camera are used to enhance a RSS-based positioning system. Note that the focus of the thesis is not to improve CV processing for object detection; instead, the objective is to make use of the CV results to enhance RSS-based positioning. To better understand CV object detection, related CV algorithms for object detection are briefly introduced next.

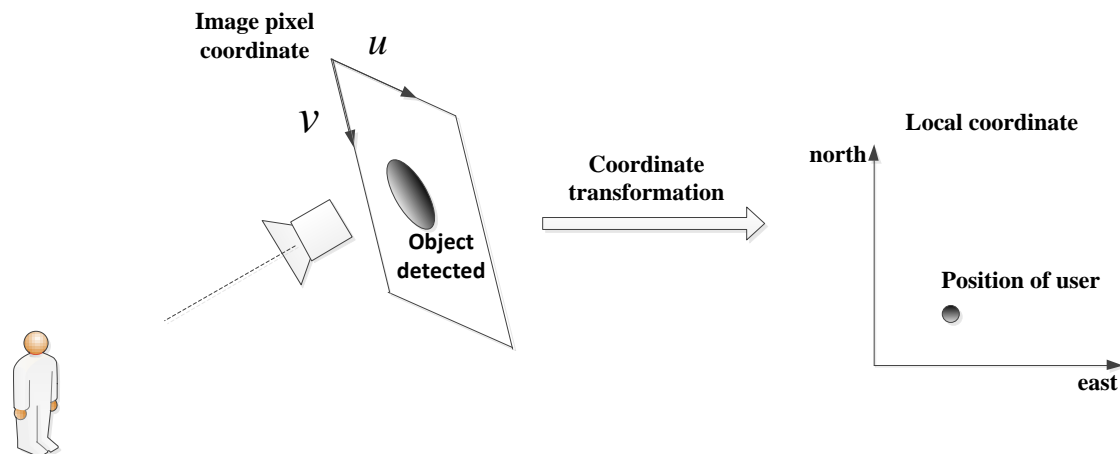


Figure 2.4: Static camera positioning system

2.3.1 Background Subtraction for Object Detection

A static or security camera mostly looks at the same background, which is normally not interesting. What is interesting is when a target (e.g., a person, a vehicle) enters the scene (Bradski and Kaehler, 2008). Therefore, object detection generally refers to isolating objects or part of objects from the background, which is the first step of using a static camera to locate a user.

Background Subtraction (BGS) techniques (or background differencing) are widely used for detecting moving objects in video frames from a static camera. This thesis briefly reviews the main BGS methods. A thorough review of the BGS techniques is provided in (Piccardi, 2004). The simplest form of BGS takes an image with the background only and the difference between the background image and the current video frames is used for object detection. After applying thresholding to the difference, a binary image is created which segments the foreground objects from the background (Van den Berghe et al 2011). One major limitation of such a simple BGS method is the fact that the background image is not static. For example, the varying luminance conditions, furniture being moved and camera being moved slightly can make background image become outdated and useless. To detect an object effectively, a background image must be an exact representation of the scene with no moving objects and must be regularly updated, while avoiding foreground objects to be absorbed to the background image. The major difference among various BGS techniques lies mainly in the models of the ‘background image’ and the ways in which it is obtained.

To update the background image regularly, a set of previous pixel values is needed to obtain the background image. Running Gaussian average method proposed by (Wren et al 1997) models the

background independently at each pixel location $[i, j]$. Specifically, the pixel's values at each pixel location are Gaussian distributed and the mean and variance of the Gaussian model are computed by the last n pixel values. To avoid fitting the Gaussian PDF from scratch at each new frame, a running average is used to compute the mean as

$$\mu_t = \alpha I_t + (1 - \alpha) \mu_{t-1} \quad (2.55)$$

where I_t is the current pixel value, μ_t is the previous average and α is an empirical weight used as a trade-off between stability and a quick update (Piccardi, 2004). For each frame time, a pixel value I_t is determined as a foreground pixel and the following inequality holds

$$|I_t - \mu_t| > k\sigma_t \quad (2.56)$$

Otherwise I_t is classified as a background pixel. In (2.56), σ_t is the variance of the Gaussian model in a pixel location and k is a value that controls the detection threshold. One advantage of running the Gaussian average method is its low memory requirement: two parameters, i.e., mean and variance, are needed to represent the background for each pixel location (Piccardi, 2004). Another similar method is the temporal median filter where the median value from the last n frame is used as the background at each pixel location. The performance comparisons of the two BGS methods were reported in some research (Lo and Velastin, 2001, Cucchiara et al 2003). One advantage of the temporal median filter method is computational efficiency, although this method requires a set of previous images to be stored in order to obtain the median values, which requires more memory than the running Gaussian average method.

The two BGS methods previously discussed can adapt to permanent change in the scene, for example, furniture being moved; however, changes in the background are not always permanent. Specifically, the background objects can change in the previous n frames used to extract the

background image. For example, when tree leaves move in the wind, a background pixel may change between floor and leaves. To deal with such a multiple background problem, (Stauffer and Grimson, 1999) use a mixture of Gaussian models to model the distribution of the pixel values for each pixel location in the background as follows:

$$p(x_t) = \sum_{k=1}^K \omega_{k,t} \eta(x_t - \mu_{k,t}, C_{k,t}) \quad (2.57)$$

where K Gaussian distributions are used. In (2.57), $\omega_{k,t}$ is the weight for the k th Gaussian model, $\mu_{k,t}$ is the mean of the k th Gaussian model, $C_{k,t}$ is the covariance matrix of the K Gaussian distributions and $\eta(\bullet)$ represents the PDF of Gaussian distribution. With such a mixture of Gaussian models to represent the background, a pixel value in the current image is used to compute the likelihood. If this pixel value lies within a certain threshold (falls in one Gaussian), it will be determined as a background pixel. On the other hand, if it falls outside all Gaussian models, it will be determined as foreground object.

The output of the BGS method is a binary image which segments the foreground objects from the background. This image shows the detected objects that are not stationary (Van den Berghe et al 2011). Figure 2.5 gives an example of the object detection results as compared to the original image.

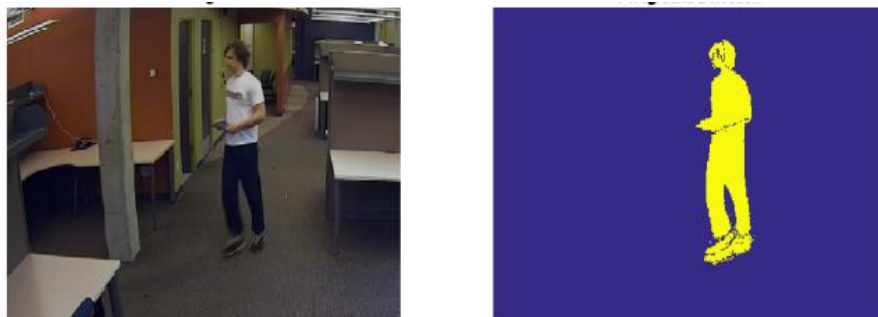


Figure 2.5: Original image(a) and object detected (b) (Nielsen et al 2016)

Chapter Three: Indoor Received Signal Strength Measurement Characterization

As discussed in Chapter 1, a wireless Received Signal strength (RSS)-based indoor positioning system suffers from considerable RSS measurement uncertainty, and the main theme of this thesis is to investigate techniques to enhance RSS-based indoor positioning. Since the main measurements in addressing this hypothesis are the RSS measurements, it is essential to understand their characteristics in indoor environments prior to investigating enhancing techniques. This chapter characterizes RSS pathloss as well as uncertainties in RSS, especially the uncertainty incurred by human body shadowing effect through experimental data collected in various outdoor and indoor environments. The results of the statistical data analysis help in characterizing the RSS measurements and form the basis for the following Chapter 4 and Chapter 5. Specifically, Chapter 4 proposes an empirical model for RSS body shadowing effect based on the characterization made in this chapter; the algorithms proposed to enhance RSS-based positioning in Chapter 4 and Chapter 5 are tested using methods based on pathloss models characterized in this chapter.

3.1 Experimental Equipment and Environments

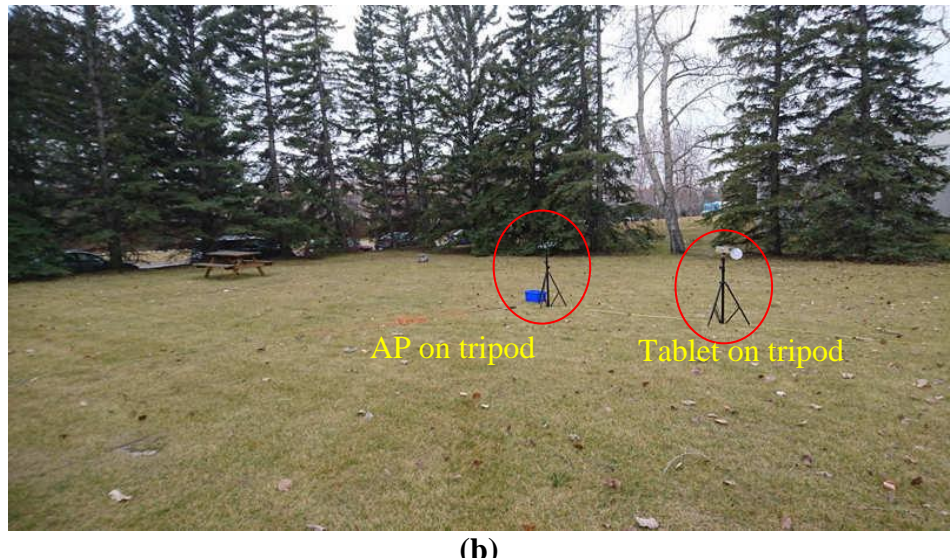
The RSS measurements for characterization are collected using IEEE 802.11 Wi-Fi Access Points (APs) and mobile devices. They are all consumer grade units. This is because most RSS-based positioning systems today are based on Wi-Fi networks. In the experiments described below, Wi-Fi routers were used to transmit 2.4 GHz and 5 GHz signals simultaneously and a Google Nexus tablet was used to receive the signals and record the RSS measurements using an

Android application developed for this purpose as described in Appendix A. The RSS measurements recorded were then post-processed for analysis.

Experimental data was collected in several outdoor and indoor environments. Since there are fewer shadowing, multipath and interfering effects in outdoor environments than indoors, the RSS measurements collected outdoors will serve as references. Figure 3.1 shows two outdoor environments used for data collections. RSS measurement collected in indoor environments can then be compared to these references in order to see how the RSS characteristics deviate from the references due to complex indoor wireless propagations variables. The indoor environments for data collection are shown in Figure 3.2. The indoor environments include hallways in several campus buildings of the University of Calgary: the ENA engineering built in the 1960s, the ICT office building built in the 2000s and the EEEL modern building built in 2010s, as well as a typical office building, Appropolis office built in the 1960s. Hallways and office space represent two typical environments that the indoor positioning could be used in (e.g., self-locating in a campus, employee tracking). Different materials could be used for buildings constructed in different ages and result in different indoor signal propagations.



(a)



(b)

Figure 3.1: Outdoor environments for data collection (a) parking lot, (b) playground

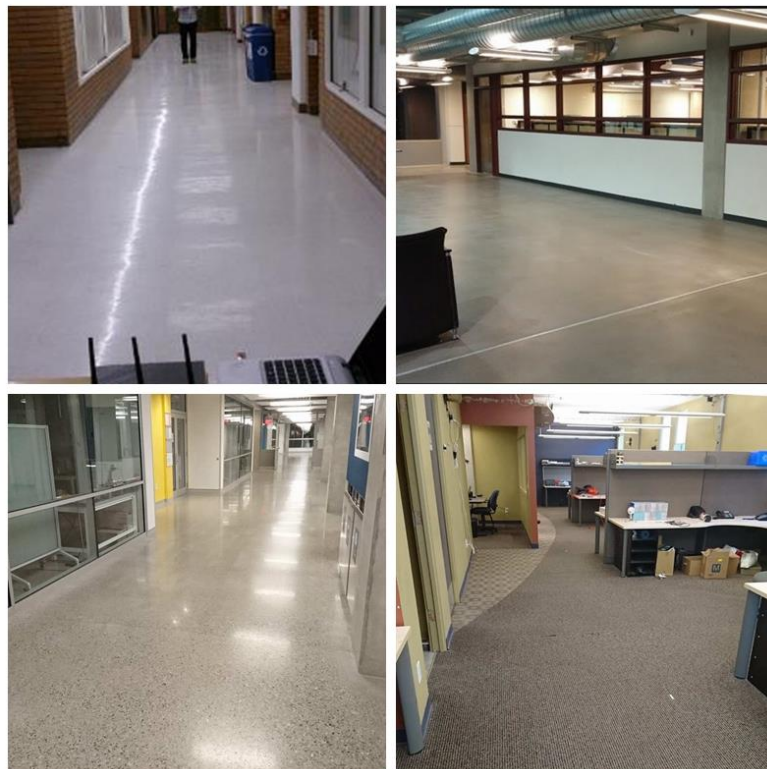


Figure 3.2: Indoor environments for data collection: hallway in ENA building (top left), hallway in ICT building (top right), hallway in EEEL building (bottom left), Appropolis office (bottom right)

As introduced in Chapter 1, RSS measurements can be affected by many factors, including hand-grip (Della Rosa et al 2011). To eliminate the hand-grip impact induced variability on the results and in order to focus purely on the characterization of wireless propagations and human body shadowing effects, the mobile device (tablet) was placed in a tripod during data collections as shown in Figure 3.1 (b).

3.2 Pathloss Characterization

Since the positioning algorithms in this thesis are based on pathloss model, the first characteristic interested herein is the pathloss which is the overall decrease in signal power between the transmitter (Wi-Fi AP) and receiver (mobile device). Pathloss is a function of the transmitter-receiver distance (T-R distance). The pathloss parameters trained from the RSS measurements together with the pathloss models (e.g., log-distance pathloss model introduced in Chapter 2) can be used to estimate the T-R distance for trilateration algorithm used in Chapter 5, or to compute the measurement likelihood for the maximum likelihood positioning algorithm used in Chapter 4.

3.2.1 Outdoor Experiment for Pathloss Characterization

The experiment was first conducted in an outdoor environment, a parking lot in the front of the CCIT building shown in Figure 3.1(a). In the experiments, the Wi-Fi AP and the tablet were placed to the same height and the AP and tablet always faced each other in same pattern. This is to eliminate the antenna radiation variations in the Wi-Fi transceiver from the pathloss estimates. A set of test points (TPs) shown in Figure 3.3 were chosen along the transmitter-receiver line (T-R line) and RSS measurements were collected at each of these TP for 70 s (which results in

about 100 RSS measurements at each TP). Figure 3.3 depicts the experiment scenario. Then the mean and standard deviation of the RSS measurements for each TP for analysis were computed.

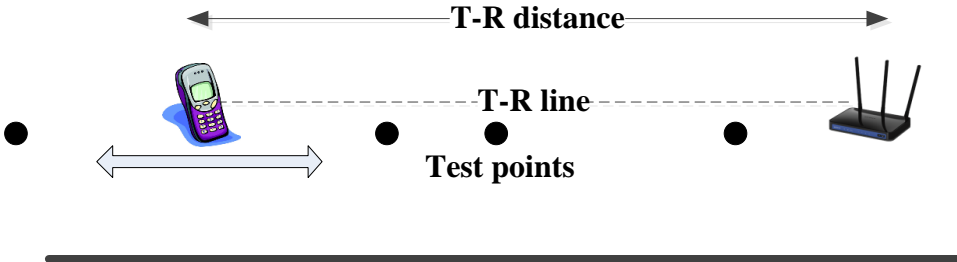


Figure 3.3: Experiment for pathloss characterization

Figure 3.4 shows the scatter plots of the raw RSS measurements as well as the mean and standard deviation versus T-R distance, for both 2.4 GHz and 5 GHz signals. Since an outdoor environment undergoes less shadowing and multipath effects, the corresponding pathloss exponent of log-distance pathloss model is supposed to be close to 2, the value for free space propagation. A log-distance pathloss model with exponent fixed to 2 is thus fitted to the RSS measurements to investigate signal propagation and the results are represented by blue dash plots in Figure 3.4, where n denotes the pathloss exponent. Generally, the free space pathloss model shows a reasonable fit to both the 2.4 GHz and 5 GHz RSS measured values. Interestingly, there is weak undulation associated with the pathloss in each signal band. This is because the coherent ground reflection multipath causes undulations which can be understood using Fresnel zones (Rappaport, 1996). The standard deviation (represented by the red bar for each RSS mean value) is smaller for 5 GHz signals than for 2.4 GHz, which is consistent with the results reported by researchers such as, Farshad et al (2013) and Lui et al (2011) and Yu et al (2014).

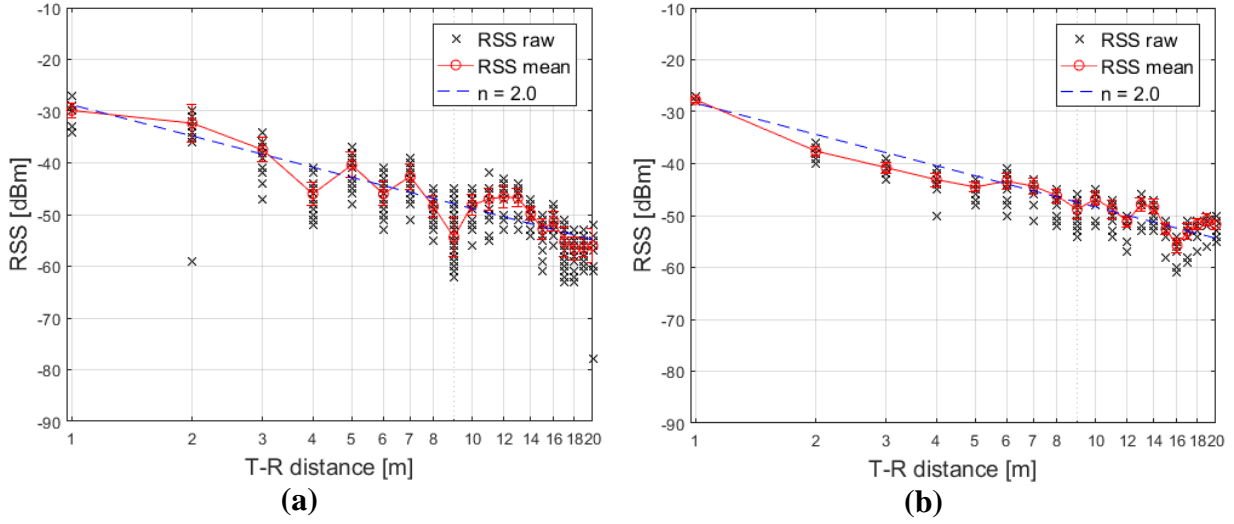


Figure 3.4: : Scatter plot, mean, standard deviation of RSS measurements and pathloss model fitted in an outdoor environment (a) 2.4 GHz signals (b) 5 GHz signals

3.2.2 Indoor Experiment for Pathloss Characterization

Experiments with the same setup were then conducted in the hallways in ENA, ICT, EEEL buildings, as shown in Figure 3.2 (a) (b) (c). The experimental results are shown in Figure 3.5, Figure 3.6, Figure 3.7 for ENA, ICT and EEEL buildings, respectively. A log-distance pathloss model is fitted to the measurements for each environment and the results are represented by blue plots in the corresponding figure. Note that in this case the pathloss exponent in the fitting model is not fixed to 2 as in outdoor case. Two conclusions can be drawn from the results:

- 1) The pathloss exponents for both 2.4 GHz and 5 GHz signals are less than 2, the value for the free space. This is because signal propagation in a hallway (or tunnel) in the LOS case may act as a waveguide, resulting in a pathloss exponent less than 2 (an ideal waveguide model has no loss and the pathloss exponent is zero). Specifically, in addition to the LOS signal, considerable multipath signals are received and they contribute to the

resultant signal constructively. This is consistent with the collusion for pathloss exponents in building LOS case described in (Rappaport, 1996).

- 2) There are a considerable number of outliers in the 2.4 GHz RSS measurements in indoor environments as highlighted by the green ellipses in Figure 3.5-Figure 3.7, while there are few outliers in 2.4 GHz outdoor case and 5 GHz indoor and outdoor cases. This is because many radio devices are operating in the 2.4 GHz industrial, scientific and medical (ISM) radio band such as Bluetooth devices, microwave ovens and wireless phones. For example, in EEEL building there are up to several hundreds of individual 2.4 GHz emissions from various transmitters. The highly-crowded interferences sources in the 2.4 GHz frequency band may affect the performance of the RSS measuring algorithm in Wi-Fi receivers as discussed in Chapter 2. The outliers significantly increase the variance of the 2.4 GHz signal indoors.

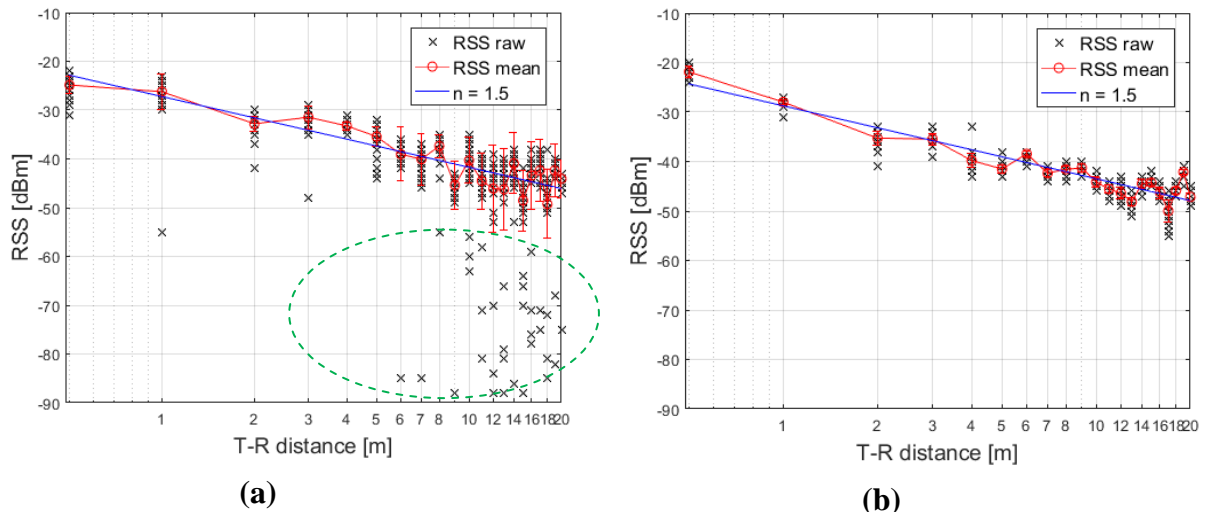


Figure 3.5: Scatter plot, mean, standard deviation of RSS measurements and pathloss model fitted in ENA building (a) 2.4 GHz signals (b) 5 GHz signals

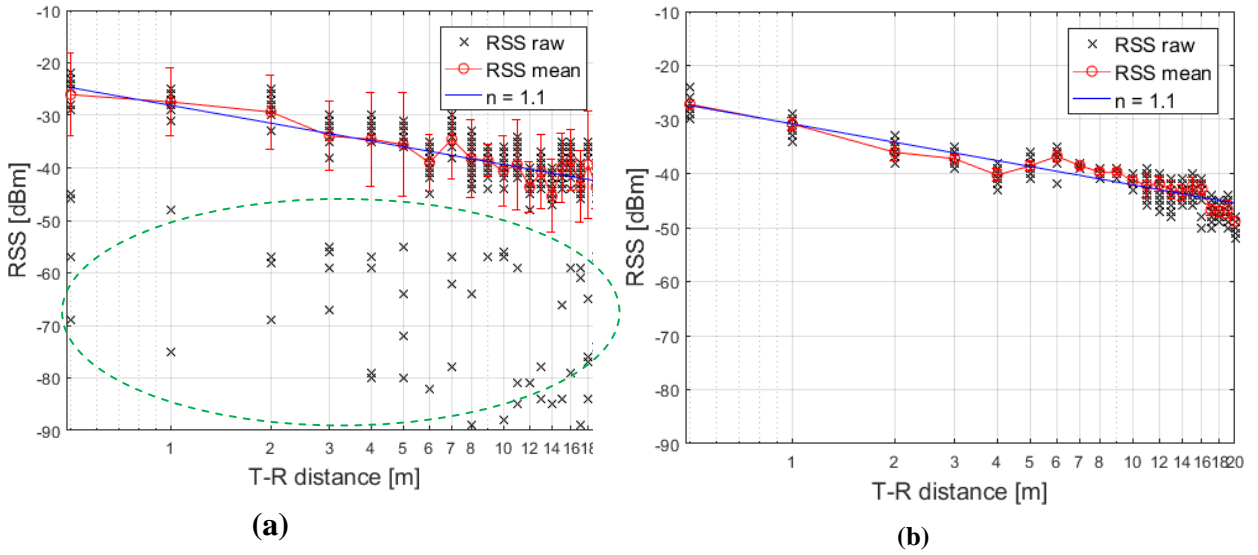


Figure 3.6: Scatter plot, mean, standard deviation of RSS measurements and pathloss model fitted in ICT building (a) 2.4 GHz signals (b) 5 GHz signals

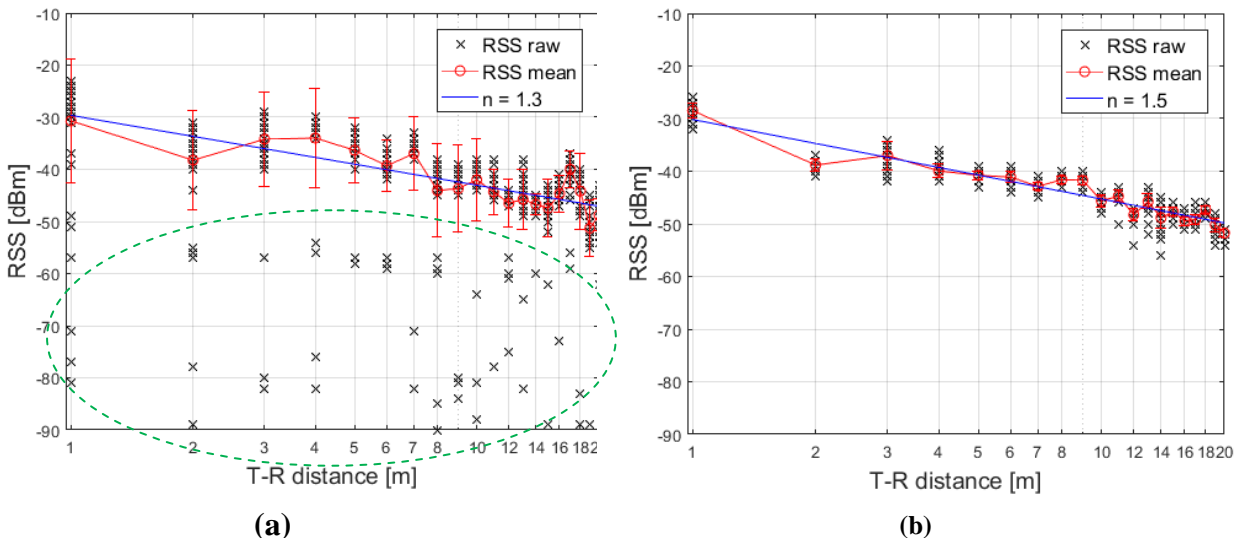


Figure 3.7: Scatter plot, mean, standard deviation of RSS measurements and pathloss model fitted in EEEEL building (a) 2.4 GHz signals (b) 5 GHz signals

The previous experiments only provide the pathloss characterization for the indoor LOS case (all TPs are in LOS condition). To further investigate the pathloss for a hybrid LOS-NLOS scenario

which is a more general case for indoor positioning applications, the same AP used for the previous experiments was deployed in the Appropolis office building as shown in Figure 3.2 for data collection. The location of the AP and TPs for data collections are shown in Figure 3.8. As can be seen, the RSS data collection at these TPs includes both LOS and NLOS cases. Unlike the previous experiments, the TPs in this experiment do not reside along the T-R line. Correspondingly, one assumption of this experiment is that the antennae of the Wi-Fi APs and tablet both have an omni-directional beam pattern.

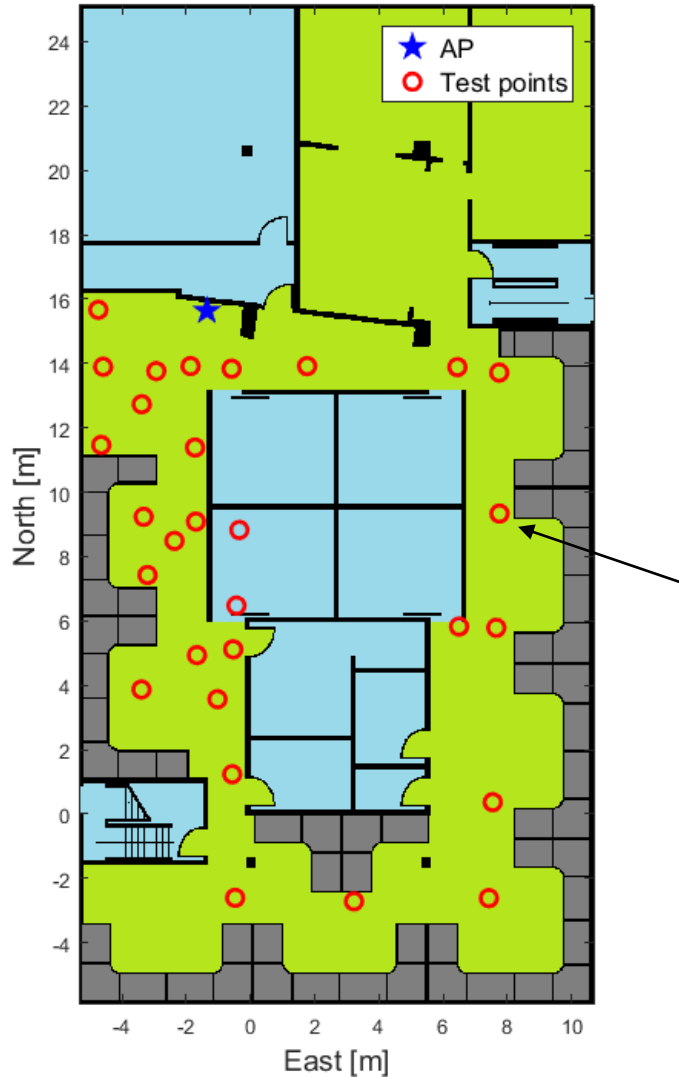


Figure 3.8: Experimental setup for RSS characterization in Appropolis office

Figure 3.9 shows scatter plots of the raw RSS measurements as well as the means and standard deviations versus T-R distance for both 2.4 GHz and 5 GHz signals. As can be seen, the pathloss exponents increase to about 4. This is because for the TPs in NLOS condition, the signals are obstructed by furniture, walls, dividers, and the obstruction of these signals causes additional losses in the received signal power. In addition to the outlier, the 2.4 GHz RSS measurements further spread in some TPs. For example, for the TP highlighted in Figure 3.8 by the black arrow, Figure 3.10 shows the histograms of the RSS measurements for the 2.4 GHz and 5 GHz signals. For the 2.4 GHz RSS measurements, it seems there are two peaks in the distribution, which further increase the variation in the 2.4 GHz RSS values considerably.

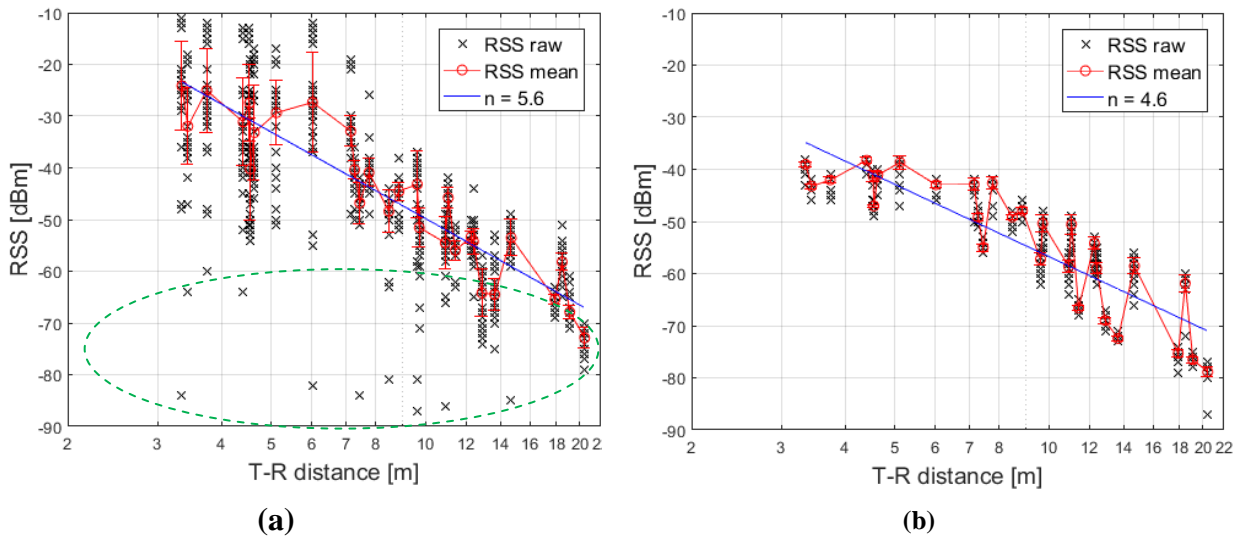


Figure 3.9: Scatter plot, mean, standard deviation of RSS measurements and pathloss model fitted in Appropolis building (a) 2.4 GHz signals (b) 5 GHz signals

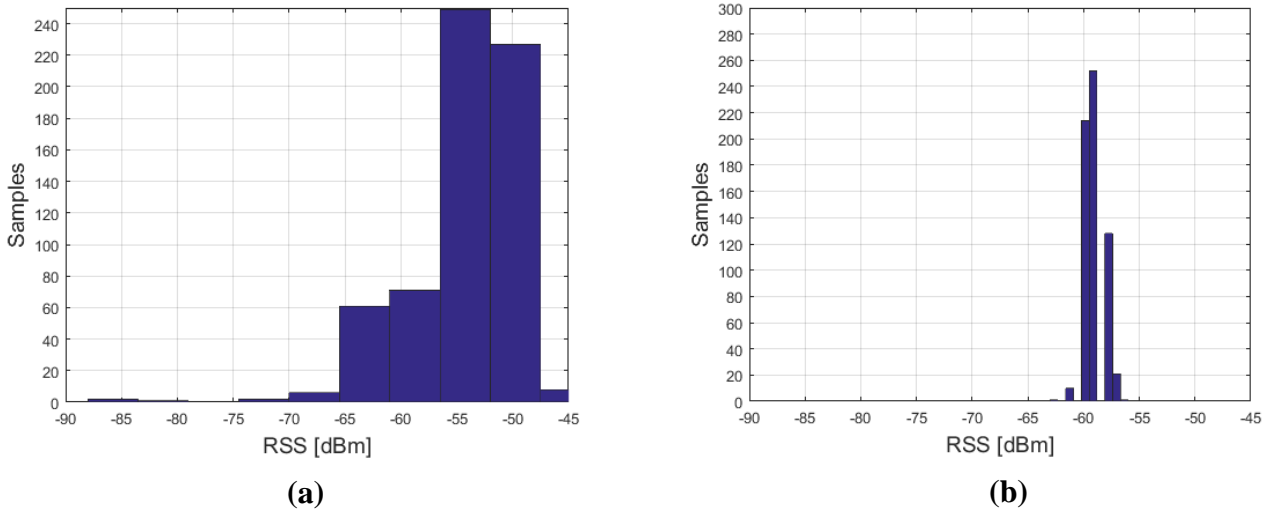
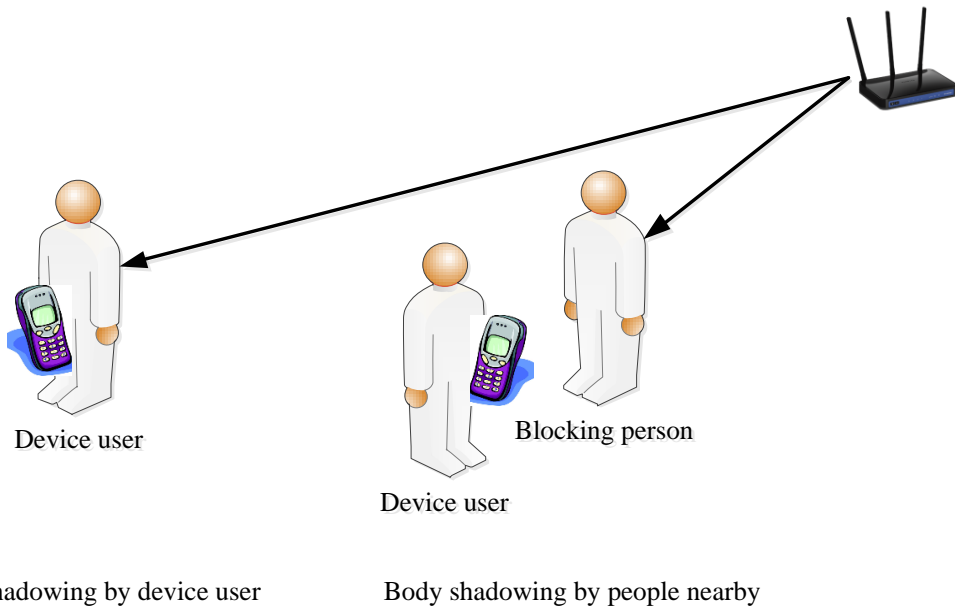


Figure 3.10: Histogram of RSS measurements at the location identified by an arrow in Figure 3.8 for (a) 2.4 GHz signals, (b) 5 GHz signals

3.3 Body Shadowing Effects on RSS Measurements

As discussed in Chapter 1, RSS loss due to human body shadowing has shown to be a source of error for RSS-based positioning. Human body shadowing generally can be caused by the device user and/or other people near the mobile device as depicted in Figure 3.11. For a body shadowing effect caused by people near the device user, the distance between mobile device and the blocking people, the number of the blocking people nearby, etc. can be used to characterize the body shadowing effect (Chen et al 2005). while the effects caused by the device user can be associated to the user's gesture and heading (Li et al 2015). Essentially, these two blocking cases can be generalized to a scenario described by the Figure 3.12, where one blocking person is considered to start the investigation. First define two quantities, namely, blocking distance and blocking angle, for characterizing the body shadowing effect on RSS as shown in Figure 3.12. The blocking distance is defined as the distance between the mobile device and the human body blocking the LOS path between the AP and mobile device, and the blocking angle is defined as

the angle between the body-device line and T-R line. When the human body is very close to the mobile device (small blocking distance, e.g., less than several decimetres), it represents the user body shadowing case; as the blocking distance increases, it can be used to represent the shadowing case caused by a blocking person other than the user. To quantify the body shadowing effects on RSS, define the RSS body shadowing loss as the value calculated by subtracting the RSS value in the shadowing case from the one in the no-shadowing case, and therefore the unit of RSS body shadowing loss is dB since RSS measurements are given in unit of dBm by the experimental devices used in this thesis. Theoretically, the RSS body shadowing loss should be a positive value. The dependence of RSS body shadowing loss on blocking distance and blocking angle will be characterized using experiments described in the next section.



Body shadowing by device user

Body shadowing by people nearby

Figure 3.11: Body shadowing effect caused by device user and/or people nearby

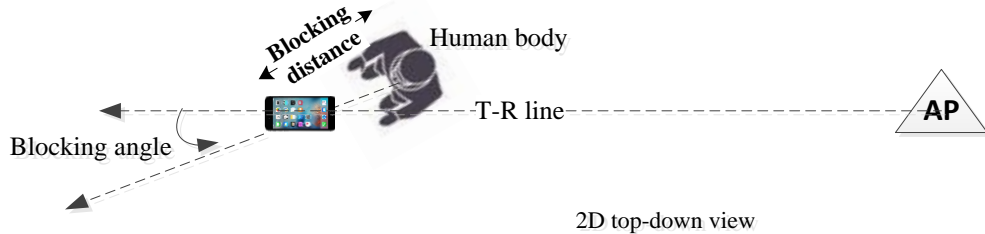


Figure 3.12: A generalized human body shadowing scenario

3.3.1 Human Body Shadowing Effect as a Function of Blocking Distance

3.3.1.1 Outdoor Experiment for Analysis of Blocking Distance Affecting Body Shadowing

To characterize the dependence of RSS shadowing loss on blocking distance, an experiment was conducted in the outdoor environment shown in Figure 3.1(a). Figure 3.13 shows the design of the experiment, where a blocking person stands at a set of TPs between the tablet and Wi-Fi AP to block the LOS path totally (blocking angle being 0°). RSS measurements were collected for each TP, and then the mean and standard deviation of the RSS measurements for each TP were computed for each blocking distance for analysis.

Figure 3.14 shows the TP means and standard deviations of RSS shadowing loss versus the blocking distance. For both 2.4 GHz and 5 GHz signals, the mean of RSS shadowing losses are positive values. This indicates that on average, the RSS shadowing loss effect are present for all the blocking distance in the outdoor environment. The trend of the RSS shadowing loss mean value presents a ‘U’ shape, i.e., larger loss values present for both small and large blocking distance. The large loss for a small blocking distance is due to the proximity between the person and mobile device, while for a large blocking distance, this is due to the proximity between the Wi-Fi AP and the person. However, for 2.4 GHz signals the considerable variation in RSS obscures this trend. In other words, for the 2.4 GHz signals, the impact of body shadowing effect on RSS is not as strong as that of other sources of uncertainty. Thus, for the 2.4 GHz signals, it is

very difficult to characterize the body shadowing effect and there is a relatively small to negligible loss in information by ignoring the body shadowing.

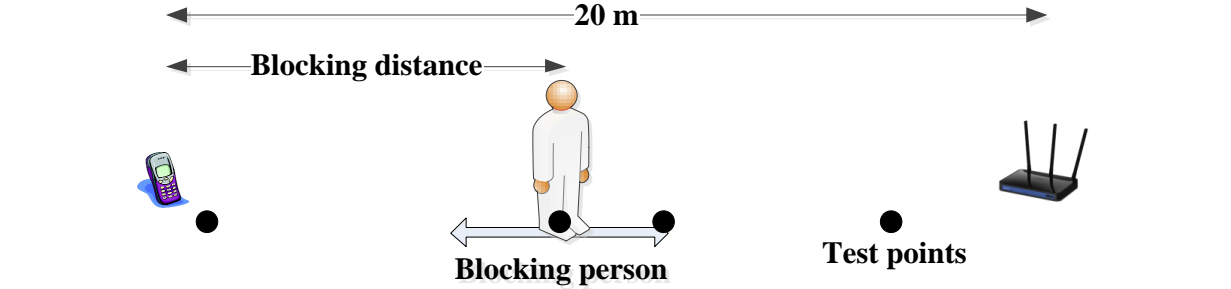


Figure 3.13: Experiment design for analyzing dependence of RSS body shadowing loss on blocking distance

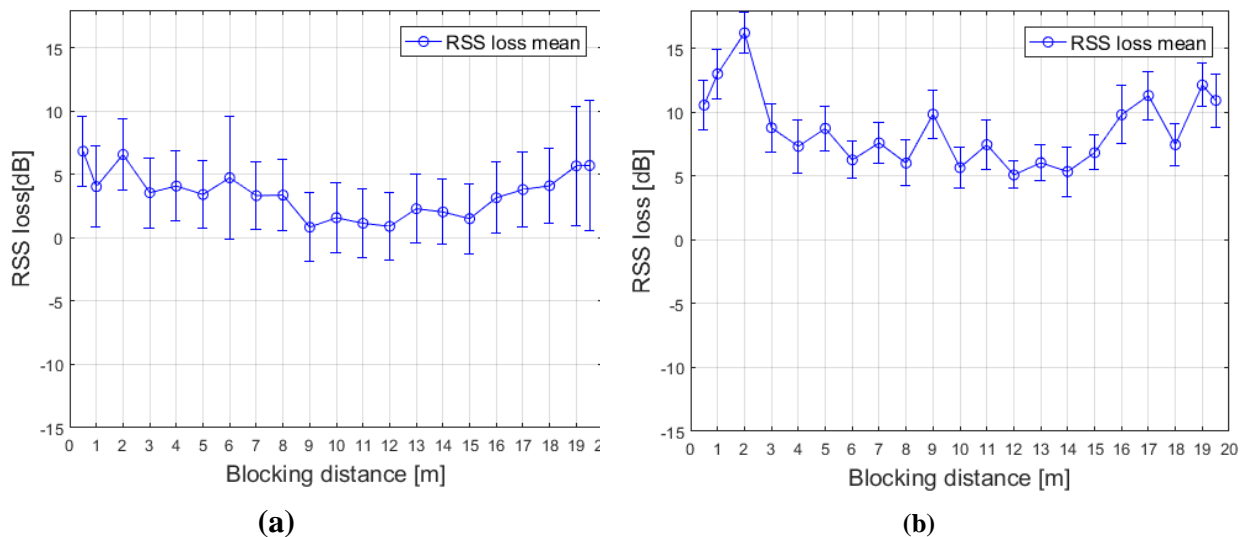


Figure 3.14: Mean and standard deviation of RSS shadowing loss as a function of blocking distance in an outdoor environment (a) 2.4 GHz signals, (b) 5 GHz signals

3.3.1.2 Indoor Experiment for Analysis of Blocking Distance Affecting Body Shadowing

Experiments with the same setup were next conducted in the hallways in ENA, ICT and EEEL buildings shown in Figure 3.2 (a) (b) (c), and the results are shown in Figure 3.15, Figure 3.16 and Figure 3.17 for the three indoor environments, respectively. For 2.4 GHz RSS results, the larger variations in indoor environments further weaken the dependence of RSS shadowing loss on the blocking distance. For the 5 GHz results, two interesting observations can be seen when compared to the previous outdoor results:

- 1) The ‘U’ shape-like dependence of the RSS shadowing loss on blocking distance becomes more definite than in the outdoor case. Interestingly, the RSS shadowing loss drops to approximately zero for medium blocking distance (the blocking person is neither too close to the tablet nor the AP), meaning that the RSS shadowing loss indoors is negligible when the blocking person is neither too close to the mobile nor the AP. This is because the multipath signals in indoor environments also contribute to the RSS.
- 2) When the blocking person is close to the mobile, the loss starts showing up when the blocking distance is approximately 2-3 *m*, and the RSS shadowing loss can be up to about 10 *dB* (ENA building case). When the blocking person is close to the AP, the loss value can be up to about 3 *dB*, and it starts showing when the distance between the blocking person and AP is approximately 2-3 *m*.

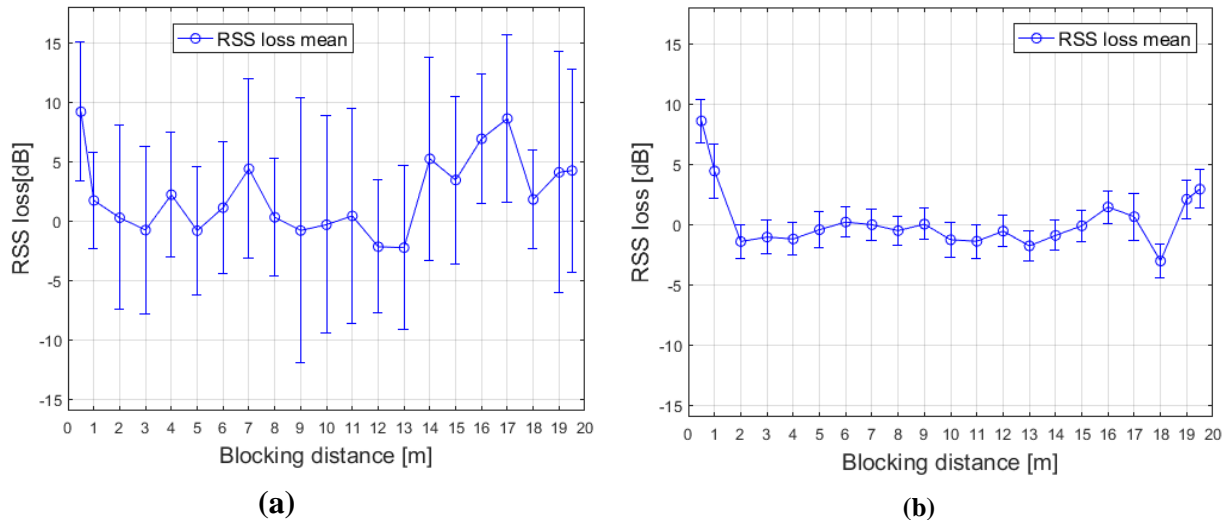


Figure 3.15: Mean and standard deviation of RSS shadowing loss as a function of blocking distance in ENA building (a) 2.4 GHz signals, (b) 5 GHz signals

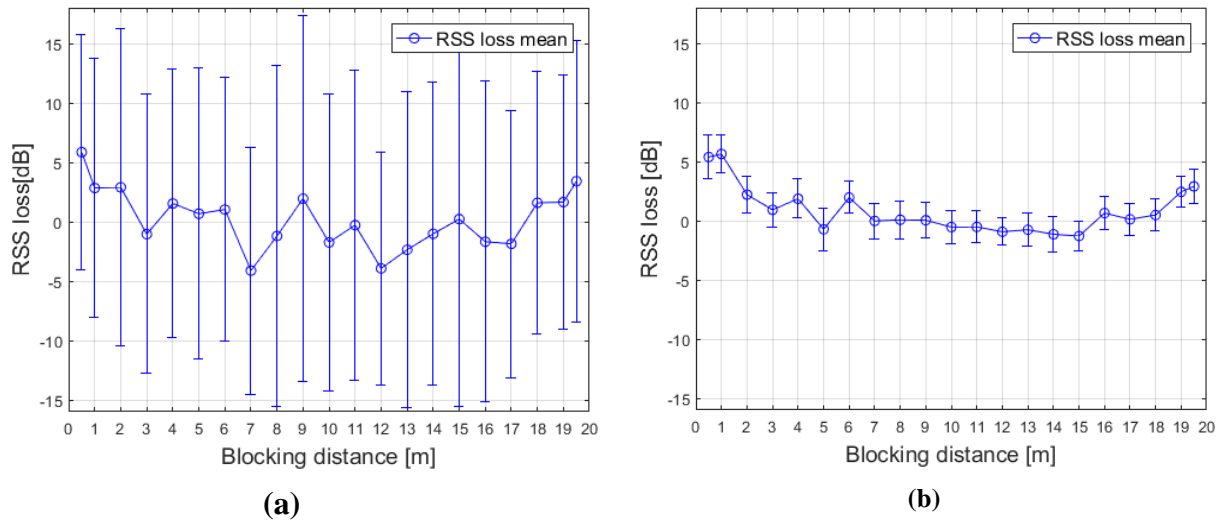


Figure 3.16: Mean and standard deviation of RSS shadowing loss as a function of blocking distance in ICT building (a) 2.4 GHz signals, (b) 5 GHz signals

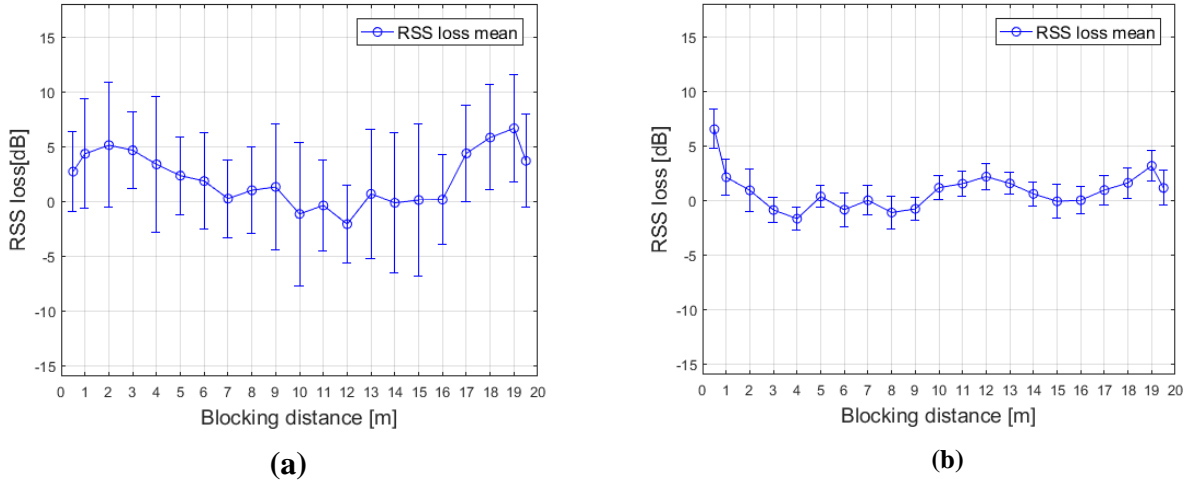


Figure 3.17: Mean and standard deviation of RSS shadowing loss as a function of blocking distance in EEEL building (a) 2.4 GHz signals, (b) 5 GHz signals

Two main conclusions can be drawn from these results:

1. For 2.4 GHz Wi-Fi signals, sources of uncertainty other than body shadowing dominate RSS variations. These sources of uncertainty could be multipath signals, interference in the ISM band, etc. For the 2.4 GHz signals, it is very difficult to characterize the body shadowing effect and there is a relatively small to negligible loss in information by ignoring it. For the remainder of the thesis, the body shadowing effect is only investigated for the 5 GHz signal for which RSS fluctuations show strong dependence on body shadowing.
2. Second, for 5 GHz RSS results, the RSS body shadowing loss becomes apparent only when the human body is close to either the mobile or the AP (less than about 2-3 m). For a normal AP deployment, a person is rarely too close to APs. On the other hand, a mobile being close to a person is a very common positioning scenario, e.g., a mobile user holding the device out front in order to self-locate. In the next section, RSS body

shadowing loss will be characterized for this scenario when the blocking angle is taken into account.

3.3.2 Human Body Shadowing Effect as a Function of Blocking Angle

3.3.2.1 Outdoor Experiment for Analysis of Blocking Angle Affecting Body Shadowing

This section characterizes the dependence of RSS shadowing loss on blocking angles, with a small blocking distance (several decimetres), which is a common shadowing scenario caused by the user. To do this, an experiment was first conducted in the outdoor environment as shown in Figure 3.1(b). The Wi-Fi AP and the tablet were installed with the same height and the T-R distance is 3 m. The tablet was placed on a tripod as shown in Figure 3.1 (b) and a person stood close to and facing the tablet without touching it (0.3 m blocking distance). This is to simulate the scenario where a mobile user holds a device out front while avoiding the hand-grip effect induced variability on the RSS shadowing loss results. Figure 3.18 depicts the design from a top-down view. During the data collection, a blocking person changed heading by standing at a set of TPs around the tablet, as shown in Figure 3.18, so the blocking angle ranged from -180° to 180° . Note that the experiment was designed to avoid the rotation of the tablet. This is to avoid variation in the antennae radiation affecting the RSS body shadowing loss estimation.

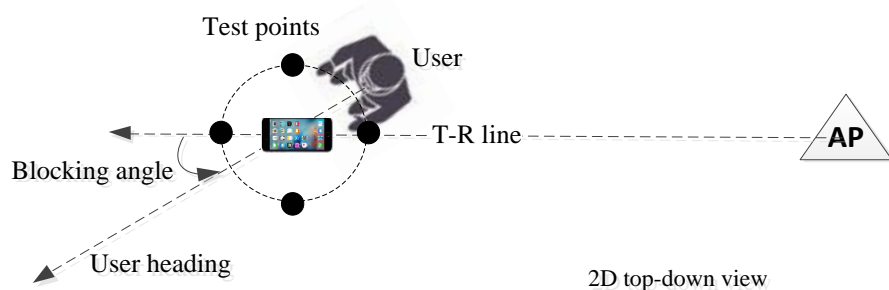


Figure 3.18: Experiment for dependence of RSS body shadowing loss on blocking angle

RSS measurements were collected for each TP (or each blocking angle) and the mean and standard deviation of the body shadowing loss are computed and shown by the blue plots in Figure 3.19 versus the blocking angle. For the 5 GHz RSS, it clearly shows the dependence of the RSS shadowing loss on blocking angle. The loss can be more than 10 dB when the tablet is totally blocked (blocking angle being 0° as described in Figure 3.18) and becomes less significant as the blocking angle deviates from 0° by 60° to 90°.

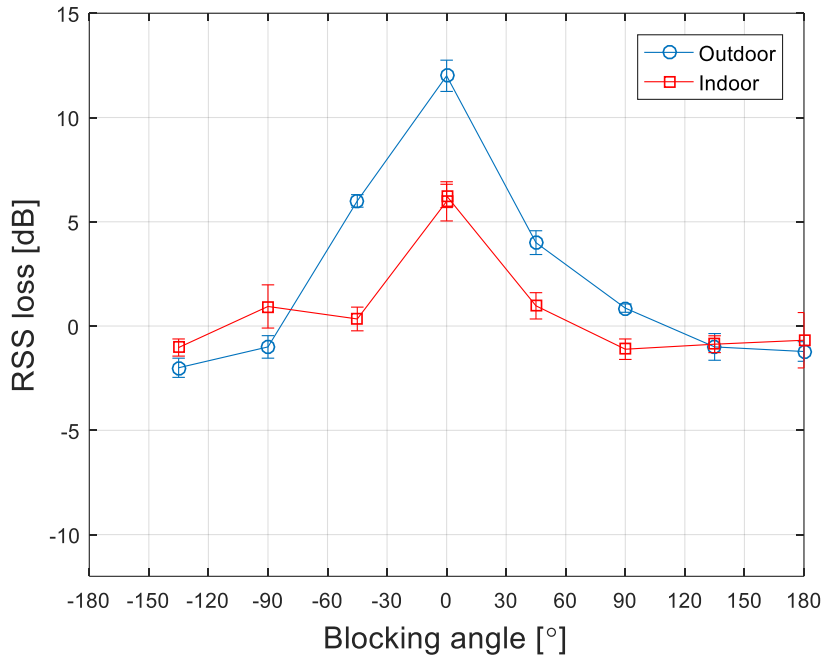


Figure 3.19: Mean and standard deviation of 5 GHz RSS shadowing loss as a function of blocking angle in outdoor and indoor environments

3.3.2.2 Indoor Experiment for Analysis of Blocking Angle Affecting Body Shadowing

Experiment with the same setup was then conducted in the Appropolis office. Figure 3.20 shows the locations of the AP (denoted by AP27) and the tablet location (denote by L1). The results are shown by the red plot in Figure 3.19. While the dependency of body shadowing loss on blocking angle is still definite, as compared to the outdoor case, the loss value is generally reduced. This is

because the multipath signals in indoor environments also contribute to the RSS, which indicates that the RSS shadowing loss is affected by multipath signals indoors. In order to explore this further, the tablet was placed at another two locations (shown in Figure 3.20 by L2 and L3) to collect data, and the experiment results are shown in Figure 3.21(a), along with the results for location L1. It can be seen from Figure 3.21 that although similar trends can be seen in these TPs, RSS shadowing loss values differ between locations due to multipath effects which are location-dependent.

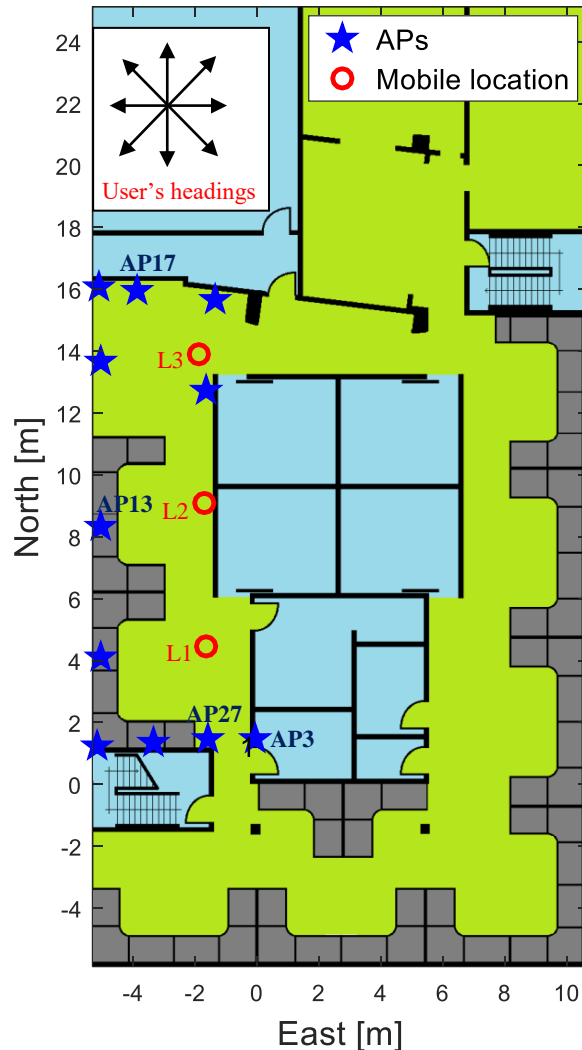


Figure 3.20: APs and mobile deployment in Appropolis office for body shadowing effect experiments

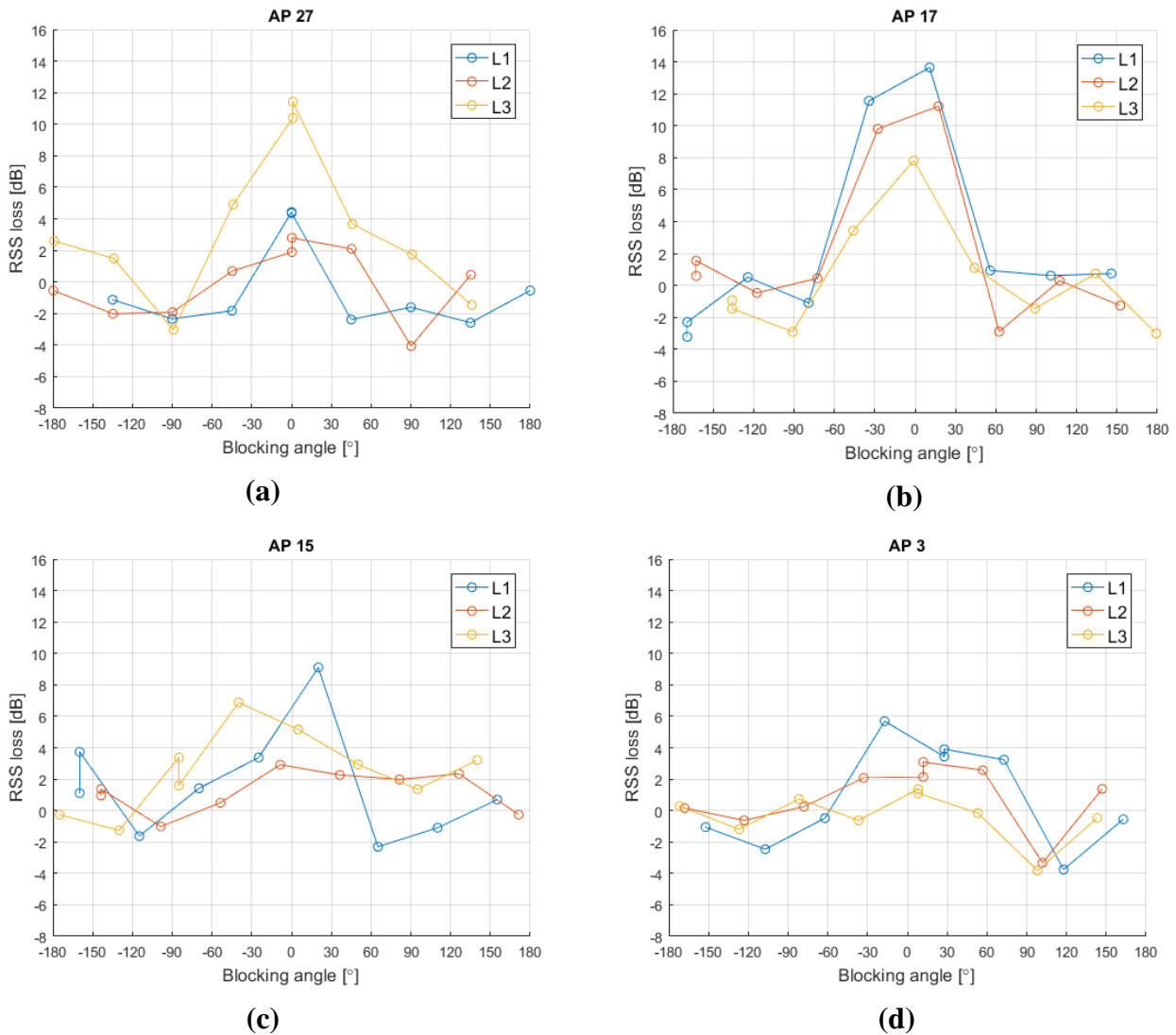


Figure 3.21: Multipath effects on 5 GHz RSS body shadowing loss for different APs

3.3.2.3 Indoor Experiment with Multiple APs

As shown in the previous experiments, the RSS body shadowing loss is affected by multipath signals which are random and can only be characterized in a statistical way. The dependence of RSS shadowing loss on the blocking angle should also be random and needs to be characterized statistically, through additional more experimental data. To do this, 10 more APs were deployed in the Appropolis office and the tablet were placed in L1, L2 and L3 locations for data collection,

which is shown in Figure 3.20. Similar to the previous experiments, for each mobile location, a person standing close to and facing the tablet changed his heading each time for data collection, but in this experiment RSS measurements from multiple APs were collected simultaneously. The eight headings for the data collection are shown in Figure 3.20. Since the locations of APs and tablet are known, for each user's heading, the blocking angle with respect to each AP can be computed.

Figure 3.21 (b) (c) (d) show the interesting results of some APs. The corresponding APs are marked in Figure 3.20. While for AP17, the RSS shadowing loss shows a strong dependence on the blocking angle for the three mobile locations, this is not the case for AP15 and AP3. For AP15 in location L2 and AP3 in L3, this dependence is quite weak. These observations again demonstrate the influence of multipath signals on the RSS shadowing loss. Such multipath influence depends on the locations of both APs and mobiles and is next to impossible to model due to the complexity of multipath. One main objective of this thesis is to use a simple model with a small number of parameters to model the body shadowing effect on RSS. It is now of interest to model the dependence of RSS body shadowing loss on blocking angle without the need to specify the AP and mobile locations. To do this, the RSS shadowing loss results across all APs and mobile locations are shown in the scatter plot in Figure 3.22. Although noisy, the data in the figure still shows the dependence of the RSS shadowing loss on the blocking angle statistically. Several statistical characteristics can be concluded from the data:

1. RSS shadowing loss generally decreases as the absolute value of the blocking angle increases, which is consistent with the previous work reported (Bahl and Padmanabhan, 2000, King et al 2006).

2. However, as the absolute value of the blocking angle becomes greater than a certain value, the RSS shadowing loss seems negligible.
3. The RSS shadowing loss seems symmetrical to the blocking angle.

Based on the data shown in Figure 3.22, an empirical model will be proposed in Chapter 4 to model the RSS body shadowing loss, and these features will be quantified in this model. The utility of the model will be evaluated by the performance of the positioning algorithm making use of this model.

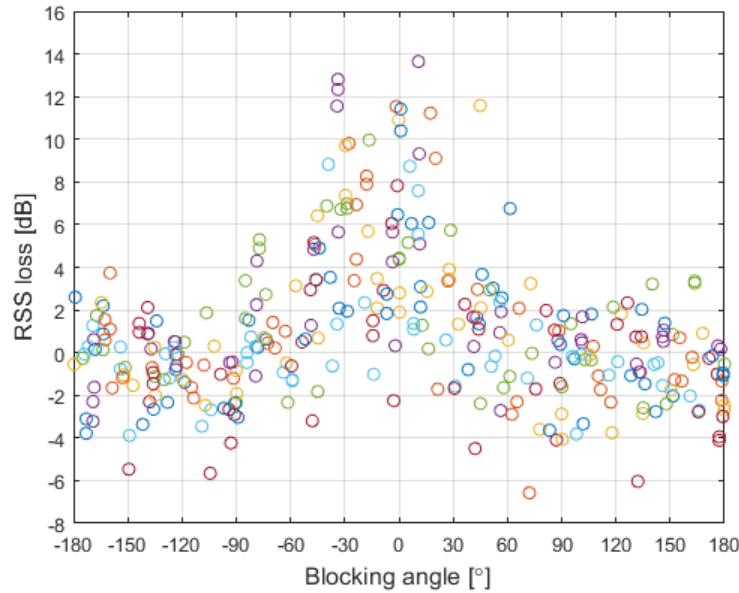


Figure 3.22: 5 GHz RSS body shadowing loss versus blocking angle for 11 APs at 3 mobile locations in Appropolis office

3.4 Conclusion

This chapter successfully characterized RSS pathloss as well as human body shadowing effects on RSS through Wi-Fi 2.4 GHz and 5GHz experimental data in various outdoor and indoor environments.

It was observed overall that the RSS standard deviation of Wi-Fi 2.4 GHz signals is larger than that of the 5 GHz signals in both outdoor and indoor environments. When it comes to indoor environments, the harsh indoor signal propagation increases the RSS variation for signals in both bands. Moreover, considerable outliers are present in the 2.4 GHz signals, which increase its variability. However, this is not the case for the 5GHz RSS measurements. Therefore, it is more advantageous to utilize 5 GHz RSS for positioning, mostly due to the interference in the 2.4 GHz band.

For RSS pathloss, the pathloss exponent parameter is less than 2 indoor LOS hallway environments due to the waveguide effect. The pathloss model was trained for multiple APs specifically in an indoor office environment. The trained pathloss models will be used in the rest of the thesis for the positioning algorithms based on pathloss model.

The human body shadowing effect was characterized to investigate how the blocking distance and blocking angle influence the RSS body shadowing loss. For 2.4 GHz Wi-Fi RSS measurements, it was observed that the body shadowing loss in indoor environment is less significant compared to the uncertainty in RSS caused by other factors such as interference and multipath. Therefore for 2.4 GHz signals, it is difficult to characterize the body shadowing effect and there is a relatively small to negligible loss in information by ignoring the body shadowing. For 5 GHz RSS measurements, it has shown that when a person is close to a mobile or the AP, the RSS shadowing loss becomes significant. Experimental results further associated the RSS shadowing loss with the blocking angle when the mobile is close to the device user's body. However, it was shown that the body shadowing effect is influenced by multipath, and due to the randomness of multipath, the dependence of the RSS shadowing loss on the blocking angle needs to be characterized statistically. Considerable experimental data was then used for the

characterization. Based on this characterization, an empirical RSS body shadowing loss model will be proposed in the following chapter for positioning purpose and its utility will be evaluated through positioning performance metrics.

Chapter Four: Enhancing RSS based Indoor Positioning by Considering Body Shadowing Effects

As discussed in the previous chapters, an RSS positioning system suffers from significant fluctuations in RSS measurements due to factors affecting the electromagnetic coupling between transceiver's antennae; human body shadowing effect is another such factor. To characterize the body shadowing effect on RSS measurements, field data was collected and analyzed in Chapter 3. It has shown that when a person is close to a mobile, the RSS body shadowing loss becomes significant for Wi-Fi 5 GHz signals. One example is the common positioning scenario where a mobile device is held out front of and close to the user's body; in this case, RSS body shadowing loss can be associated with the blocking angle. Based on the RSS characterization made, the main topic of this chapter is to improve RSS modeling by considering the RSS body shadowing loss to enhance the RSS-based indoor positioning. An empirical model with a small number of parameters is proposed to model the dependence of the RSS body shadowing loss on the blocking angle, and experimental training data are used to train the model parameters for the office environment consider in this thesis. By using this model, an estimator is proposed to jointly estimate the user's location and heading. The utility of the RSS body shadowing loss model will be evaluated by performing positioning using the proposed estimator.

4.1 Empirical RSS Body Shadowing Loss Model

Suppose that a user is holding a mobile device in front of himself and attempts to self-locate in an indoor environment. When he is facing an AP, there is a direct propagation path from the AP to his mobile (LOS path), assuming there are no other obstacles blocking the path. As the user moves around and changes heading, the user's body may block the LOS path and thus cause a

theoretically loss in the RSS reading, as shown in Figure 4.1. Generally, the RSS shadowing loss is influenced by the azimuth angle β defined by the user's heading and the T-R line, as well as the elevation angle α between the user and AP, as shown in Figure 4.2(a). This relation can be described in general by

$$\eta = f(\beta, \alpha) \quad (4.1)$$

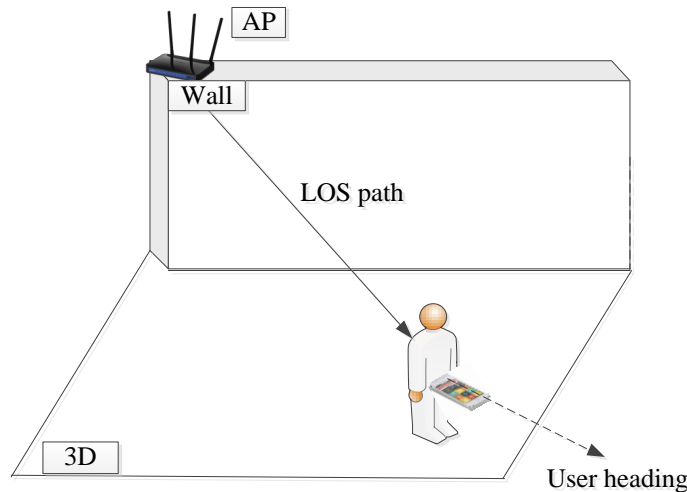


Figure 4.1: Mobile user's body blocks RSS from an AP

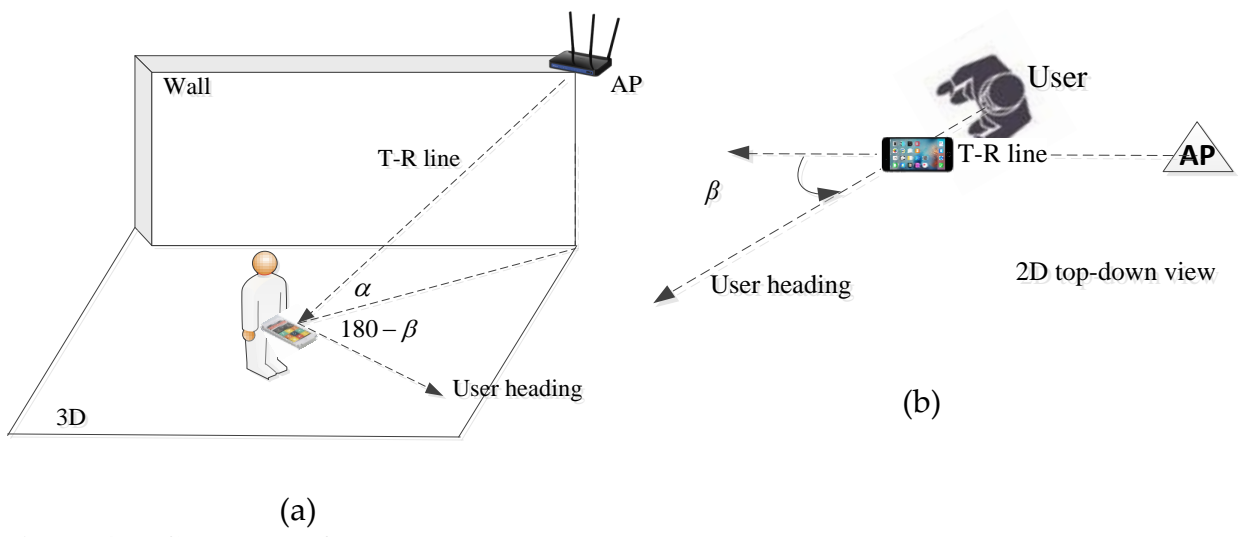


Figure 4.2: Geometry of T-R line, user's heading and blocking angle in (a) 3D scenario (b) 2D scenario

Usually, a mobile device is held close to the user's body, so a near-field blockage scenario can be assumed. Additionally, the probability of a user being close to an AP is much lower than the other way around (especially in large open space and due to the fact that APs are usually installed in ceilings), hence a small α can be assumed most of the time. Under such circumstances, when the user moves around, β will determine the blocking degree (e.g., no blocking, half blocking, complete blocking, etc.) more significantly than α . In other words, the RSS shadowing loss depends strongly on β and weakly on α and then (4.1) can be reduced to

$$\eta = f(\beta, \alpha) \approx f(\beta) \quad (4.2)$$

Accordingly, the body shadowing 3D scenario in Figure 4.2(a) can be simplified to a 2D scenario as shown in Figure 4.2(b). The azimuth angle β shown in Figure 4.2(b) is defined as the blocking angle, and it ranges from -180° to 180° as indicated by in the figure.

The body shadowing effect on RSS reading from a mobile device is a complex phenomenon of physics and modeling from a physics basis would be very difficult if not impossible, and even if such a model could be derived, it may not be practical for positioning use. Instead, this thesis proposes an empirical model based on experimental data. The parameters associated with the model are trained by fitting an empirical curve to the experimental data. Furthermore, the proposed model will be incorporated into an RSS measurement model for positioning. Using this method, the utility of this model will be verified through positioning performance enhancement analysis after implementation.

The RSS body shadowing loss data versus the blocking angle from Chapter 3 is shown in Figure 4.3. The conjectures made based on the data are as follows:

- 1) The RSS body shadowing loss η is symmetrical about the blocking angle β , which indicates that η can be modeled as a function of the absolute value of the blocking angle, $|\beta|$. Note that by doing this, the number of parameters needed for modeling can be reduced and hence a simpler model can be achieved. In Figure 4.4, η are plotted versus $|\beta|$ by blue circles.
- 2) η generally decreases as the $|\beta|$ increases, which is consistent with the previous work reported (Bahl and Padmanabhan, 2000, King et al 2006). The definition of η was given in Chapter 3 and η should theoretically be a positive value. Many functions can model such a relation. However, as an exponential decay function in general shows a good fit to such relation and is quite simple to use, this thesis thus adopts the exponential decay function for modeling this relation.
- 3) As $|\beta|$ becomes greater than a certain value, η seems to become insignificant and is mainly dominated by zero-mean noise. This is because the block begins to disappear as the user turns to face the AP. Therefore, it is reasonable to model the data in a piece-wise way and the objective is to minimize the square error discrepancy between the model and the observed data using a minimum number of parameters. When $|\beta|$ is less than a transition value, say β_0 and $\beta_0 > 0$, the exponential function mentioned above is used to model η ; when $|\beta| > \beta_0$, η is 0.

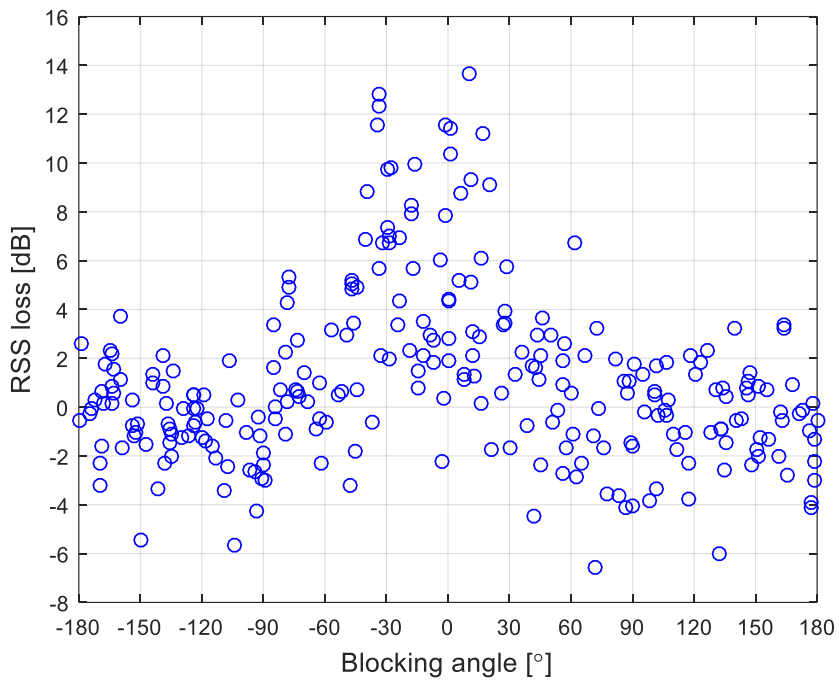


Figure 4.3: 5 GHz RSS shadowing loss data versus blocking angle in Appropolis office

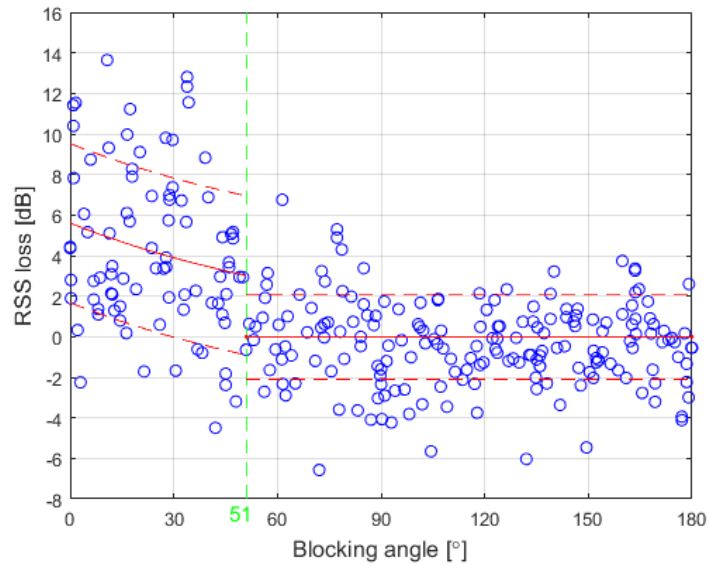


Figure 4.4: RSS shadowing loss model fitted to experimental training data

It can be seen that the RSS shadowing loss data is quite noisy due to factors such multipath; however, to make the RSS shadowing loss model simple to use, the choice is to use a deterministic function to model the dependence of η on β , and the utility of this model will be evaluated by the positioning performance of the algorithm using this model. To summarize, a model is proposed to model the dependence of η on β as follows:

$$\eta(\beta) = \begin{cases} \eta_0 \exp(-a|\beta|) & |\beta| \leq \beta_0 \\ 0 & \beta_0 < |\beta| \leq 180^\circ \end{cases} \quad (4.3)$$

It can be seen that three parameters need to be trained for the model and they are β_0 , η_0 and a . For $|\beta| \leq \beta_0$, η_0 is the RSS shadowing loss when the AP is completely blocked ($\beta = 0^\circ$), and a is a positive number that controls the decay rate of the RSS shadowing loss as β increases.

With the model proposed in(4.3), the model parameters can be trained using the data collected in the Appropolis office in Chapter 3. This can be done by choosing the parameter set (β_0 , η_0 and a) that results in minimum Mean Square Error (MSE) value between the model and the training data, namely

$$[\hat{\beta}_0, \hat{\eta}_0, \hat{a}] = \arg \min_{\beta_0, \eta_0, a} \sum_{\eta_{obs} \in \Omega_t} [\eta(\beta; \beta_0, \eta_0, a) - \eta_{obs}(\beta)]^2 \quad (4.4)$$

In (4.4), $\eta(\beta; \beta_0, \eta_0, a)$ represents the RSS body shadow loss model conditioned on the parameter set $[\beta_0, \eta_0, a]$; $\eta_{obs}(\beta)$ represents an RSS body shadow loss training data that belongs to the training data set Ω_t . The estimated parameters are listed in Table 4.1. The model with the trained parameters is shown in Figure 4.4 by the red solid plot. The standard deviations of the estimation residuals are also shown by red dashes.

Table 4.1: Trained parameters of RSS body shadowing loss model for the test area in Appropolis office

Parameters	value
β_0 [°]	51
η_0 [dB]	5.7
a	-0.01

With the RSS body shadowing loss model, the conventional RSS measurement model only considering pathloss now can be extended to (4.5) by incorporating the body shadowing loss as

$$r = r_0 - \underbrace{10n \log_{10}(d)}_{\text{pathloss}} - \underbrace{\eta(\beta)}_{\text{body shadowing loss}} + w \quad (4.5)$$

Note that w now represents the uncertainty in RSS after modeling the body shadow loss using the proposed model. Due to the simplicity of the proposed empirical model, it may only model the true body shadowing loss partially, and the leftover part becomes an RSS uncertainty component included in w .

To summarize, this section proposes a simple empirical body shadowing loss model based on the experimental data collected in the Appropolis office. Due to the simplicity of the model, it may only partially model true body shadowing loss. But recall that this thesis seeks to model the body shadowing loss in a simple form for practical use. Next, an estimator utilizing this model will be proposed for positioning. The utility of the model will be evaluated indirectly in terms of positioning performance using experimental data.

4.2 Joint Estimation of Position and Heading using Body Shadowing Loss Model

RSS body shadowing loss is a source of uncertainty in RSS measurements if it is not modeled. However, if it is modeled accurately as a function of parameters that are to be jointly estimated

as part of the location computations, then the uncertainty is effectively replaced by a constraint to improve positioning performance. Unfortunately, deriving such an accurate body shadowing model is not practical as discussed previously. Instead, a simple empirical RSS body shadowing loss model was utilized in the last section based on training data. Although there is a residual uncertainty in the proposed model, a partially modelling of body shadowing loss should be able to provide information to enhance positioning performance to some extent. Additionally, because the body shadowing loss is modeled to depend on the blocking angle which can be associated with the user's heading as shown in Figure 4.2(b), the user's location needs to be jointly estimated with the heading which is a useful parameter for navigation. In this regard, a joint estimator is developed herein by using the enhanced RSS measurement model proposed in (4.5) to jointly estimate user's location and heading.

4.2.1 Problem Formulation for Joint Estimation of Position and Heading

Figure 4.5 depicts the scenario for using RSS measurements from multiple APs to jointly estimate user's location and heading. Suppose a mobile user holds the device out front and is located at an unknown position $\mathbf{p} \triangleq (E, N)$ with unknown heading θ . At a certain epoch, the mobile device receives RSS measurements from M APs as denoted by the following RSS vector:

$$\mathbf{r} = [r_1 \quad \cdots \quad r_m \quad \cdots \quad r_M]^T \quad (4.6)$$

The M APs are located at known locations:

$$\mathbf{p}_m \triangleq (x_m, y_m), m = 1, \dots, M \quad (4.7)$$

The problem of joint estimating position and heading is to estimate the state vector

$$\mathbf{x} \triangleq [E, N, \theta]^T \quad (4.8)$$

by using the RSS measurement vector \mathbf{r} .

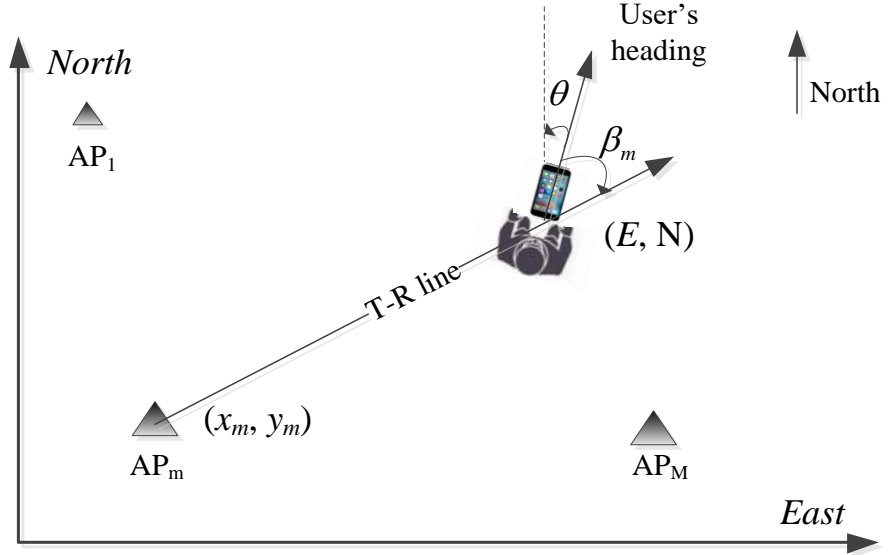


Figure 4.5: Position and heading joint estimation using RSS from multiple APs

With the RSS model taking into account the body shadowing loss proposed in (4.5), the measurement model for the estimation scenario shown in Figure 4.5 can be written as

$$\begin{aligned} r_m &= r_{0_m} - 10n_m \log_{10}(d_m) - \eta_m(\beta_m) + w_m \\ &= k_m(E, N) - \eta_m(E, N, \theta) + w_m, \quad m = 1, 2 \dots M \end{aligned} \quad (4.9)$$

In (4.9), r_{0_m} and n_m is the pathloss parameters for the wireless link between the mobile and m th AP, and d_m is the corresponding T-R distance computed by

$$d_m = \sqrt{(E - x_m)^2 + (N - y_m)^2}, \quad m = 1, 2 \dots M \quad (4.10)$$

In (4.9), it is defined

$$k_m(E, N) = r_{0_m} - 10n_m \log_{10}(E, N) \quad (4.11)$$

$k_m(x, y)$ represents the RSS component considering log-distance pathloss. $\eta_m(\beta_m)$ is the modeled shadowing loss due to the user's body blocking the m th AP. Since the blocking angle β_m is defined as the angle between the T-R line and user's heading through

$$\beta_m = \theta - \tan\left(\frac{E - x_m}{N - y_m}\right) \quad 180^\circ > |\beta_m| \geq 0^\circ \quad (4.12)$$

the shadowing loss is hence denoted by $\eta_m(E, N, \theta)$. w_m is a random variable that represents the noise or uncertainty in the RSS measurement after modeling the RSS by the log-distance pathloss model and proposed body shadowing loss model. The RSS is commonly assumed to be log-normally distributed (Sklar, 1997, Smailagic et al 2000); that is the RSS measurements in dBm are assumed to be Gaussian distributed. Further assume that w_m is Gaussian distributed with zero-mean and variance $\sigma_{w_m}^2$.

With all the above discussion regarding the measurement model, the PDF of the RSS from the m th AP is expressed to be

$$p(r_m | \mathbf{x}) = \frac{1}{\sqrt{2\pi\sigma_{w_m}^2}} \exp\left\{-\frac{[r_m - (k_m(\mathbf{x}) - \eta_m(\mathbf{x}))]^2}{2\sigma_{w_m}^2}\right\} \quad (4.13)$$

The corresponding log-likelihood function therefore is therefore

$$L_{r_m}(\mathbf{x}) = \ln p(r_m | \mathbf{x}) = -\frac{\ln 2\pi\sigma_{w_m}^2}{2} - \frac{[r_m - (k_m(\mathbf{x}) - \eta_m(\mathbf{x}))]^2}{2\sigma_{w_m}^2} \quad (4.14)$$

It is further assumed that $w_m \quad m=1, 2, \dots, M$ associated with each of the component in the RSS vector \mathbf{r} are mutually independent. Thus the joint PDF of the RSS vector is

$$p(\mathbf{r} | \mathbf{x}) = \prod_{m=1}^M p(r_m | \mathbf{x}) \quad (4.15)$$

And hence the log-likelihood of the RSS vector is

$$L_r(\mathbf{x}) = \ln p(\mathbf{r} | \mathbf{x}) = \sum_{m=1}^M L_{r_m}(\mathbf{x}) \quad (4.16)$$

By inserting (4.14) to (2.27), one has

$$\begin{aligned} L_r(\mathbf{x}) &= \sum_{m=1}^M L_{r_m}(\mathbf{x}) = \sum_{m=1}^M \left(-\frac{\ln 2\pi\sigma_{w_m}^2}{2} - \frac{[r_m - (k_m(\mathbf{x}) - \eta_m(\mathbf{x}))]^2}{2\sigma_{w_m}^2} \right) \\ &= -\frac{1}{2} \sum_{m=1}^M \left(\ln 2\pi\sigma_{w_m}^2 + \frac{[r_m - (k_m(\mathbf{x}) - \eta_m(\mathbf{x}))]^2}{\sigma_{w_m}^2} \right) \end{aligned} \quad (4.17)$$

Now the maximum likelihood estimator (MLE) is the value of \mathbf{x} that maximize $L_r(\mathbf{x})$ in (4.17),

namely

$$\begin{aligned} \mathbf{x}_{ML} &= \arg \max_{\mathbf{x}} L_r(\mathbf{x}) \\ &= \arg \max_{\mathbf{x}} \left\{ \sum_{m=1}^M -\frac{1}{2} \left(\ln 2\pi\sigma_{w_m}^2 + \frac{[r_m - (k_m(\mathbf{x}) - \eta_m(\mathbf{x}))]^2}{\sigma_{w_m}^2} \right) \right\} \end{aligned} \quad (4.18)$$

which is equivalent to minimizing the following negative likelihood:

$$\mathbf{x}_{ML} = \arg \min_{\mathbf{x}} \left\{ \sum_{m=1}^M \left(\frac{[r_m - (k_m(\mathbf{x}) - \eta_m(\mathbf{x}))]^2}{\sigma_{w_m}^2} \right) \right\}. \quad (4.19)$$

(4.19) is the estimator to jointly estimate the user's location and heading by incorporating the body shadowing loss model in the measurement model. The derivation of the analytical form for the MLE in (4.19) is not straightforward; however, the focus of the thesis is to evaluate the performance of this MLE instead of its implementation. Therefore, this thesis chooses to perform

grid search to implement the MLE; that is, define a set of discrete grids in the state space and compute the corresponding likelihood for each grid. The state value in the grid that maximizes the likelihood is determined as the state estimate.

Next, this joint estimator is used to evaluate if positioning improvement is possible by modeling the body shadowing loss, as compared to the positioning method without considering the body shadowing effect. The positioning method ignoring body shadowing effect can be simply obtained by eliminating the body shadowing loss term from (4.19) as:

$$\mathbf{x}_{conv} = \arg \min_{\mathbf{x}} \left\{ \sum_{m=1}^M \left(\frac{[r_m - k_m(\mathbf{x})]^2}{\sigma_{w_m}^2} \right) \right\} \quad (4.20)$$

and will be referred to as the conventional positioning estimator in the rest of this chapter. Note that the state vector \mathbf{x} in (4.20) contains only user's position.

Next, experimental data will be used to evaluate the performance of the proposed estimator and indirectly test the performance of the body shadowing loss model.

4.3 Experimental Data Processing and Results

4.3.1 Experimental setup and data collection

To assess the utility of the empirical RSS body shadowing loss model proposed, test data was collected in the test area where the model parameters were trained. As mentioned in Chapter 3, the test area is a part of Appropolis office, and the environment of the test area is shown in Figure 4.6.



Figure 4.6: Experimental environment in Appropolis office

The main pieces of equipment used for test data collection are the same as those that were used for the training data collection in Chapter 3, which includes include 11 Wi-Fi routers from different manufacturers and a Google Nexus tablet. The 11 Wi-Fi APs were deployed in the test area as shown by the blue stars in Figure 4.7, which is also the same as that for data training collection.

In the experiment, the data was collected in a set of static test points (TPs) as shown in Figure 4.7 by the red circles. The utility of the proposed RSS body shadowing loss model will be evaluated at each of these TPs. For each TP, the tablet was placed on a tripod as shown in Figure 4.8. The objective was to isolate the variation of the body shadowing loss and not to combine it with the variation of the tablet due to hand-grip effects on RSS as mentioned in Chapter 3. When collecting RSS measurements for blocking cases, the user stood right beside the tablet as shown in Figure 4.8(b).

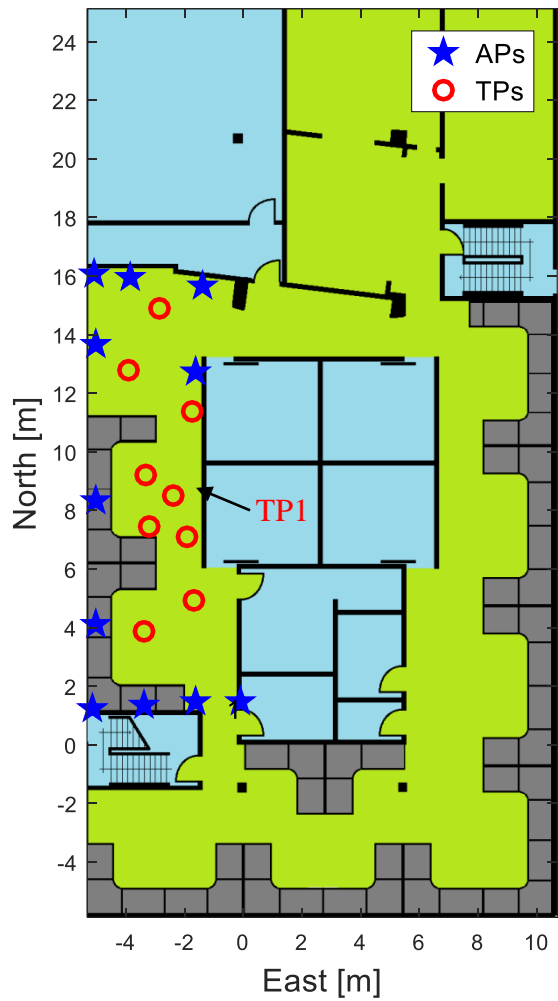


Figure 4.7: Test area floor plan, AP setup and test points



Figure 4.8: (a) RSS collection without body shadowing (b) RSS collection with user pointing south

To obtain the RSS shadowing loss data for analysis, the following three steps were performed to obtain three corresponding RSS datasets:

1. Collect RSS at TPs without body shadowing, as demonstrated in Figure 4.8(a). The RSS mean value computed for each TP using this dataset will be served as RSS reference value that is free of body shadowing effect. In addition, the positioning results computed using this dataset will be compared with those in the shadowing cases for analysis.
2. Collet RSS at TPs with a user pointing south and blocking mobile-AP links. Figure 4.8(b) shows this scenario.
3. Similar to the previous scenario, collect RSS at TPs with the same user pointing north. The two datasets collected at this step and previous step are used to compute the RSS shadowing loss data and to evaluate the positioning performance change due to body shadowing, as well as test the proposed estimator to assess the utility of the proposed RSS body shadowing loss model.

For each AP in each RP of each dataset, the tablet was used to collect data for 5 minutes and about 430 RSS measurements were obtained for data processing.

4.3.2 RSS Body Shadowing Loss Distribution at Test Points

Since the RSS body shadowing loss model was proposed and trained based on the data collected at the training points, it is necessary to evaluate if this model and the trained parameter are able to characterize RSS body shadowing loss for other locations in the same area. To do this, the three collected datasets are used to compute the RSS mean value, which is denoted by

$m_{RSS}(i, j, n)$ $i = 1, \dots, 11$ $j = 1, \dots, 9$ $n = 0, 1, 2$, where i is the index of the APs, j is the index of the TPs and n is the index of the datasets. Then the RSS shadowing loss are computed by

$$\eta(i, j, n) = m_{RSS}(i, j, 0) - m_{RSS}(i, j, n) \quad i = 1, \dots, 11 \quad j = 1, \dots, 9 \quad n = 1, 2 \quad (4.21)$$

The RSS body shadowing loss computed from (4.21) are plotted in Figure 4.9 versus corresponding blocking angles computed using the coordinates of the APs and TPs. The trained RSS body shadowing loss model is also plotted for comparison.

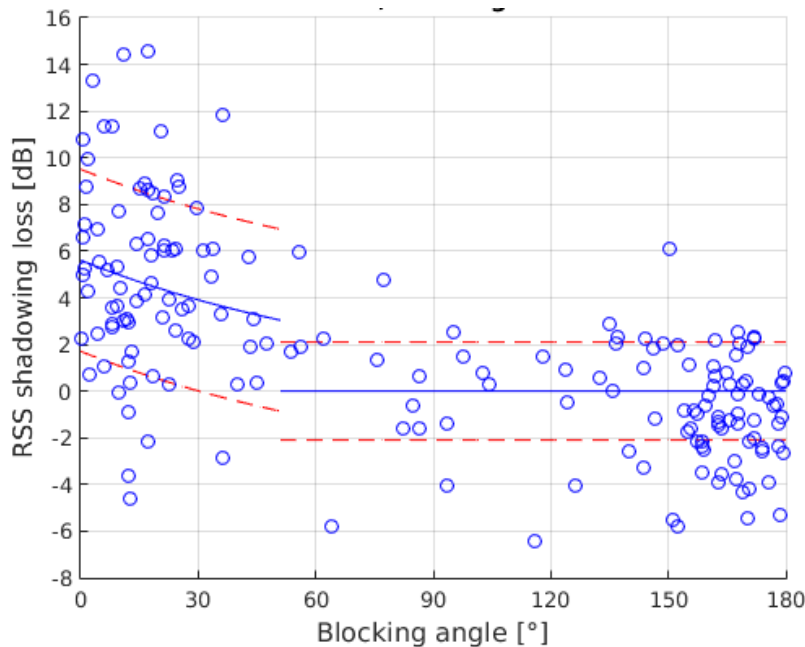


Figure 4.9: RSS body shadowing loss data collected at test points compared to the trained model

4.3.3 Position Performance Evaluation and Comparison

Figure 4.10 shows the data processing scheme for positioning performance evaluation and comparison among different scenarios. There are four test scenarios:

- 1) The first dataset (without shadowing effect) is processed using the conventional positioning algorithm given by (4.20). The positioning performance in this case serves as

reference to which the positioning results for shadowing cases can be compared. But note that positioning without body shadowing does not necessarily produce the best performance since at some locations the multipath likely affects the pathloss modeling and thus positioning performance.

- 2) The second and third datasets (under body shadowing but with different user's heading) are processed using the conventional positioning algorithm. The positioning results in this case are supposed to demonstrate the positioning performance degradation due to body shadowing effect and the body shadowing loss being not modeled.
- 3) The second and third datasets are processed with the proposed estimator to jointly estimate position and heading. The results in this case are used to evaluate the performance of the body shadowing loss model by comparing to the results obtained in the previous two processing cases.
- 4) As will be seen below, the joint estimation of heading with position does not appear to have obvious positioning improvement. Therefore, in the fourth test scenario, the second and third datasets are processed with the proposed estimator with heading constrained to the true value.

To demonstrate the details of processing and results, the following demonstration and analysis first takes a TP as an example, and then evaluates the performance for the overall area.

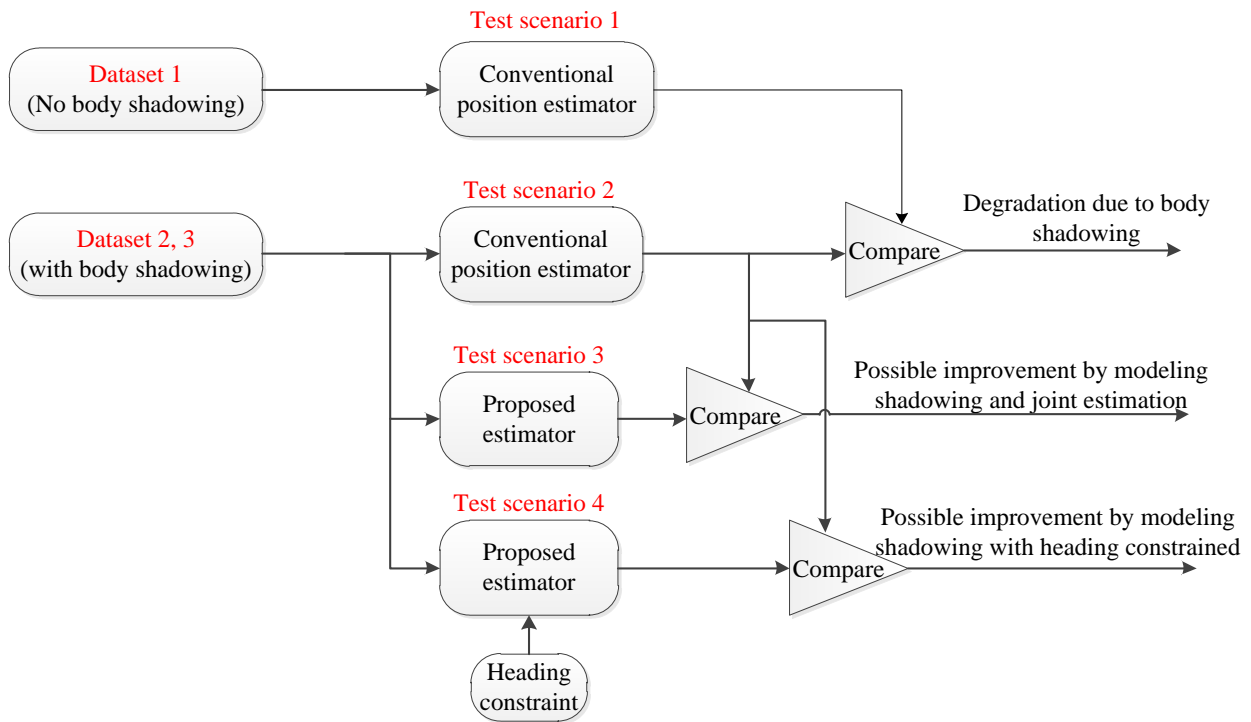


Figure 4.10: Data processing scheme for positioning performance evaluation

4.3.3.1 Results at one test point

The RSS measurements in the first dataset (without shadowing) at location TP1 (shown in Figure 4.7) are first processed using the conventional position estimator and the 2D positioning error percentiles are shown in Figure 4.11 in blue.

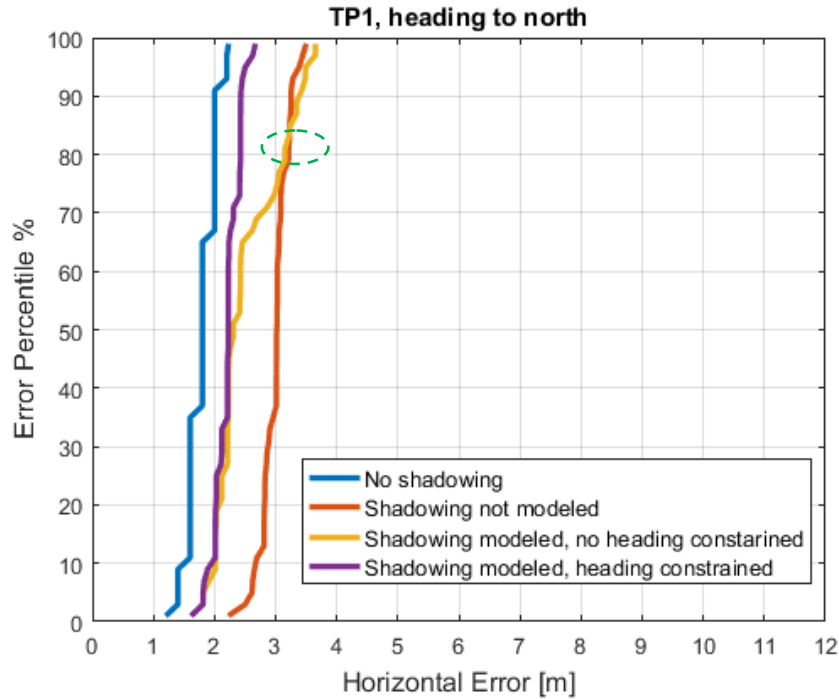


Figure 4.11: Error percentile of positioning errors at TP1, pointing north

Next, the RSS in the second dataset (body shadowing with the user pointing north) collected at TP1 is analyzed. To see the body shadowing loss at this location, the loss values for the 11 APs versus corresponding blocking angles are shown in Figure 4.12. It can be clearly seen that the body shadowing losses with smaller blocking angles are significant. If such losses are not modeled during computations, it will cause ranging errors and hence degrade positioning accuracy. The red plot in Figure 4.11 demonstrates the positioning error percentile in this case where the conventional positioning algorithm is applied without modeling the body shadowing loss. It can be seen that position estimates can be offset by more than 1 m due to the body shadowing effect, as compared to the non-shadowing case. To further reveal how the unmodeled uncertainties in RSS, including the body shadowing loss, can affect positioning, measurement residuals can be analyzed. Denote the measurement residual vector by

$$\mathbf{r}_{res} \triangleq \begin{bmatrix} r_{res_1} & \cdots & r_{res_m} & \cdots & r_{res_M} \end{bmatrix}^T \quad (4.22)$$

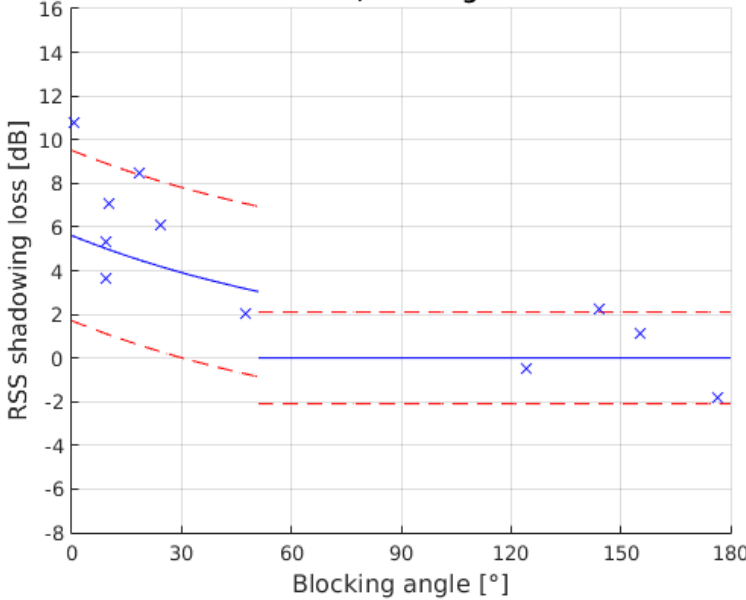


Figure 4.12: RSS body shadowing loss at TP1 with user pointing north

In the context of the RSS measurement model shown in (4.9), the RSS residual vector can be defined as

$$r_{res_m} = r_m - \left[k_m(\hat{x}, \hat{y}) - \eta_m(\hat{x}, \hat{y}, \hat{\theta}) \right], \quad m=1, 2 \dots M \quad (4.23)$$

The residual vector is obtained after the estimates are made, and it can be interpreted as the discrepancy between the actual RSS measurement vector, \mathbf{r} , and the predicted measurement vector $k_m(\hat{x}, \hat{y}) - \eta_m(\hat{x}, \hat{y}, \hat{\theta})$ $m=1, 2 \dots M$. However, it is not straightforward to use a vector to quantify the discrepancy as compared to a scalar. To do so, this thesis chooses to use Sum of Squared residuals (SSR) approaches defined as

$$SSR = \mathbf{r}_{res}^T \mathbf{r}_{res} \quad (4.24)$$

With the SSR, it is now possible to show the discrepancy between the RSS measurements and the measurement model without modeling the body shadowing loss; that is $\eta_m(\hat{x}, \hat{y}, \hat{\theta}) = 0$ in (4.23). Figure 4.13 shows the \sqrt{SSR} for this case, as compared to the \sqrt{SSR} for the non-shadowing case in red. It can be seen that \sqrt{SSR} is much larger than that in non-shadowing case. This is because the RSS measurement model that does not consider the body shadowing loss cannot model the RSS accurately and thus the position estimate is biased, resulting in large residual.

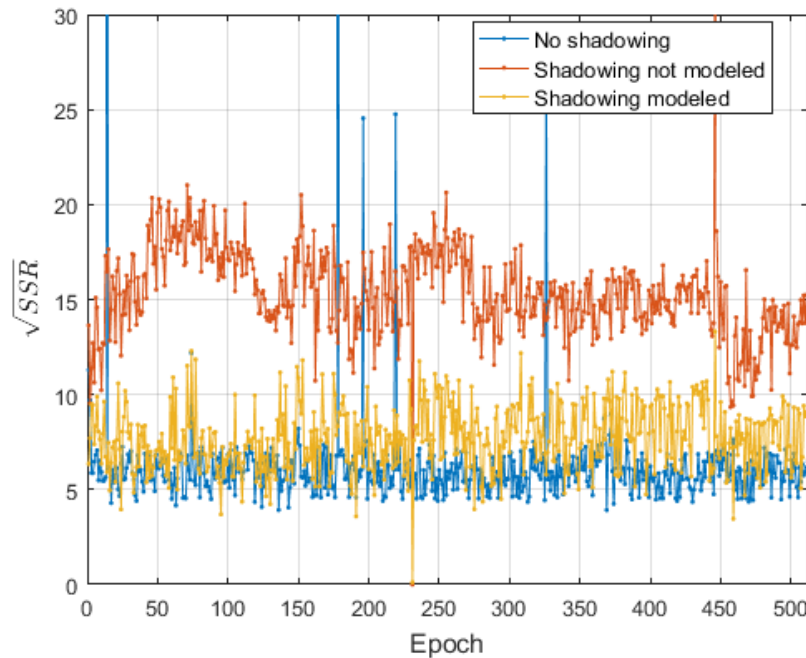


Figure 4.13: Sum of square residuals in different test scenarios at TP1, pointing north

Having examined how body shadowing affects positioning, it is now time to investigate how the proposed body shadowing loss model would assist in mitigating the adverse effect of body

shadowing on positioning. The same data as in a previous processing case (RSS in the second dataset collected at TP1) is processed using the joint estimator proposed in (4.18).

Prior to demonstrating the state estimation results, it is beneficial to analyze the computed measurement likelihood over the state space from which the estimates are determined. For example, for the RSS vector received at a certain epoch, the computed negative log-likelihood over the *E-N* state space conditioned on heading being 0° (pointing north, true state) are shown in Figure 4.14, overlaid on the floor plan.

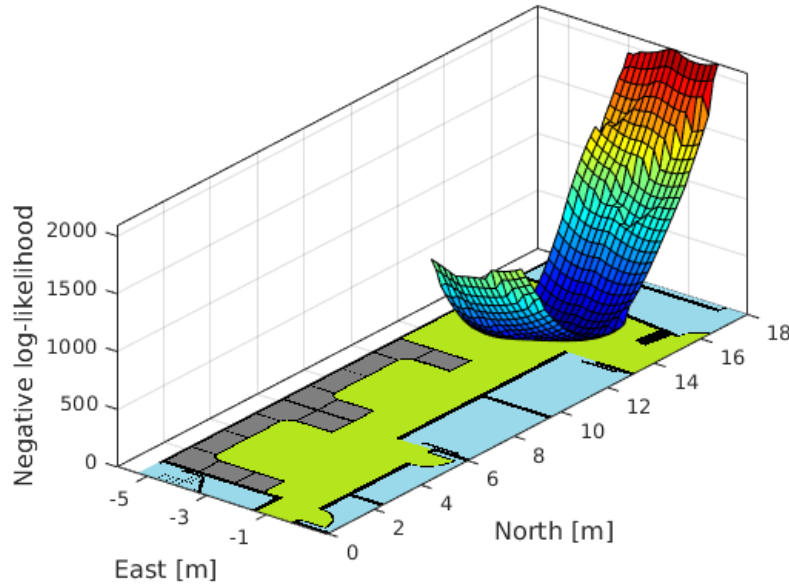


Figure 4.14: Negative Likelihoods over *E-N* state space

Next, analyze the likelihood over the heading state space. Figure 4.15 shows the minimum negative log-likelihood values derived in the *E-N* state space conditioned on different headings in the heading state space. It can be seen that while there is a local minimum area (green ellipse) represented by three consecutive likelihood values which can produce accurate heading estimates, there is also another local minimum area which is ‘narrower’ (red ellipse) and corresponds to the smallest negative log-likelihood value. A ‘wider’ negative log-likelihood local

minimum area is more likely to produce an accurate heading estimate. This is because the body shadowing loss is not very sensitive to the blocking angle, as shown in Figure 4.4, hence it is neither sensitive to the heading. Correspondingly, the likelihood function should not be too sensitive to the heading. Therefore, the fact that the first local minimum area produces an accurate heading estimate is reasonable. However, it is interesting that an erroneous heading can produce a local minimum area (red ellipse) which is the minimum negative log-likelihood value in the overall heading state space. This is due to the inaccuracy in the RSS measurement model, even when the pathloss and body shadowing loss are partially modeled. If the heading estimate is determined directly from such likelihood, an erroneous heading estimate will be produced. The issue shown in Figure 4.15 is not a rare case. Figure 4.16 (a) and (b) display all the heading estimate errors over time and heading error percentiles in blue, respectively. It can be seen that many large significant errors exist in the heading estimates. To improve the heading estimation performance, the fact that an accurate heading estimate corresponds to a ‘wider’ local minimal area can be utilized. To do this, a moving average filter is used to filter the negative log-likelihood in order to eliminate the ‘narrow’ local minimum while retaining the ‘wider’ one. The filtered negative log-likelihood values are shown in red in Figure 4.15 with the length of the averaging filer chosen to be 5. It can be seen that the minimum negative log-likelihood value corresponds to an accurate heading estimate after filtering. Figure 4.16 shows the heading estimates after filtering the likelihood, and then determines the estimate from that; heading estimation has been improved. With the heading estimate, the position estimate can now be determined conditioned on the estimated heading values. The position error percentile is shown in Figure 4.11 in yellow. When compared to the case where the body shadowing loss is not

modeled, positioning performance is improved when the error percentile is less than 75%. However, when the position error percentile is greater than 75%, there is little improvement.

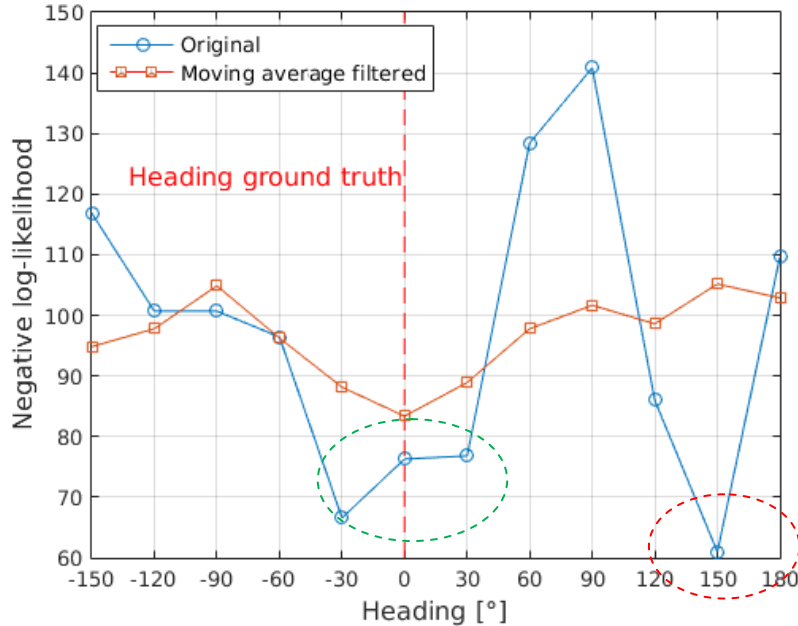


Figure 4.15: Minimum negative log-likelihoods over heading state space

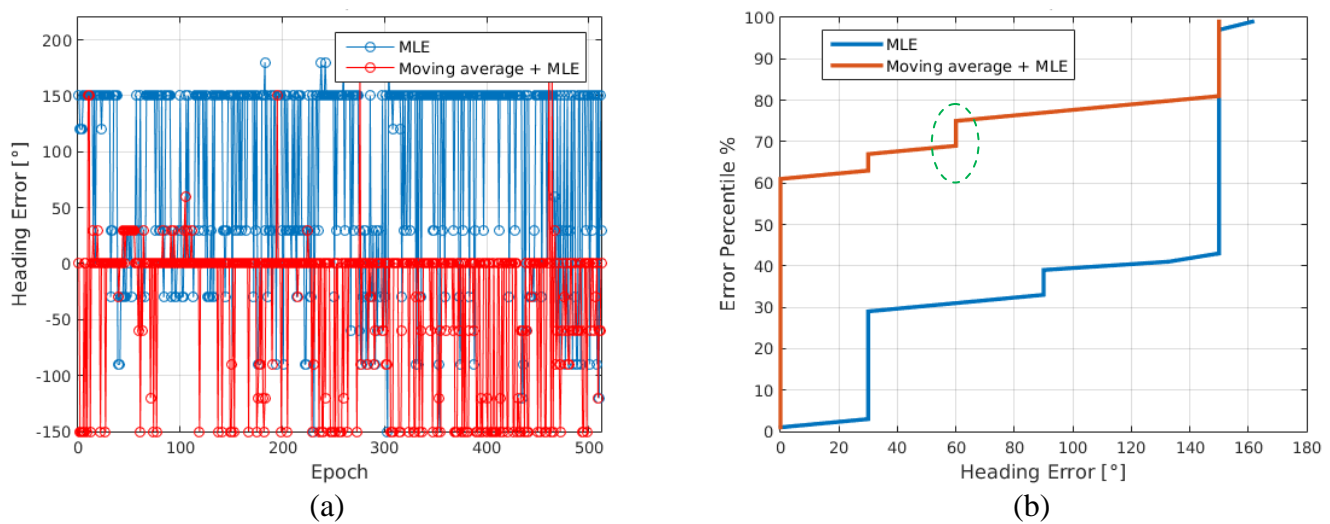


Figure 4.16: Heading estimate errors at TP1 with user pointing north

It is interesting to look carefully at Figure 4.16(b), where the heading error percentile also has a discontinuity at 75% (green ellipse), corresponding to a 60° heading error. This may indicate that, as the heading error reaches 60° , the shadowing loss model becomes invalid. This also suggests that, if the heading can be constrained by prior information (e.g., from other sensors), it could be used to constrain the heading state space search to improve positioning accuracy as well as the computational efficiency. With this in mind, the purple line in Figure 4.11 shows the positioning results when the grid search MLE is constrained to the user's true heading. By comparing the heading-constrained results to the unconstrained results, it is evident that considerable positioning improvement is possible.

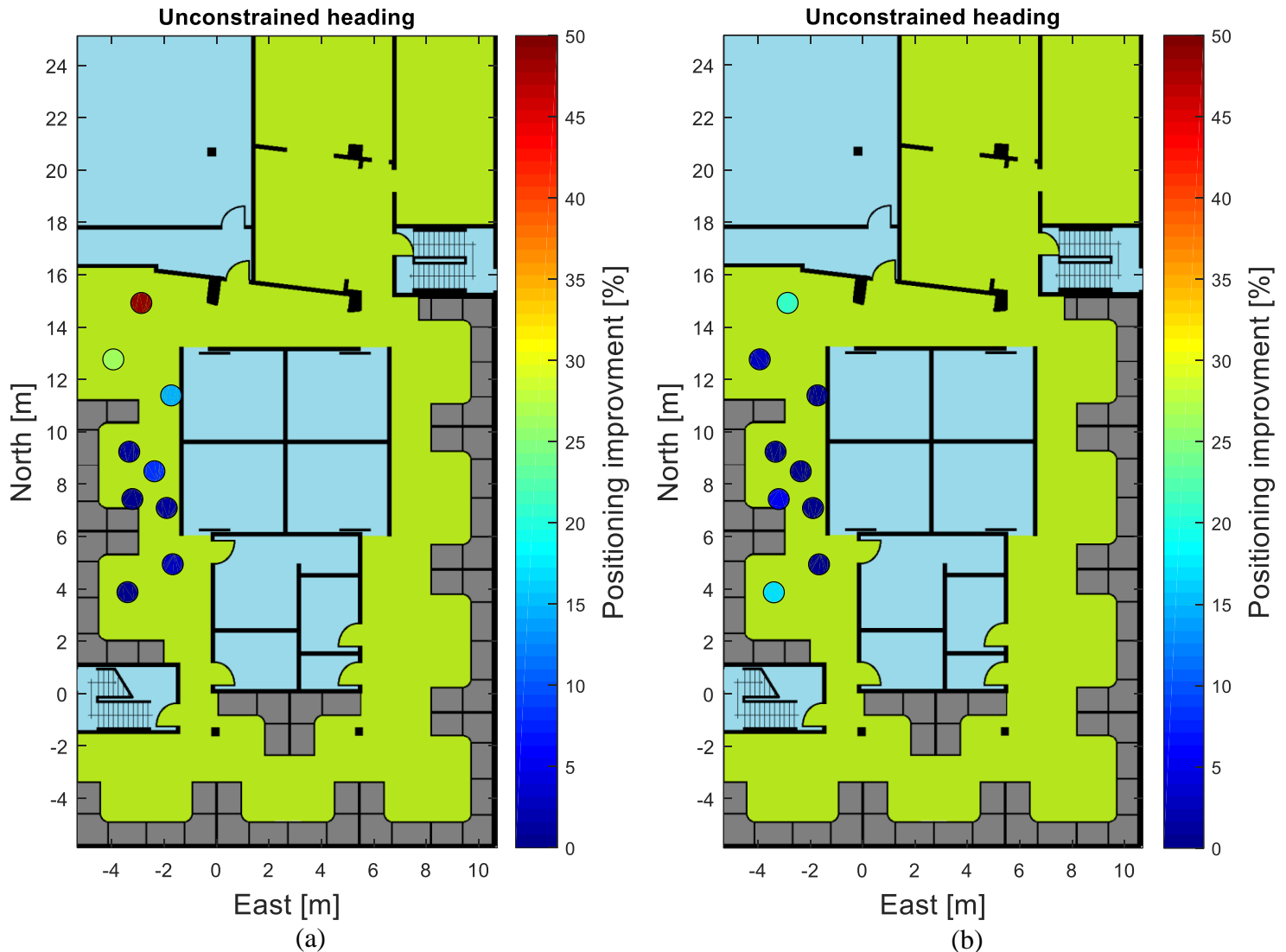
To summarize, the data processing and results at TP1 lead to the following conclusions:

- The effectiveness of using the body shadowing loss model to improve positioning relies on accurate heading estimation.
- If the heading was known in advance accurately, it would improve positioning performance considerably.
- If the heading is unknown and has to be jointly estimated with the position, a modified joint MLE based on (4.19) is needed to handle practical field data processing issue. With the modified MLE, the minimum negative log-likelihood value in the position state space for each possible heading is determined first, and then these values are processed by a moving average filter and searched for the minimum one to determine the heading estimate. Finally, the position estimate is determined as the value that minimizes the negative log-likelihood in the position state space conditioned on that heading estimate.

4.3.3.2 Results at all test points

Having examined the positioning performance at one TP, it is now time to evaluate performance in the overall test area. The four test scenarios are applied to all TPs as shown in the floor plan in Figure 4.7. To access possible performance improvement for multiple TPs, the position Root Mean Square Error (RMSE) at each TP for each test scenario is computed, and the positioning improvement at a TP is evaluated by comparing RMSE at the TP for different test scenarios. Figure 4.17 shows the positioning performance improvement for each TP. Each circle is drawn at the true position of the TP and color-coded according to the improvement computed at that TP. Note that for each TP, the proposed estimator with and without heading constraint is used to enhance positioning by processing the second and third experimental datasets (under body shadowing but with a different user's heading), resulting in four sub-figures in Figure 4.17 to demonstrate improvement. It can be seen that, when the heading is unknown and needs to be jointly estimated, it does not show obvious improvement for the TPs. On the other hand, if the heading is constrained, positioning performances improves in 15 (83%) out of 18 test cases (9 TP, 2 headings). It is interesting to analyze the cases without improvement. For example, for TP2 with user pointing south (shown with a black arrow in Figure 4.17(d)), Figure 4.18 shows the RSS body shadowing loss data collected. Many values deviate considerably from the proposed model, and some are even negative. This indicates that multipath signals dominate the signal propagation, and thus the main source of uncertainty is multipath which is not modeled by the RSS measurement model used (which is a combination of pathloss and body shadowing loss models). It is interesting to further examine the position error percentile for this case in Figure 4.19. It is evident that the position estimates are offset considerably in the no-shadowing case, which further proves that multipath dominates the signal propagation. Note that the point here is

that since multipath is dominant, neither the pathloss alone model nor the pathloss combined with body shadow loss model can model and remove the majority of uncertainties from RSS. The fact that for this particular case the processing without considering the body shadowing loss has better performance is an exception.



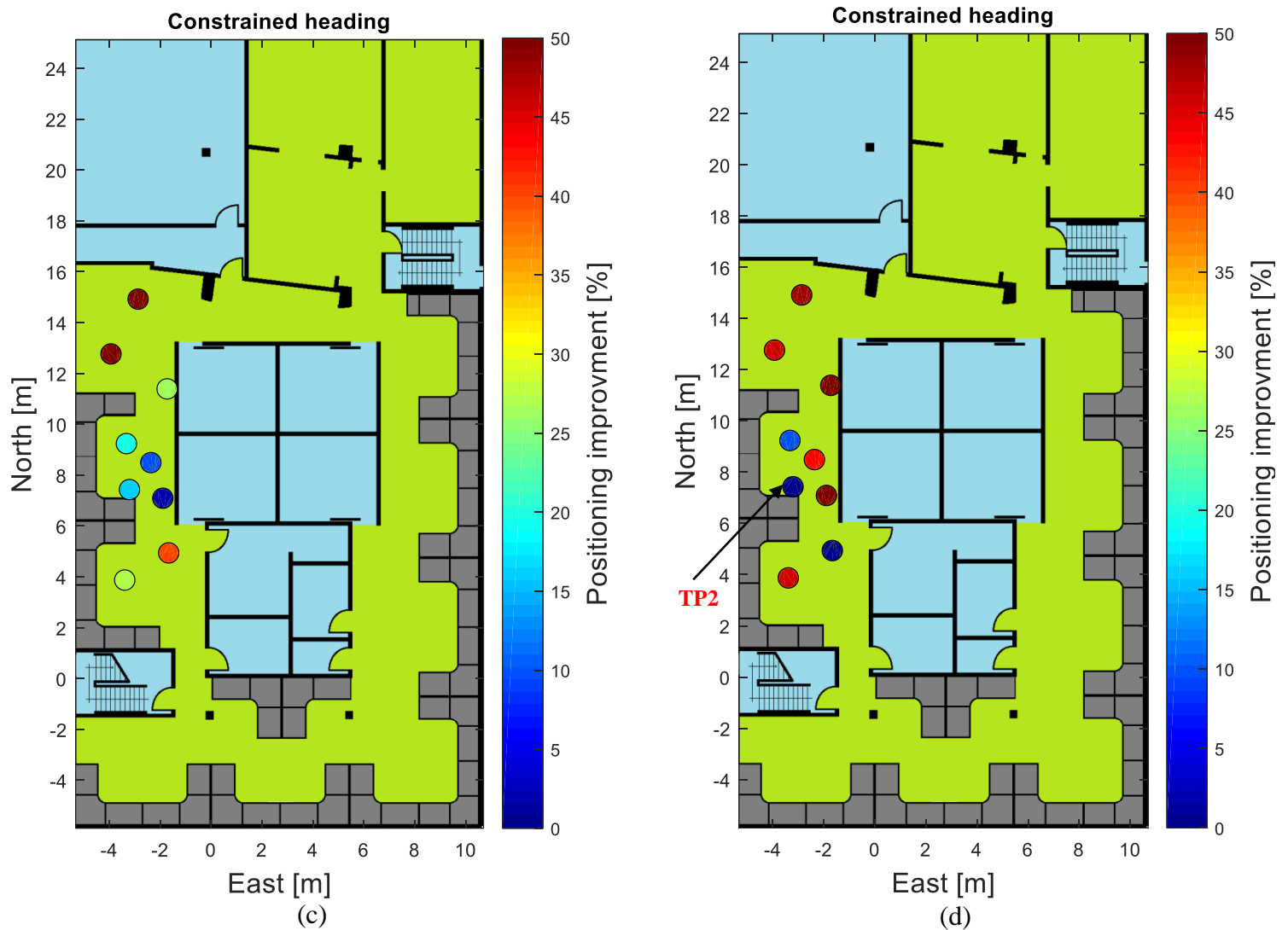


Figure 4.17: Position errors as a function of location (a) pointing north, heading not constrained, (b) pointing south, heading not constrained, (c) pointing north, heading constrained, (d) pointing south, heading constrained

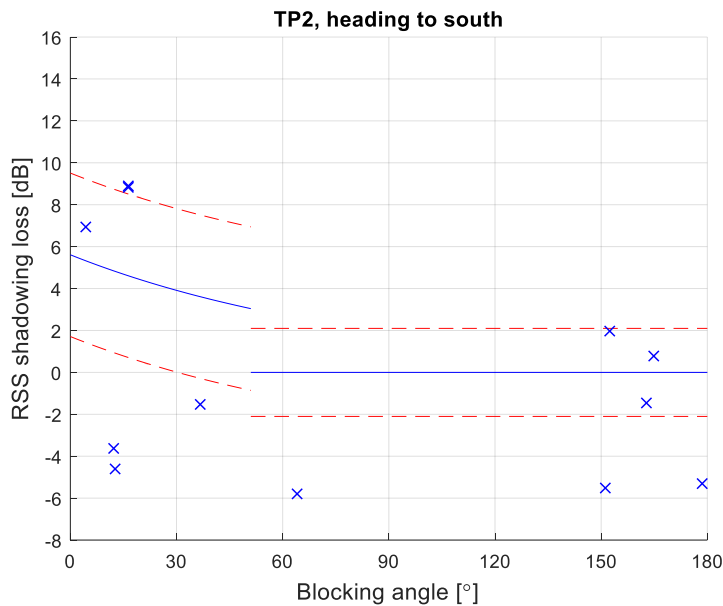


Figure 4.18: RSS body shadowing loss at TP2, pointing south

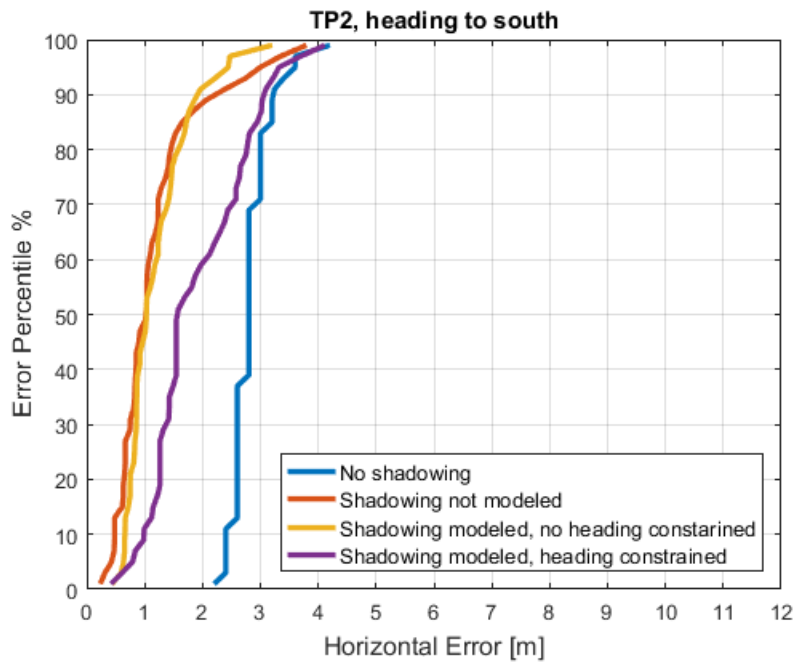


Figure 4.19: Error percentile of positioning errors at TP2, pointing south

To quantify the positioning performance over all TPs, Figure 4.20 shows the position error percentiles over all TPs in the four test scenarios. With the body shadowing loss modeled and using the proposed estimator, even if the heading is unknown and has to be jointly estimated with position, the resulting positioning performance is as good as or slightly better than the conventional estimator. It can be seen that the median position error is reduced by around 0.3 m. Moreover, by using the body shadowing loss model and constraining the heading, considerable improvement can be achieved and the median position error is reduced by about 0.8 m.

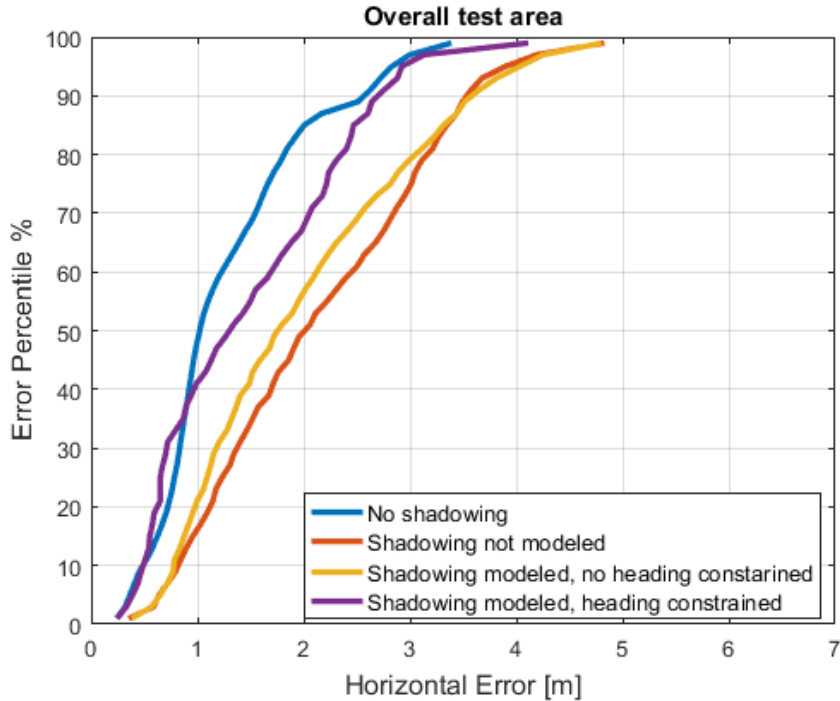


Figure 4.20: Error percentile of positioning errors of all TPs

Table 4.2 Average RMSE positions over all RPs

Test scenarios	RMSE [m]	Position RMSE Improvement [%]
No shadowing	1.5	
Shadowing not modeled	2.4	
Shadowing modeled, heading not constrained	2.2	8%
Shadowing modeled, heading constrained	1.8	25%

4.4 Summary

Based on the RSS body shadowing loss characterization made in Chapter 3, an empirical RSS body shadowing loss model was proposed in this chapter to model the dependence of body shadowing loss on the blocking angle which can be associated with user's heading. By incorporating this model with the conventional RSS measurement model that considers pathloss, a MLE was proposed to jointly estimate user's position and heading. Training data was used to estimate the parameters of the body shadowing loss model and independent test data was used to evaluate the effectiveness of the proposed model through positioning performance. Experimental results have shown that the usefulness of the body shadowing loss model to improve positioning relies on the accuracy of heading estimates and is affected by multipath signals. If the user's heading is unknown and has to be estimated jointly with position, 70% of test cases improve, and the overall positioning performance improves by 8%. If the user's heading is constrained, then 83% of test cases improve and the overall positioning performance improve by 25%.

Chapter Five: Enhancing RSS-based indoor positioning with Security Cameras and Building Maps

As discussed in previous chapters, considerable uncertainties in RSS measurements in the indoors reduce the Fisher information in the RSS measurements for positioning and thus degrade positioning. In general, the Fisher information can be improved by removing uncertainties in measurements and/or adding constraints to the measurement model. Corresponding to the first strategy, one main objective of this thesis is to improve RSS modeling to remove uncertainties in RSS and enhance ultimate positioning performance. Based on the RSS characterizations conducted in Chapter 3, an empirical model was proposed in Chapter 4 to model the uncertainty in RSS measurements due to the human body shadowing effect. It turned out that the proposed model with trained parameters in an indoor environment is able to partially model the body shadowing loss and improve the ultimate position estimation, especially when the heading parameter is constrained; however, due to the complexity of the mechanism of body shadowing, the proposed model can only partially model this uncertainty. Under some circumstances, other dominant error sources are very difficult to model effectively, e.g., fading caused by multipath. In such cases, modeling uncertainty sources to improve positioning is ineffective. The second strategy, namely applying constraints to measurement models, makes use of prior information to improve position estimation. From the Bayesian filtering perspective as introduced in Chapter 2, this is to improve state a posteriori distribution estimation by incorporating state prior distribution from prior information recursively. These prior information sources can be in the form of sensor data, motion dynamics models, building map, etc. This chapter investigates how to use a security camera and obtain information effectively from the Computer Vision (CV) processing results to enhance position estimation. An estimator is proposed to infer user's

heading in corridors by using data from an uncalibrated security camera. A camera-aided RSS positioning system based on Kalman filtering is then proposed to incorporate the heading estimates for enhancing positioning performance. This chapter investigates further incorporating constraints from a building map. A map-camera-aided RSS positioning algorithm based on particle filtering is proposed. Wi-Fi transceivers and a security camera are exploited to set up an experimental environment in an office building for data collection to evaluate the proposed algorithms. The positioning performances of unaided RSS, camera-aided RSS and camera-map-aided RSS solutions are demonstrated and compared.

5.1 Unaided RSS Positioning System based on Kalman Filtering

Prior to investigating of using security camera and building maps to enhance an RSS-based positioning system, it is necessary to introduce the unaided RSS system upon which the enhancing techniques can be developed. Additionally, the positioning results of the RSS-enhancing solutions will be compared to those of the unaided RSS system to analysis the specific improvements. Figure 5.1 shows a commonly used unaided RSS positioning system based on Kalman filtering. Generally, the Kalman filter takes the position observations from the RSS-based trilateration (introduced in Chapter 2) and produces filtered position estimates making use of the observation model and a system state model.

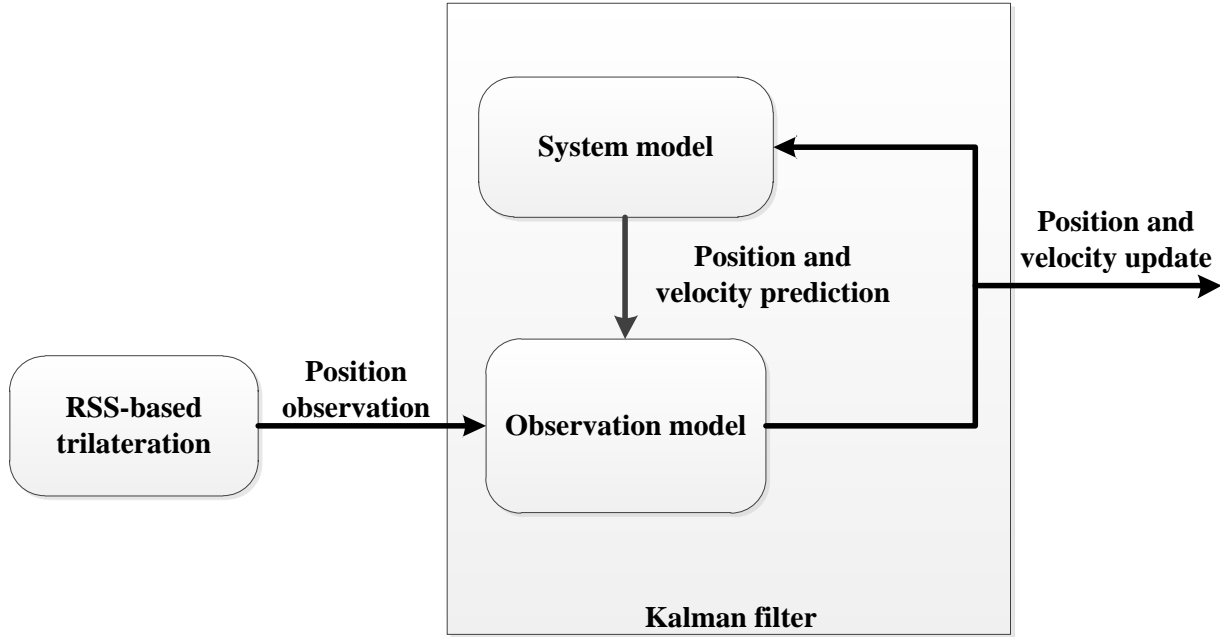


Figure 5.1: Unaided RSS positioning system

Specifically, the system state vector is

$$\mathbf{x} = [E \ N \ v_E \ v_N]^T \quad (5.1)$$

where E and N are the 2D coordinates in the local coordinate system, and v_E and v_N are the velocities in the east and north directions. The system state model of the pedestrian's position uses a classical Pedestrian Dead Reckoning (PDR) model (He et al 2013):

$$\begin{aligned} \dot{E} &= v_E \\ \dot{N} &= v_N \end{aligned} \quad (5.2)$$

where $\dot{\bullet}$ represents derivative. The velocities are further modeled as random walk processes:

$$\begin{aligned} \dot{v}_E &= \eta_{v_E} \\ \dot{v}_N &= \eta_{v_N} \end{aligned} \quad (5.3)$$

where η_{v_E} and η_{v_N} are the white Gaussian noise of the corresponding state (Shin, 2006, Evennou and Marx, 2006, Khan and Syrjarinne, 2013, He et al 2014). Note that the random walk assumption in (5.3) states that each velocity component propagates with an acceleration governed by a white Gaussian random process. The use of this Gaussian white noise model herein assumes the least amount of information regarding the user's motion.

The observation is the position estimates from RSS-based trilateration is denoted by

$$\mathbf{z} = [E_{obs} \quad N_{obs}]^T \quad (5.4)$$

Thus, the observation model is

$$\begin{aligned} E &= E_{obs} + w_E \\ N &= N_{obs} + w_N \end{aligned} \quad (5.5)$$

By combining the state vector in (5.1), the observation vector in (5.4) and the observation model (5.5) into a matrix form, the observation matrix \mathbf{H} is

$$\mathbf{H} = \begin{bmatrix} 1 & 0 & 0 & 0 \\ 0 & 1 & 0 & 0 \end{bmatrix} \quad (5.6)$$

which maps the state vector to the observation vector as introduced in Chapter 2.

5.2 Fusing Security Cameras into RSS-based Indoor Positioning System

Some approaches have been proposed using fusion of camera data with wireless signal to perform positioning (Perš et al 2011, Van den Berghe et al 2011, Papaioannou et al 2014). In general, fusion approaches fall into three categories: camera-aided radio, radio-aided camera and radio/camera integration. A review of these methods can be found in Chapter 1. A common point in these approaches is that the object detection results in image pixel coordinates must be mapped to suitable coordinates (e.g., local level frame). To this end, an effective CV system

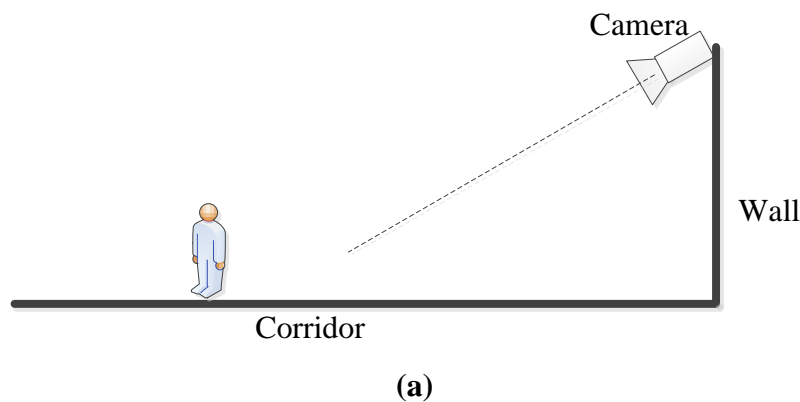
needs careful calibration to obtain accurate camera intrinsic and extrinsic parameters, as described in Chapter 2. Even if a CV positioning system is well-calibrated, it can reach sub-metre accuracy only under certain conditions (e.g., no occlusion, good lighting, objects in moderate distance from cameras, etc.). Hence, the positioning performance of the CV system may degrade significantly due to dim light, occlusion, etc. Also, as compared to the coverage of wireless signals, the Field of View (FOV) of cameras is relatively limited. For example, there are blind spots for FOV and some areas are not suitable for security cameras due to privacy concern. On the contrary, wireless signals are almost ubiquitous indoors. Another inherent limitation of using security cameras for positioning is the problem of ambiguous user's identity; that is, an unaided CV tracking system lacks the ability to associate the tracking results with the corresponding target. This is not a problem for RSS-based positioning systems since RSS measurements are inherently associated with the device identity, e.g., BSSID in a Wi-Fi network as discussed in Chapter 2. To summarize, it is beneficial to investigate how to use a security camera and to obtain information effectively from CV processing to enhance RSS-based positioning.

Now look at the problems from an RSS-based positioning system perspective. As introduced previously, the unaided RSS system utilizes a PDR system model in the Kalman filter. In this case, the dominant error source is typically the heading error (He et al 2013). The heading in the unaided RSS system is actually derived from the change of the position state. However, due to the considerable uncertainty in RSS measurements, the position estimate suffers from large errors and thus heading suffers as well. By incorporating heading observations, the heading state of a PDR algorithm can be updated accurately and the positioning performance can be improved. It has been observed that a corridor is a place where indoor positioning is needed frequently, and

security cameras are usually installed at their ends and are oriented to look in the corridors. In this section, an estimator is proposed to estimate the user's heading by using the object detection results from CV processing; a camera-aided RSS positioning system based on Kalman filtering is proposed to incorporate the heading observations for positioning enhancement, and the performance improvement is evaluated by using experimental data.

5.2.1 Heading Estimation with a Security Camera in Corridors

To extract information effectively from a security camera installed in a corridor, it is necessary to first consider the setup of such a camera, as depicted in Figure 5.2. The security camera is installed at the end of the corridor and is oriented to look down in it as shown by the 2D plot in Figure 5.2 (a); the projection of the v axis of the image plane on the floor is parallel to the corridor as shown in Figure 5.2 (b). The details the coordinates system related to CV processing can be found in Chapter 2. With the camera setup, Figure 5.3 (a) depicts a person walking in the corridor captured by the camera in the image pixel coordinates, and Figure 5.3 (b) depicts the object detection results with the blob representing the walking person. The object detection can be done using the background subtraction algorithm as introduced in Chapter 2.



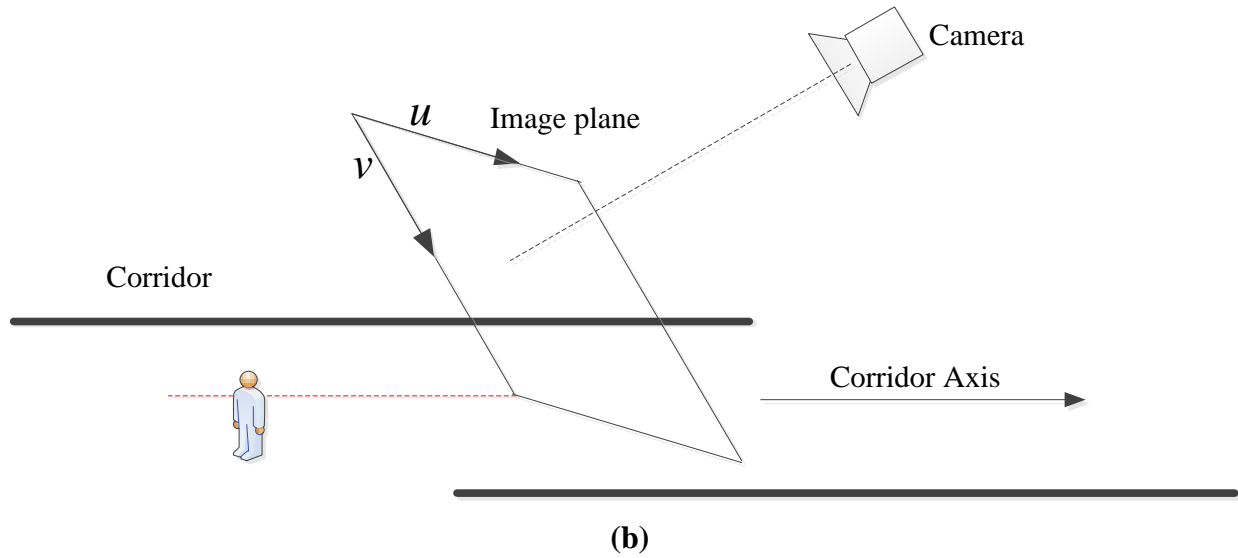


Figure 5.2: Security camera setup in a corridor (a) 2D depiction (b) 3D depiction

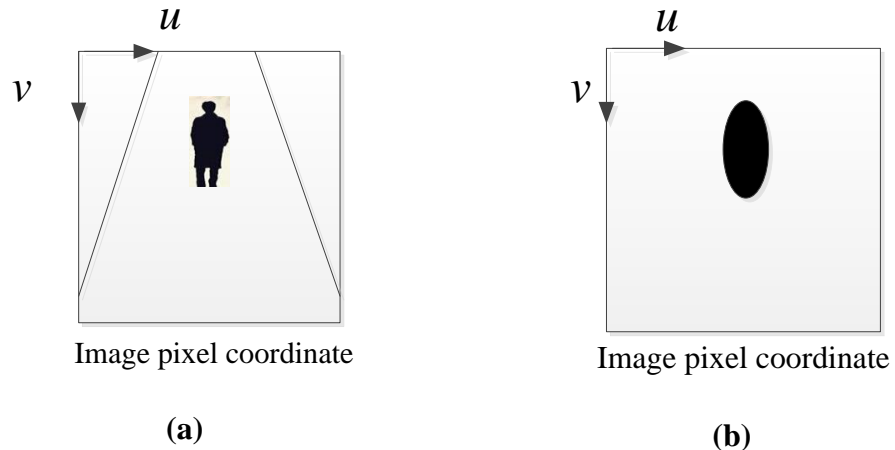


Figure 5.3: (a) A person captured by camera (b) Object detection result

In Chapter 2, it was explained that a static camera positioning system needs to map the object detection results (e.g., results shown in Figure 5.3(b)) to the local level frame, in which calibration is needed to obtain the intrinsic and extrinsic parameters. Instead, this thesis seeks to obtain effective information from the CV processing stage to enhance the RSS-based positions.

The question arises as to whether it is feasible to extract information directly from the object detection results to enhance RSS positioning, without calibrating the security camera.

Assume a mobile user walking in the corridor only backward or forward, hence the walking direction is constrained to be parallel to the corridor. As mentioned above, the projection of the v axis of the image plane on the floor is parallel to the corridor. The change of the detected object along the v axis of the image plane can be exploited to infer the walking direction. To further relate the user's walking direction in the corridor to its heading in the local coordinate system, define the corridor axis as shown in Figure 5.2(b) and denote the angle from the corridor axis to the north axis as γ . Based on this, the change of the detected object in pixel along the v axis of the image plane can be used to estimate the user's heading as

$$\theta = \begin{cases} \gamma & \frac{dv}{dt} > 0 \\ 180^\circ - \gamma & \frac{dv}{dt} < 0 \end{cases} \quad (5.7)$$

where dv/dt is the pixel change rate of the detected object in the v axis. For simplicity, denote

$$k = dv / dt \quad (5.8)$$

hereafter in the thesis.

In practice, k needs to be estimated from a time series of an object's Ground Touching Point (GTP). A GTP refers to the pixel location in the image pixel plane representing the position where the object touches the ground surface; Figure 5.4 provides such an example. In practice, GTPs are noisy and sometimes are missing due to impairments in CV processing such as floor shadows, occlusions due to half-walls or furniture that obstructs the lower part of a person, dim light, object color being similar to the background, etc. An example of noisy GTPs from the CV processing module will be shown based on experimental data in Section 5.2.3.2 when discussing

field data processing. The focus of this thesis is not to improve CV processing algorithm to obtain better GTP estimates; instead, the objective is to infer user's heading more effectively from the noisy GTPs to enhance RSS-based positioning. It has been observed that, the frame rate of security cameras is normally high relative to the motion of a pedestrian indoors; the camera used herein has a rate of 25 frame/s. Further assume that the CV can maintain detection of the pedestrian. k can then be assumed to be constant during a time interval that is sufficiently small. Based on this, k can be estimated by fitting multiple consecutive GTPs to a linear model. In particular, a time window is chosen and L GTPs in the window together with the corresponding timestamps are fitted to a linear model. Then the measurement model to estimate k using GPT measurements can be expressed as

$$\mathbf{v} = [\mathbf{t} \quad \mathbf{1}] \begin{bmatrix} k \\ b \end{bmatrix} + \mathbf{w} \quad (5.9)$$

In (5.9), \mathbf{v} is a $L \times 1$ vector of L GTPs projected on the v axis, the vector \mathbf{t} represents the corresponding timestamps, $\mathbf{1}$ is a $L \times 1$ vector with all component being 1, b is the intercept point of the linear model which is a nuisance parameter and \mathbf{w} is a $L \times 1$ vector represents the noise or uncertainty associated with the measurement vector. Assume that the measurements, \mathbf{v} , generated by CV processing are mutually independent. Additionally, as mentioned earlier, the measurement rate from CV processing is high relative to the pedestrian motion, hence it is practical to obtain large amount of measurements to estimate k in a given time interval. Then a Maximum likelihood Estimator (MLE) is asymptotically unbiased, achieves CRLB, and has a Gaussian PDF (Kay, 1993). Also under these assumptions, a Least Squares (LS) estimator is equivalent to the MLE and also asymptotically achieves CRLB. The LS estimator is expressed by

$$\begin{bmatrix} \hat{k} \\ \hat{b} \end{bmatrix} = \left([\mathbf{t} \quad \mathbf{1}]^T [\mathbf{t} \quad \mathbf{1}] \right)^{-1} [\mathbf{t} \quad \mathbf{1}]^T \mathbf{v} \quad (5.10)$$

which is the estimator of k . Combining (5.10) with (5.7) and (5.8) results in the estimator to obtain user's heading in corridors with CV processing generated measurements.

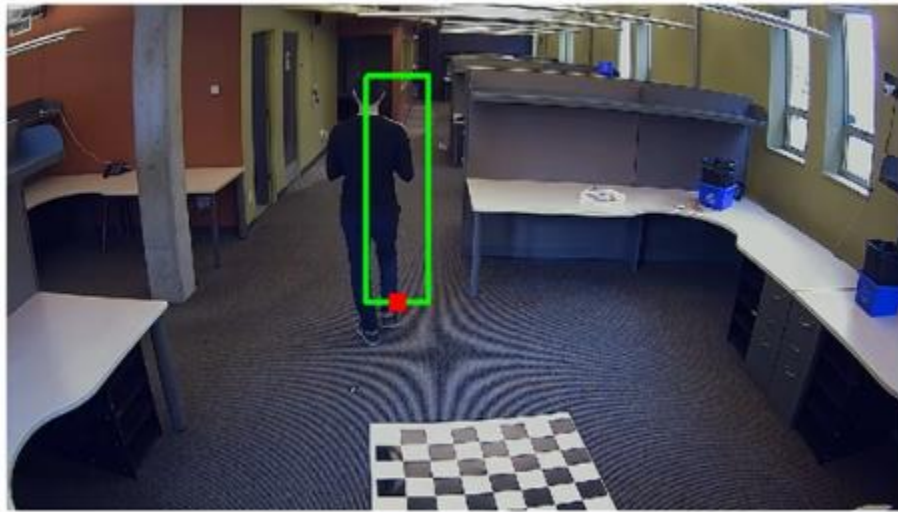


Figure 5.4: Bounding box (green) and ground touch point (red) of a detected object

Some aspects must be considered when applying this estimator in practice. Firstly, the estimator proposed herein relies on the pixel change rate in the image plane to infer heading. In other words, k carries no information regarding heading when it is too small (e.g., the user is static), and the heading estimates using (5.7) become invalid. In practice, the value of k should indicate the validity of the heading estimates. A threshold for k must retain the estimates that carry more information regarding heading. This threshold needs to eliminate the erroneous estimate when k is small. Experimental data will be used to analyze the threshold effect on heading estimation. Second, although the proposed linear measurement model in (5.9) is based on the assumption that the user's velocity is constant during the processing interval and that object detection can always be maintained, this is not always the case in practice. During a processing interval, the

user's velocity might change abruptly (e.g., sharp turn) or a large number of object detection results may be biased considerably due to impairments in the CV processing for object detection (as will be shown with experimental data in Section 5.2.3.2). In this case, the linear model proposed above is not able to fit to the GPTs and a quantity is needed to indicate the high unreliability of the heading estimates. Similar to Chapter 4, the Sum of Squared Residuals (SSR) can be used to quantify the discrepancy between the actual measurement vector and the predicted one, and thus indicate the reliability of the estimate. Denote the residual vector as

$$\mathbf{v}_{res} = [\mathbf{t} \quad \mathbf{1}] \begin{bmatrix} \hat{k} \\ \hat{b} \end{bmatrix} - \mathbf{v} \quad (5.11)$$

Furthermore, the fact that the CV processing is not able to maintain detection the object all the time in practice must be considered, which means that the number of measurements to estimate k may vary. Thus, it is reasonable to use a normalized SSR to indicate the reliability of the heading estimates, namely

$$\frac{SSR}{L} = \frac{\mathbf{v}_{res}^T \mathbf{v}_{res}}{L} \quad (5.12)$$

Experimental data will be used to evaluate the effectiveness of this metric to indicate the reliability of the heading estimate and its utility to improve positioning performance.

5.2.2 Camera-aided RSS Positioning System based on Kalman Filtering

With the heading estimator making use of the CV results discussed in last section, it is now time to consider fusing the heading estimates into an RSS-based system. Figure 5.5 proposes a camera-aided RSS system by extending the conventional unaided RSS positioning system as discussed previously. Compared to the unaided RSS system shown in Figure 5.1, heading

observations using camera data are incorporated into the system. In general, the heading estimator, as proposed in (5.7) and (5.10), processes the CV object detection results to produce heading observation for the following Kalman filter. The Kalman filter utilizes both the heading and position observations from RSS trilateration to track position, horizontal speed and heading of the mobile user.

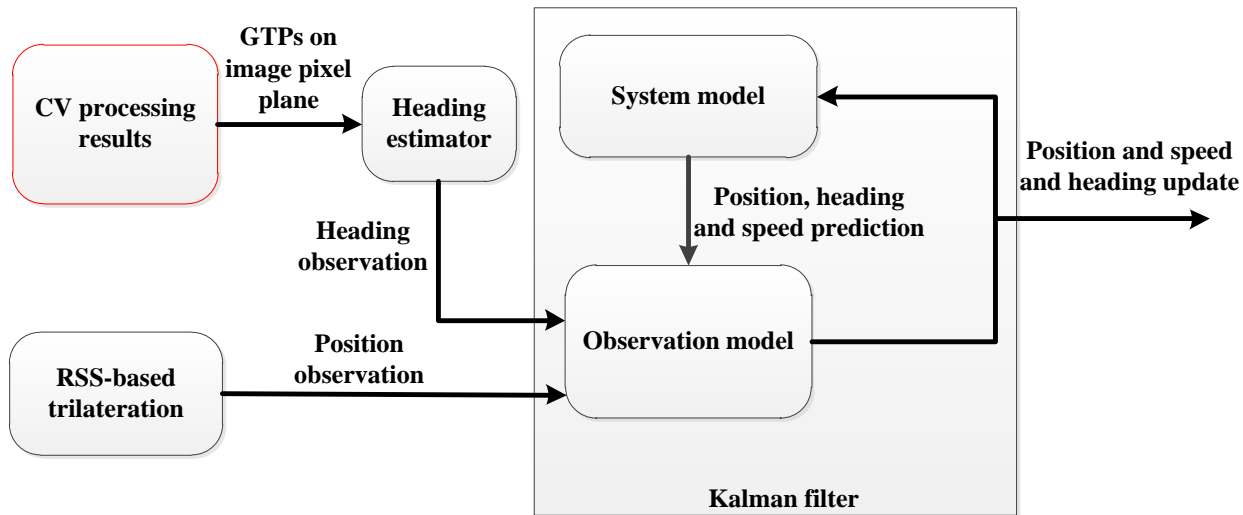


Figure 5.5: Camera-aided RSS positioning system

In particular, the system state vector in this case is

$$\mathbf{x} = [E \ N \ v_h \ \theta]^T \quad (5.13)$$

where (E, N) represents the position in local coordinates, v_h is the horizontal speed and θ the user's heading. Similar to the unaided RSS system, the system state model of the pedestrian's position is

$$\begin{aligned} \dot{E} &= v_h \sin \theta \\ \dot{N} &= v_h \cos \theta \end{aligned} \quad (5.14)$$

and the horizontal speed and heading are modelled as random walk processes:

$$\begin{aligned}\dot{v}_h &= \eta_{v_h} \\ \dot{\theta} &= \eta_\theta\end{aligned}\tag{5.15}$$

where η_{v_h} and η_θ are the white Gaussian noise of the corresponding states. Similar to the unaided RSS system, the use of the white Gaussian noise model here to model the horizontal acceleration and heading change rate assumes the least amount of user motion information. The observations as shown in Figure 5.5 are the position estimates from the RSS trilateration and heading estimates from CV processing denoted by

$$\mathbf{z} = [E_{obs} \quad N_{obs} \quad \theta_{obs}]^T\tag{5.16}$$

Thus the observation model is

$$\begin{aligned}E &= E_{obs} + w_E \\ N &= N_{obs} + w_N \\ \theta &= \theta + w_\theta\end{aligned}\tag{5.17}$$

By combining the state vector in (5.13), the observation vector in (5.16) and the observation model (5.17) into a matrix form, the observation matrix \mathbf{H} is

$$\mathbf{H} = \begin{bmatrix} 1 & 0 & 0 & 0 \\ 0 & 1 & 0 & 0 \\ 0 & 0 & 0 & 1 \end{bmatrix}.\tag{5.18}$$

A simulation was conducted to demonstrate how the heading observation enhances positioning using the proposed algorithm. In the simulation, it was assumed that a user is walking in a straight line forward and backward with a speed of 1.5 m/s for 10 minutes and the reference trajectory in local coordinates is shown in Figure 5.6. The reference heading for the first 100 s is shown in Figure 5.7. To simulate the noisy position observations from RSS-trilateration and heading observations from CV processing, the noise values associated with the position and

heading observations are assumed to be Gaussian distributed with zero mean and standard deviations of 3 m and 10° for position and heading observation, respectively. Note that the statistics of the observations assumed in the simulation may not reflect the statistics of the field data accurately, but the point here is to generate observations to analyze how the heading observation helps enhancing position using the proposed algorithm. Experimental data will be collected and used to evaluate performance in the next section.

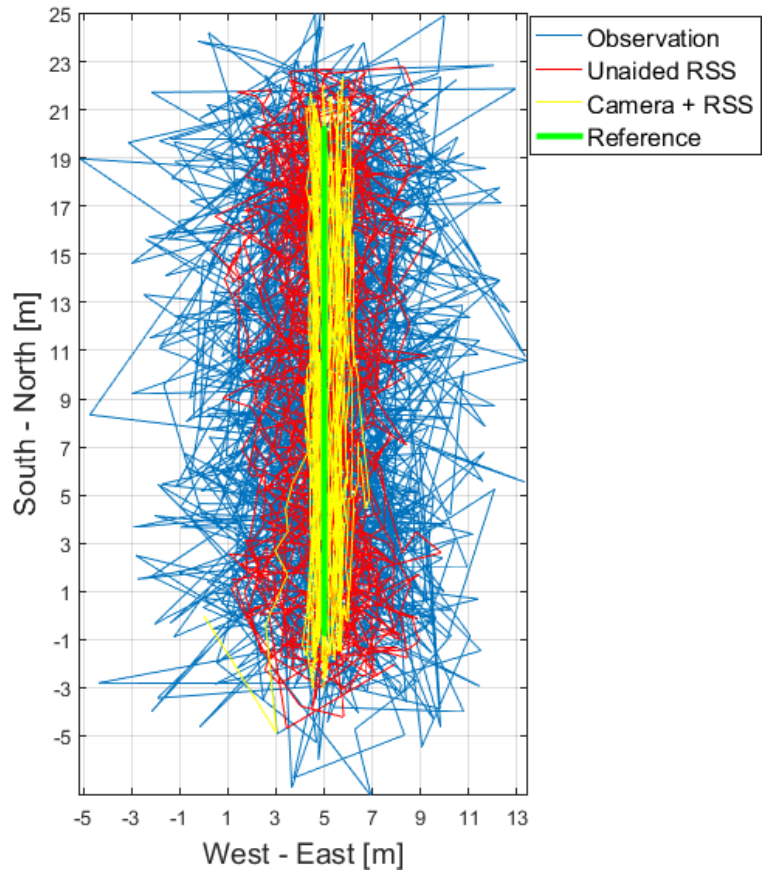


Figure 5.6: Reference trajectory, position observations, unaided RSS Kalman filtering position estimates and camera-aided RSS Kalman filtering position estimates in local coordinates

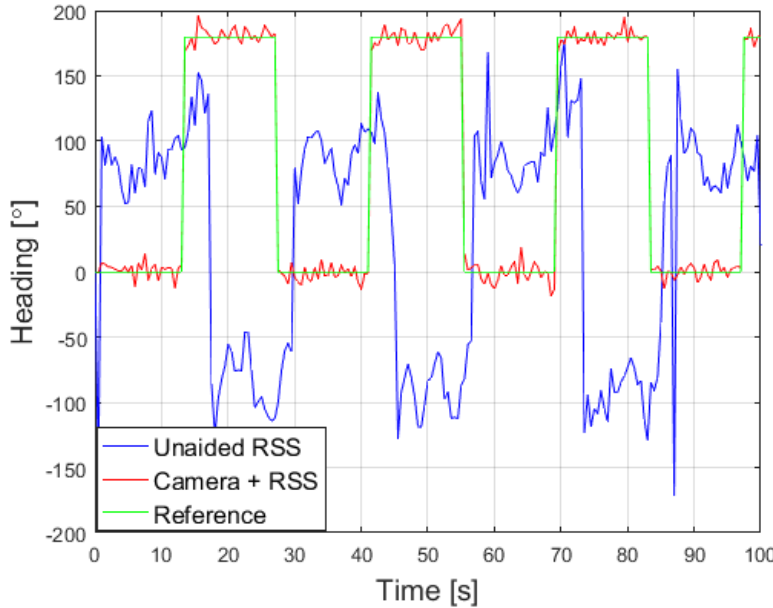


Figure 5.7 Reference heading, unaided RSS and camera-aided RSS heading estimates

The position observations as shown in Figure 5.6 were first processed by the unaided RSS Kalman filter as shown in Figure 5.1 to obtain unaided RSS system positioning results. The red line in Figure 5.9 shows position results in local coordinates. In general, the use of a dynamic model in the unaided RSS Kalman filter smooth the position observations, thus reducing their variances. Although the heading in this case is not directly tracked according to the definition of the state vector in (5.1), it is very useful for the following analysis and can be derived from v_E and v_N by

$$\theta = \text{atan}2(v_E, v_N) \quad (5.19)$$

Figure 5.7 shows the derived headings in unaided RSS case; considerable heading errors occur. While the use of the pedestrian dynamic model does constrain the spread of the position estimates, considerable heading errors introduce drift in the position states when using the dynamic model in the prediction stage. In other words, heading information from camera data

should be able to provide constraints on the heading state and further improve positions. With this in mind, the position and heading observations are then processed by the proposed camera-aided RSS Kalman filter shown in Figure 5.5 to obtain the camera-aided RSS system results. With the heading observations, Figure 5.7 shows the heading state tracking results. As compared to the heading estimates in the unaided RSS case, the use of heading observations in the camera-aided RSS Kalman filter allows for a more accurate tracking of the heading state. The updated variances of the position state in the west-east and south-north directions are shown in Figure 5.8 and Figure 5.9, respectively. It is shown that the variances of the position state are reduced in both directions by incorporating heading observations. The variances in the south-north direction appear to attain a periodic steady-state. To investigate this, the heading state in the camera-aided RSS Kalman filter is shown against the update variances in Figure 5.9. It clearly demonstrates that the periodic transition-state in the update variance is due to the heading changing by 180° periodically. After that, the Kalman filter “locks on” to the true state and the update variance becomes steady.

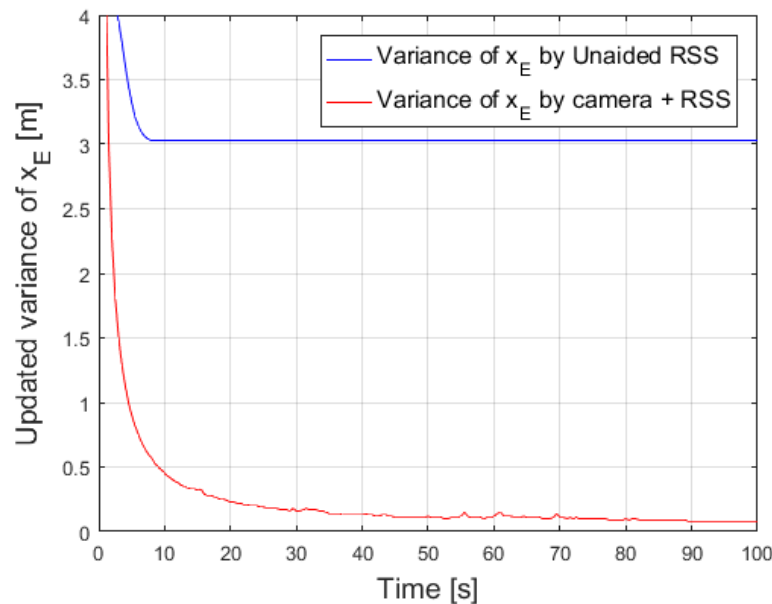


Figure 5.8: Updated variances of position state in west-east direction

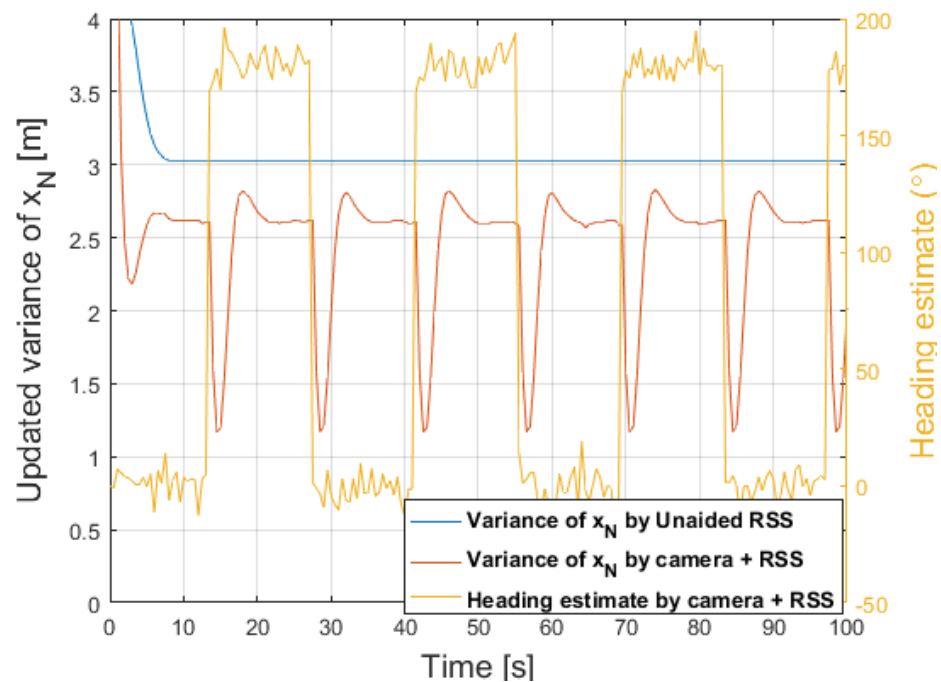


Figure 5.9: Updated variances of position state in south-north direction, as well as heading estimates of camera-aided RSS system

Figure 5.10 shows the position errors for both positioning systems over the duration of the entire simulation. While performance improvement is quite clear in the west-east direction, the improvement in the south-north direction is not. To analyze the position improvement in a statistical way, Figure 5.11 shows the position error percentiles for both systems. It is clear that performance is improved in both west-east and south-north directions by incorporating heading observation using the camera-aided RSS Kalman filter. It should be noted that the point of the simulation is to show how heading observation enhances the positioning performance. The simulation results show that the improvement in the west-east direction is greater than that in the south-north direction; this may not be the case when it comes to field data processing. In practice, the amount of improvement the proposed algorithm can provide depends on factors such as the modeling of the observation errors, the accuracy of the dynamic model, etc. In the following section, experimental data will be used to evaluate possible positioning performance improvements brought by the proposed algorithm.

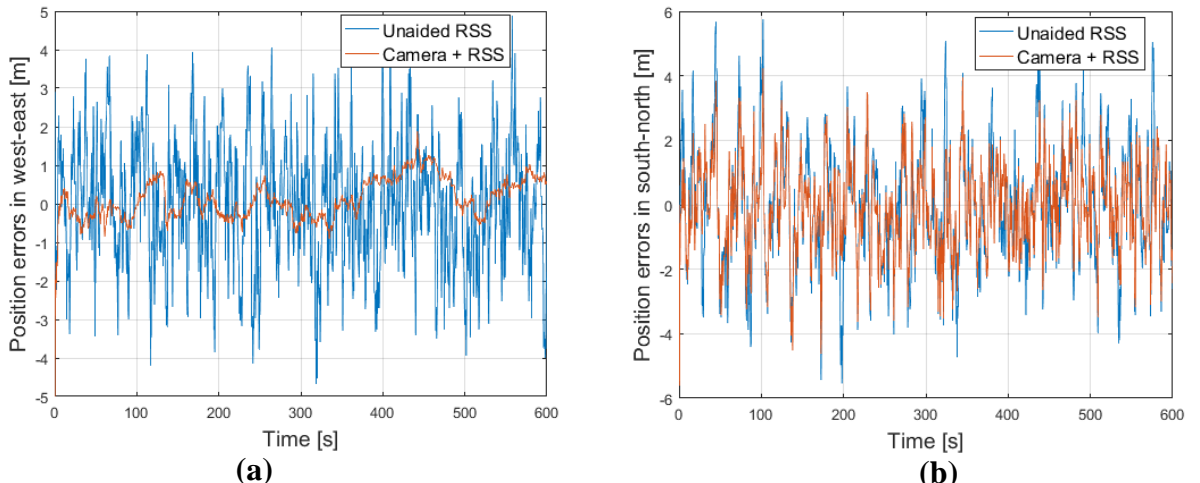


Figure 5.10: Position errors in (a) west-east direction (cross track) and (b) south-north direction (along track)

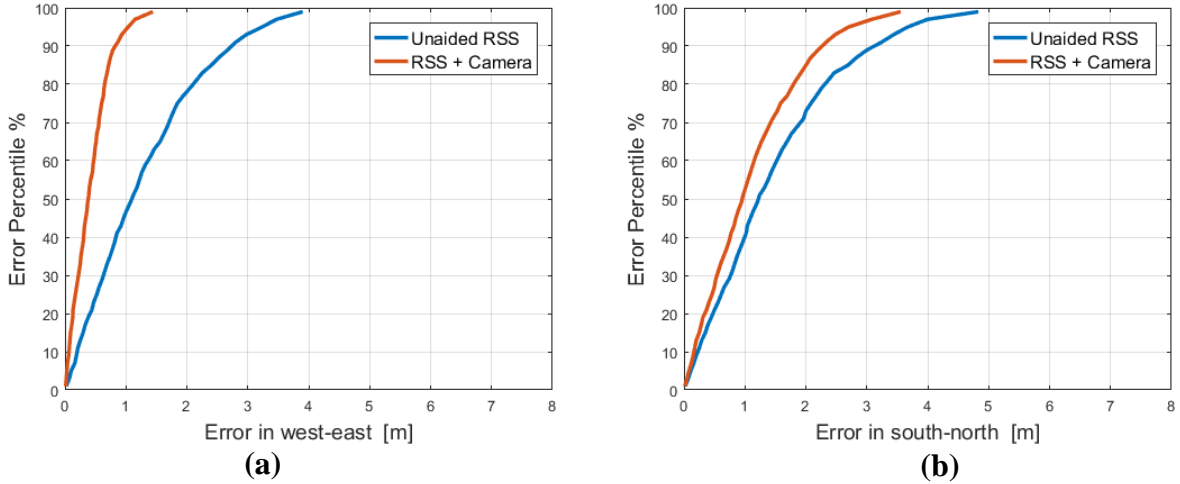


Figure 5.11: Position error percentiles in (a) west-east direction (cross track) and (b) south-north direction (along track)

5.2.3 Experimental Setup and Results Analysis

In this section, an experimental environment is setup in a typical office building using consumer grade Wi-Fi 2.4 GHz transceivers and security cameras for RSS and camera data collection. Experimental data is then used to analyze the heading estimator, and potential benefits of fusing camera-derived heading information into the RSS-based positioning system are assessed.

5.2.3.1 Experiment Setup and Data Collection

An experimental environment was set up and experiments were conducted in a typical office building as shown in Figure 5.12 (a). The test area measures approximately 8 m by 20 m. The primary pieces of experimental equipment are all consumer-grade and include a Google Nexus tablet, Wi-Fi routers and a security camera system for general surveillance. Figure 5.12 (b) shows a security camera installed to monitor a corridor in the office. The deployment of the APs and the security camera is shown Figure 5.13, where the APs are represented by blue stars and

the security camera by a red square. The AP deployment shown in Figure 5.13 is quite common for corridors, where the APs are distributed along the corridor and thus do not provide good geometry to localize a person in west-east direction as shown in Figure 5.13. Under such circumstances, it is easier to assess how the fusion of camera data can improve the positioning performance in this environment.

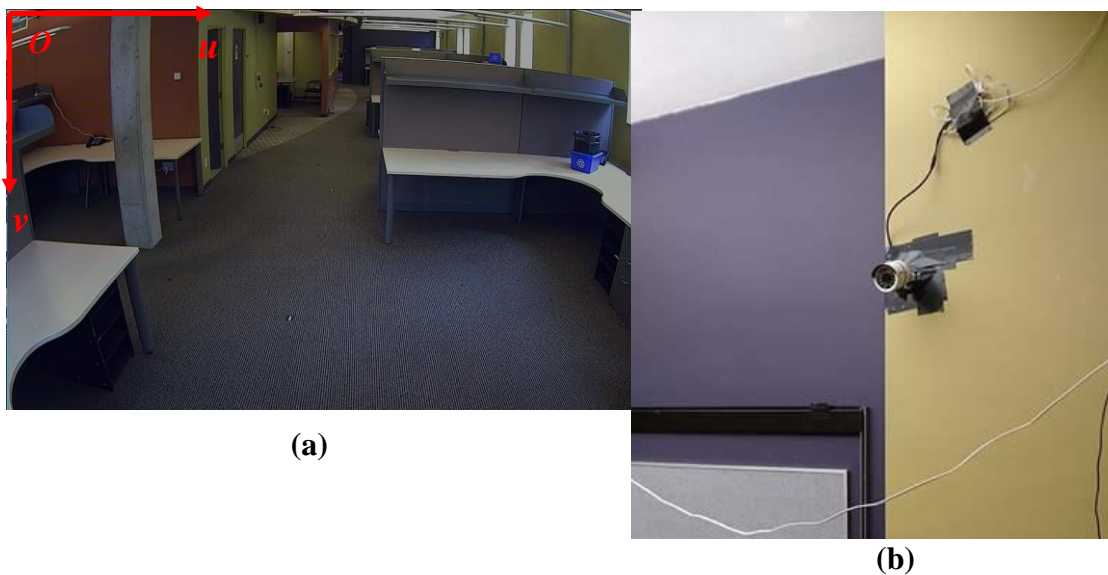


Figure 5.12: (a) Experimental environment in field of view of a security camera (b) a security camera

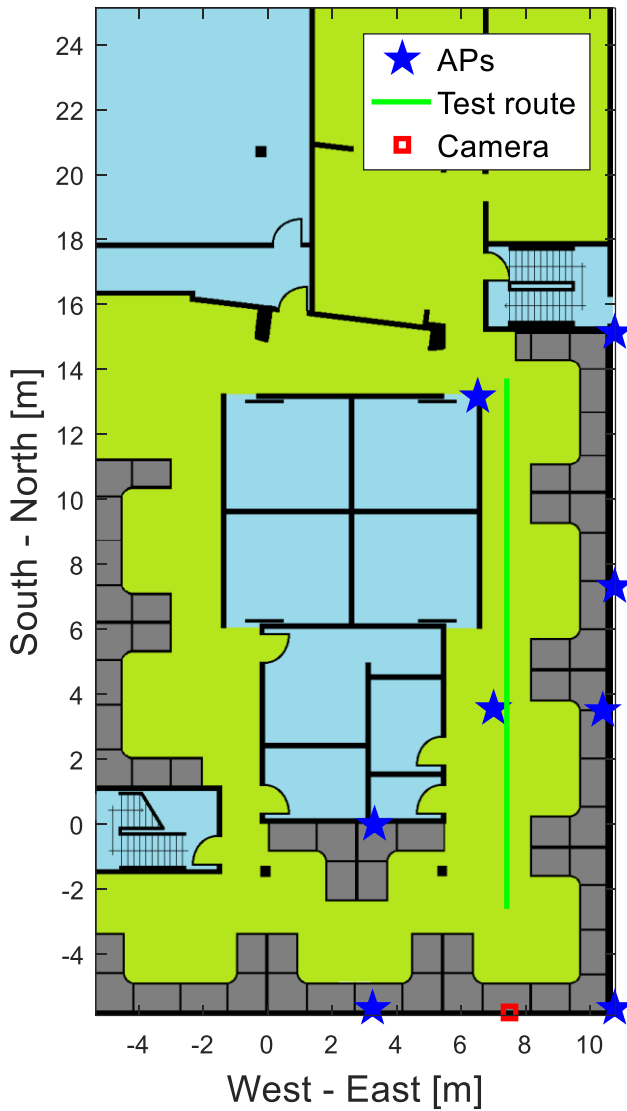


Figure 5.13: Floor plan, experimental setup and test route reference

The Google Nexus tablet was used to collect Wi-Fi RSS measurements and the RSS data rate is about 1.4 Hz. The Android application described in Appendix A was used in both calibration and tracking stages to collect and stream RSS measurements to files on the tablet for post-processing. Similarly, videos from the security camera data was streamed to and stored in a server for further processing. The frame rate of the video is 25 Hz and the dimension is 1280 by 720 pixels. To synchronize the RSS measurements and the video frame, both RSS data and video frames are

time tagged by their respective systems (Android and Linux systems) and the two systems are synchronized by Network Time Protocol (NTP). The NTP can usually maintain timing accuracy within tens of milliseconds over the public internet, which is sufficient for the experimental requirements herein.

In the pathloss model calibration stage, RSS measurements were collected in a set of RPs distributed in the test area to train the parameters of pathloss models, as discussed in Chapter 3. During the test, the tablet was held by the user walking at a speed of about 0.85 m/s for 10 minutes. The reference trajectory is shown in Figure 5.13 and was repeated 15 times. Figure 5.14 depicts how to obtain the reference solution with markers placed along the test route and the distances between them measured through a survey. The stop-watch feature developed in the Android application was used to record the time when the user arrived at a marker and pressed a button on the tablet. The position reference solution can be computed by the following method in post-processing. The person in the experiment walked very slowly and with an almost uniform speed, so a constant walking speed can be assumed between two adjacent markers (spacing being 0.5 m). Denote the timestamp of a measurement as t , and the two recorded adjacent times when the user arrived at the corresponding markers as t_n and t_m where $t_m > t_n$. The reference position where the measurement is obtained can be computed as

$$x_{ref} = \frac{x_m - x_n}{t_m - t_n} t \quad (5.20)$$

where x_n and x_m are the surveyed positions of the two corresponding markers. In the experiment, the distance between two adjacent markers is 0.5 m, which indicates that the accuracy of the position reference solution is better than 0.5 m.

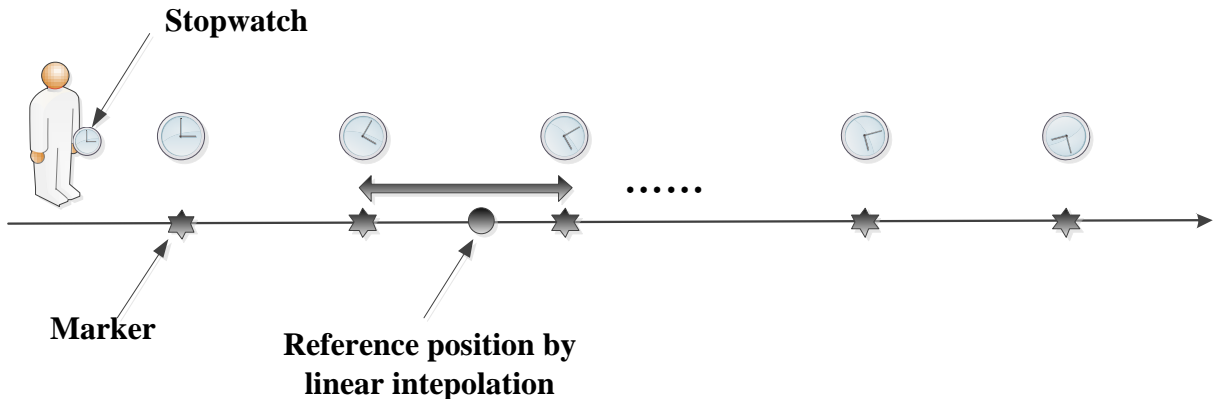


Figure 5.14: Method to obtain position reference solution

5.2.3.2 Heading Estimation Using CV Object Detection

Firstly, CV object detection results are generated using a camera tracking system developed by the research team and Figure 5.15 shows some results, where the green boxes represent the bounding boxes of the object detected and the red points, the GTPs. The top left sub-figure in Figure 5.15 gives an example of good detection results. However, as discussed before, due to the impairment in CV processing, considerable errors are present in some cases, as given by an example shown in the top-right sub-figure. Even worse, the example shown in the bottom-left sub-figure shows an example of false detection, and the bottom-right sub-figure shows a missing detection case. To gain an overview of the CV processing results, Figure 5.16 shows the GTPs of the detected object in the image v axis for the first 105 seconds. The image coordinate system is shown at the top left sub-figure of Figure 5.15. It can be seen that the CV processing results are quite noisy in pixel, which corresponds to the results shown in Figure 5.15. For example, CV either fails to detect the object, or the variance of the GTPs is quite large for the first 5 seconds. This is partly because the user was stationary for the first 5 seconds in the experiment and the CV detection system was not able to detect the object correctly with background subtraction algorithm. Additionally, in some area the detection results were completely wrong (e.g., at 45

seconds), as well as intermittent missing detection of object, especially when the user is far away from the camera. The CV processing performance can be improved by introducing extra processing (e.g. Bayesian filtering) in the CV processing domain; the focus here however is not to improve CV processing but to extract the information needed from it to enhance positioning.

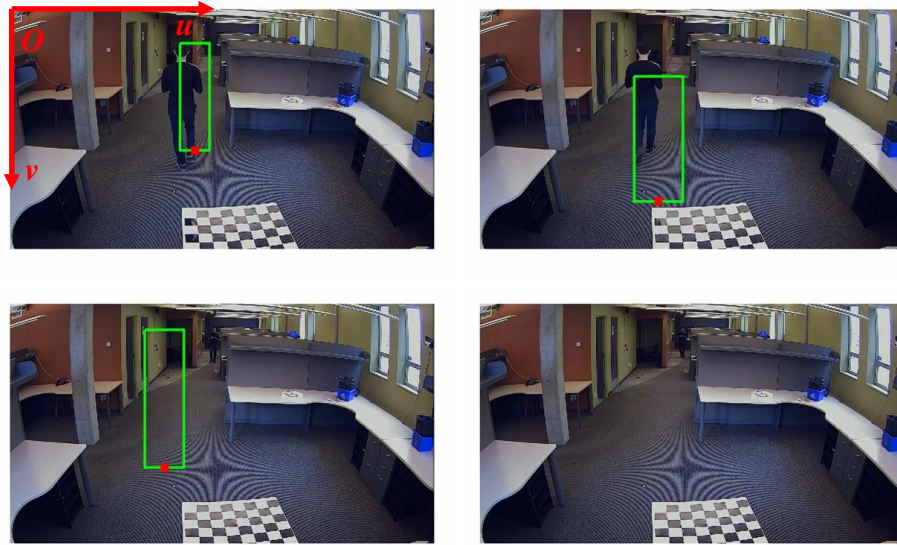


Figure 5.15: CV object detection results: (top left) good detection, (top right) detection with considerable error, (bottom left) false detection, (bottom right) missed detection

With the object detection results, the estimator proposed in (5.7) and (5.10) can be used to estimate the user's heading and then enhance positioning using the camera-aided RSS positioning system. However, due to the noisy nature of the CV processing results, there will be poor or even erroneous results in the heading estimates. Prior to incorporating such heading estimates in the positioning system, techniques must be developed to remove the erroneous results and/or indicate the confidence level of the heading estimates.

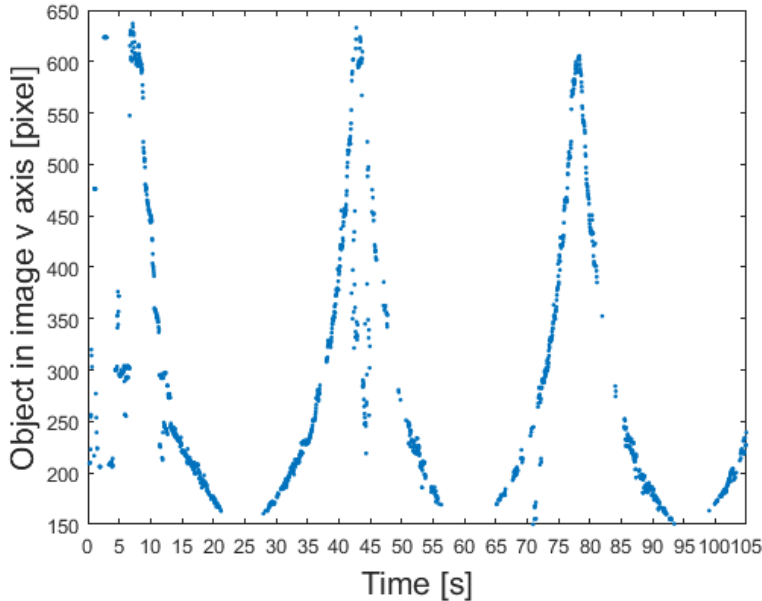


Figure 5.16: Object detected in image v axis by camera during the first 105 seconds

As mentioned previously, because the proposed heading estimator utilizes the change of the detected object in the image pixel plane to infer the user's heading, the change rate of the detected object in pixel provides a metric to determine the validity of the heading estimates. Specifically, when a user is stationary or is far away from the camera, the change of the detected object in the image is dominated by noise, so the sign of the pixel change rate in (5.7) carries no information regarding heading. The heading observations obtained in these cases should not be used to update the states in the Kalman filter. A straightforward way to utilize this metric in practice is to set a threshold against which the pixel change rate of the detected object is compared. A heading estimate associated with a pixel change rate lower than the threshold will then be eliminated. With heading estimates from the CV results, different threshold levels are tested and the corresponding Root Mean Square Errors (RMSE) and availability of the heading estimates are computed and shown in Figure 5.17. While the heading estimation availability drop

as the threshold increases is quite straightforward, it is interesting to observe that the threshold increase first reduces and then increases the heading estimates RMSE values. To investigate this issue, the GTPs of the detected object in the image v axis for three different cases are shown in Figure 5.18 by the blue points, along with the corresponding linear fitting lines given by the red plots. The pixel change rate estimate \hat{k} and the corresponding $\sqrt{SSR/L}$ (root of normalized SSR) are also shown in the corresponding sub-figures. While the first case shown in Figure 5.18 (a) is a normal case where heading can be estimated correctly, the other two cases represent two types of causes that lead to erroneous heading estimates. For the case in Figure 5.18 (b), the user was stationary during that time interval, resulting in a small pixel change rate and hence carrying no information regarding the heading. This type of heading estimation error can be removed by setting a proper threshold for the pixel change rate. For the case in Figure 5.18(c), the outliers in the object detection offset \hat{k} and result in an erroneous heading estimate. Note that this type of error cannot be eliminated even using a high threshold for \hat{k} . The aforementioned issue regarding the way the pixel change rate threshold affects the RMSE of heading estimates can now be explained. As the pixel change rate threshold increases, the heading estimate errors caused by the second cases can be removed, resulting in reduced heading estimate RMSE values. However, as the threshold continues to increase, the correct heading estimates, as shown in Figure 5.18(a), will also be removed, and the erroneous heading estimates, as shown by Figure 5.18 (c) will still exist in the remaining estimates. Therefore, the RMSE begins to increase as the threshold increases to some point.

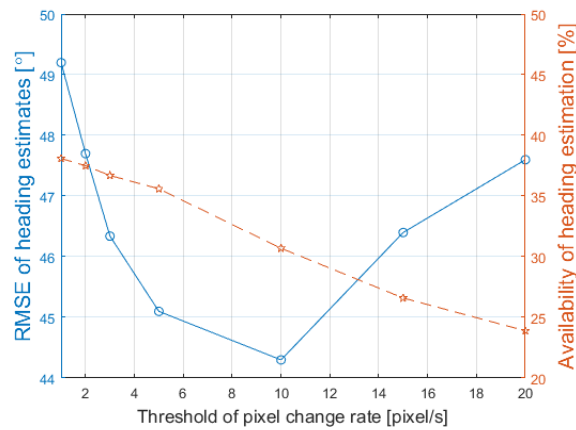


Figure 5.17: RMES and availability of heading estimates versus threshold of pixel change rate

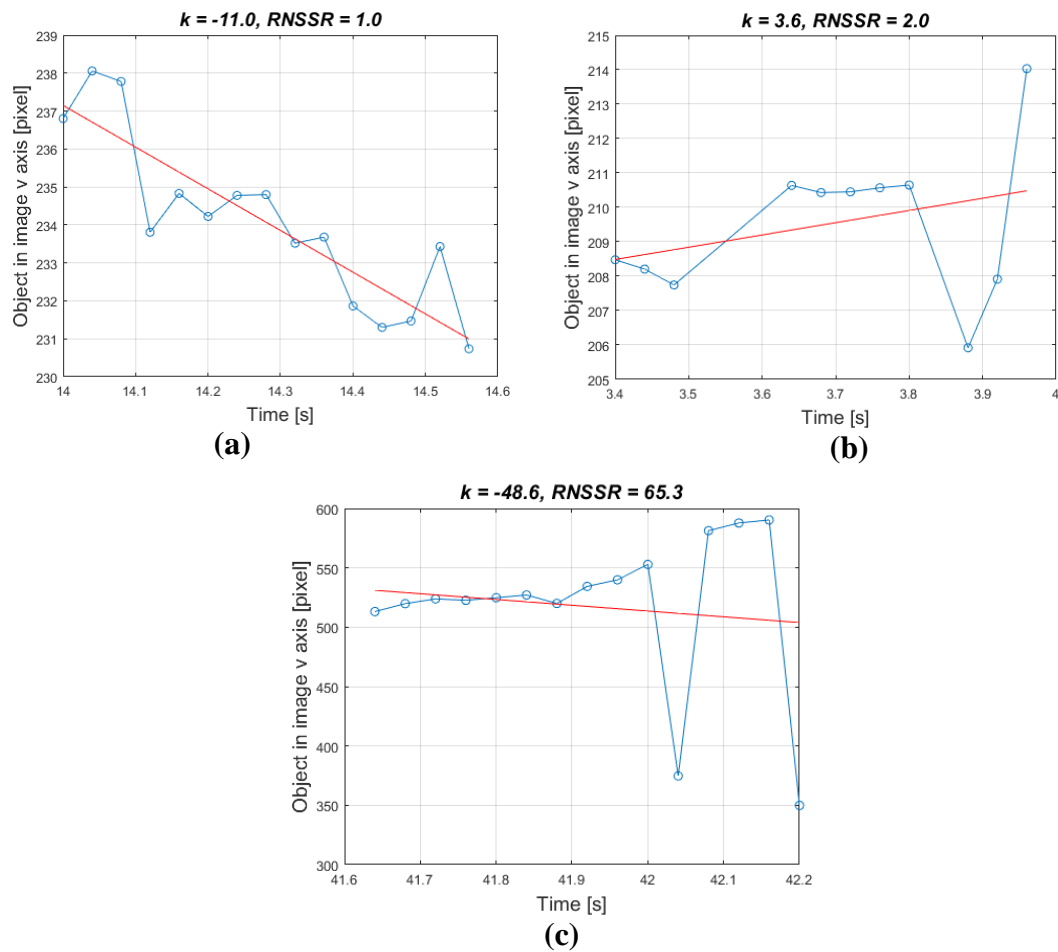


Figure 5.18: Object detected in image v axis for three cases and heading estimates: (a) heading obtained correctly, (b) low pixel change rate carrying no heading information, (c) heading obtained wrongly due to outliers.

To summarize, while setting a proper pixel change rate threshold can remove the type of heading estimate errors in the second case, it is not able to remove the errors associated with the third case. However, to fuse the heading observation into the following Kalman filter, the type of errors in the third case should also be removed. Note that, as shown in Figure 5.18 (c), the large $\sqrt{SSR/L}$ value in this case can indicate the high unreliability of the corresponding heading estimates.

The potential of SSR to indicate the reliability of the heading estimates was discussed in Section 5.2.1. To further evaluate the practical utility of SSR indicating the reliability of the heading estimates, the heading estimation errors and the corresponding $\sqrt{SSR/L}$ values are plotted in Figure 5.19 for the first 50 s of the experiment, in which the correlation of the $\sqrt{SSR/L}$ and heading estimation errors is quite clear. A practical method that utilizes the SSR to improve heading estimation is to set a threshold for $\sqrt{SSR/L}$ to eliminate the type of errors in the third case shown in Figure 5.18 (c). Specifically, a heading estimate associated with a $\sqrt{SSR/L}$ larger than the threshold should be eliminated. Similar to the analysis of the threshold for the pixel change rate above, different $\sqrt{SSR/L}$ threshold levels are tested and the corresponding RMSE and the availability of the heading estimates are computed and shown in Figure 5.20. While the decline in estimation availability as the threshold decreases is straightforward, it is interesting to observe that the decreasing of the threshold level first reduces and then increases the RMSE of heading estimates. This is because the threshold decline first eliminates the type of heading errors shown in the third case in Figure 5.18 (c). However, as the threshold continues to drop and

becomes too small, some accurate heading estimates will also be removed, and therefore the RMSE of heading estimates will begin to increase.

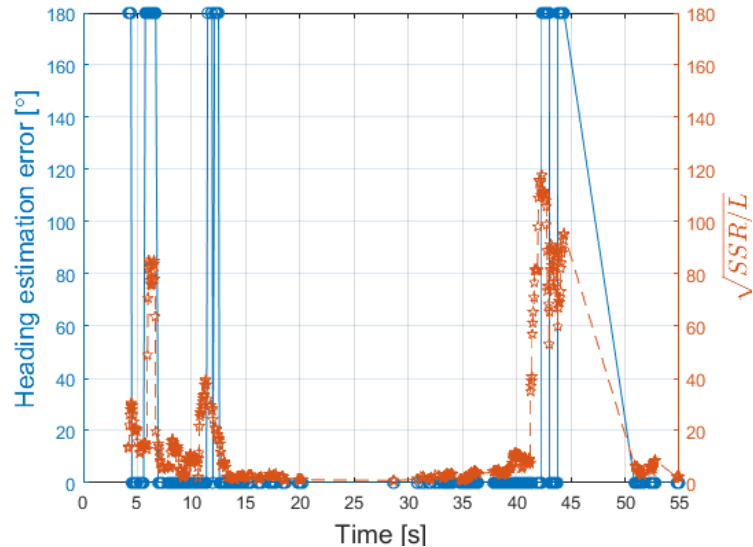


Figure 5.19: Heading estimation errors and root of normalized SSR

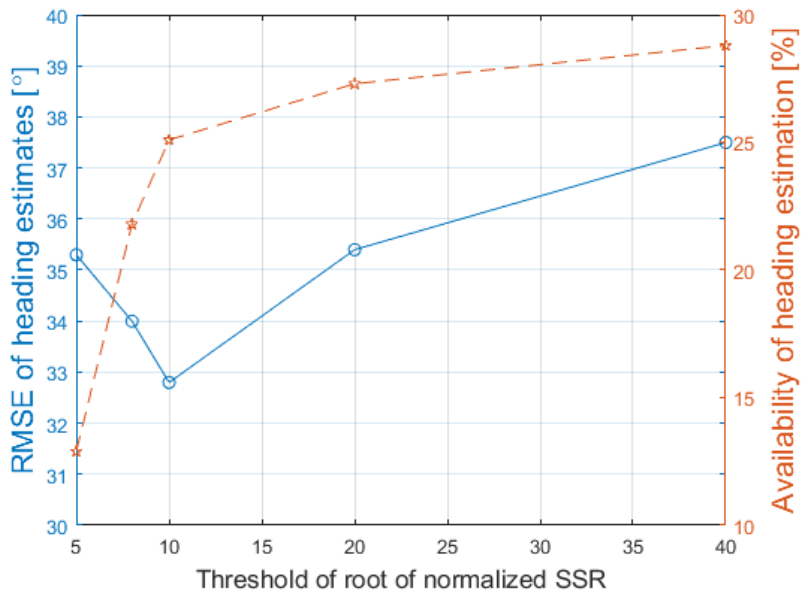


Figure 5.20: RMSE and availability of heading estimates versus threshold of root of mean SSR

In summary, this section proposed a heading estimator that makes use of the CV processing results. To deal with the heading estimation errors due to noisy CV processing results, thresholds of pixel change rate and roots of normalized SSR are developed to eliminate erroneous heading estimates. Experimental results and analysis demonstrate that for each of the thresholds, there exists an optimum value to attain minimum heading estimation RMSE. Note that the optimum values for the thresholds mentioned above are based on the specific camera data used in the thesis. In practice, the optimum values need to be tuned for specific scenarios.

5.2.3.3 Camera-aided RSS Positioning System Enhancement

With heading observations provided by the heading estimator, the performance of the proposed camera-aided RSS positioning system can now be evaluated and compared to that of the unaided RSS system. To do this, position observations from RSS trilateration are fed to the unaided RSS system as shown in Figure 5.1, while the camera-aided RSS system is provided with position and heading observations as shown in Figure 5.5.

Figure 5.21 shows the heading state tracking results in the camera-aided RSS Kalman filter for the first 250 s. Overall, the Kalman filter can track the heading accurately when provided with accurate heading observations. However, it exhibits considerable errors in two scenarios. The first scenario is lack of observations, and one such example is highlighted with the red ellipse in Figure 5.21. This is either due to the CV processing missing detection of the object, or to the use of thresholds eliminating the heading estimates that are unreliable, as discussed before. The second scenario is that the heading observation contains errors and hence offsets the heading state tracking. One such example is highlighted with the black ellipse.

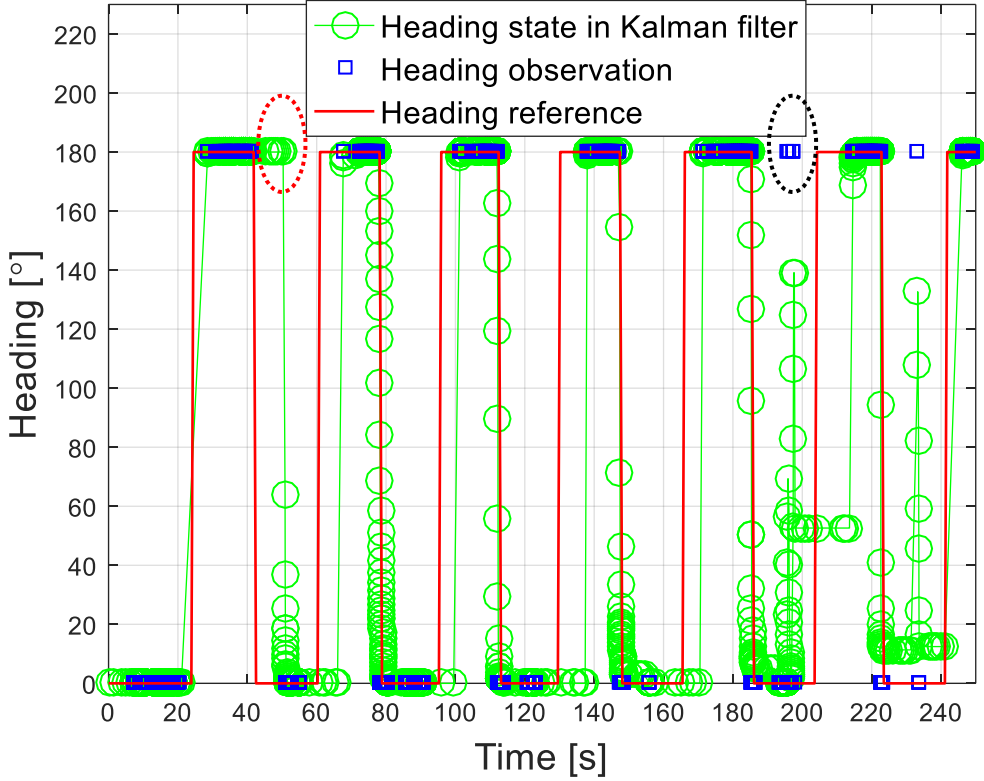


Figure 5.21: Heading state tracked in camera-aided RSS system

To evaluate the performance improvement brought by the camera-aided RSS system, the position results of the unaided RSS system are first shown in Figure 5.22 in blue, overlaid on the floor plan. Since the geometry of the Wi-Fi APs does not provide a good constraint in the west-east direction, the tracking precision is diluted in this direction for the unaided RSS system. The positioning results of the camera-aided RSS system are shown in red in Figure 5.22. Obviously, the position errors in the west-east direction are reduced because the heading observations constrain the position state update, which is consistent with the simulations results shown in Section 5.2.2. Looking closer at the details for both systems, the position error over time and the percentiles of the position error in the west-east direction are shown Figure 5.23(a) and Figure 5.24 (a), respectively. While the use of heading observations almost uniformly reduces the west-

east direction errors, the interval highlighted by the black ellipse in Figure 5.23 (a) exhibits poor performance. This corresponds to the interval when erroneous heading state estimates are present at about 200 s in Figure 5.21. For position performance in the south-north direction, the position errors over time and their percentiles in the west-east direction are shown in Figure 5.23(b) and Figure 5.24 (b), respectively, for both systems. Significant performance improvement can be seen in this direction by using the camera-aided RSS system. This is because the heading observations improve the heading state tracking in the Kalman filter, thus improving the position state propagation in this direction. Figure 5.23(c) and Figure 5.24 (c) show the horizontal position errors over time and their percentiles for both systems. The position RMSEs of both systems are listed in Table 5.1. There are 25% and 38% position RMSE improvements in the east and north axes, respectively, resulting in a 37 % position RMSE improvement horizontally as compared to the unaided RSS system.

To summarize, by fusing the heading information from the security camera using the proposed camera-aided RSS system, the positioning performance is improved significantly. It is also worth noting that, in the west-east direction (perpendicular to corridor direction), more improvement is possible if more constraints can be used, for example in Figure 5.22, the position estimates located in walls are obviously not reasonable and should be corrected by introducing map information. This will be done next to further improve performance.

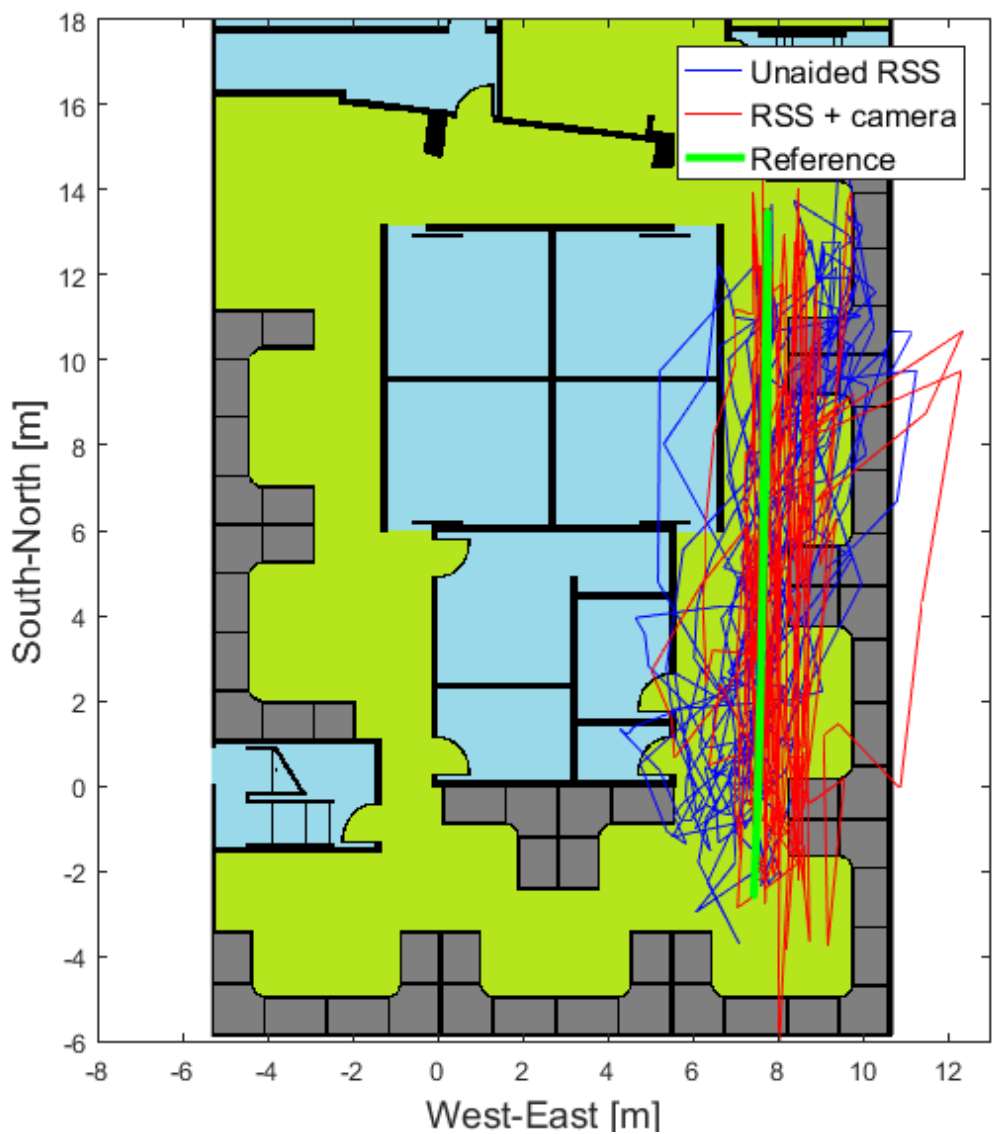


Figure 5.22: Position results of unaided RSS and camera-aided RSS systems

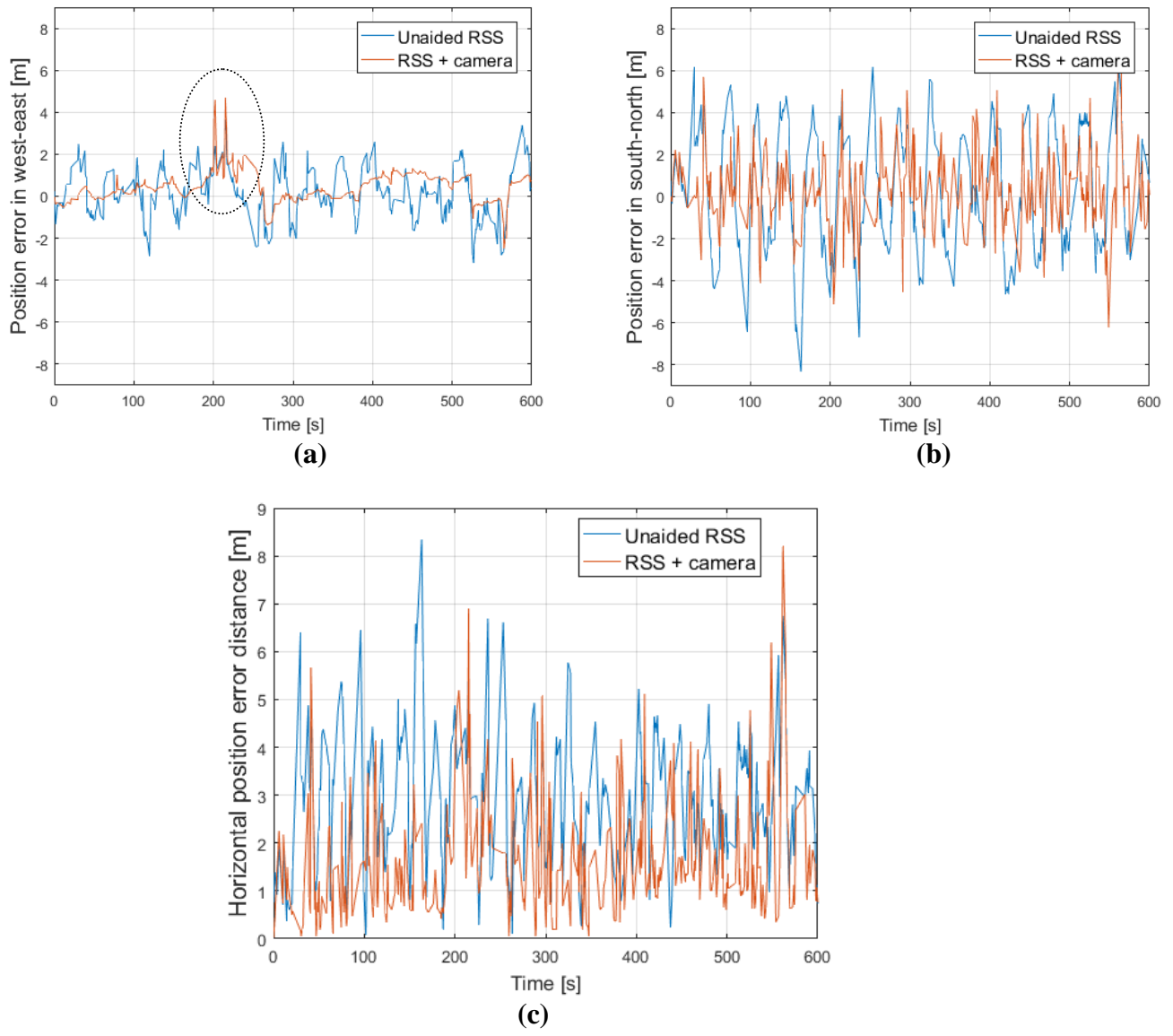


Figure 5.23: Position for unaided RSS and camera-aided RSS systems (a) errors in west-east (cross track), (b) errors in south-north (along track) and (c) horizontal errors

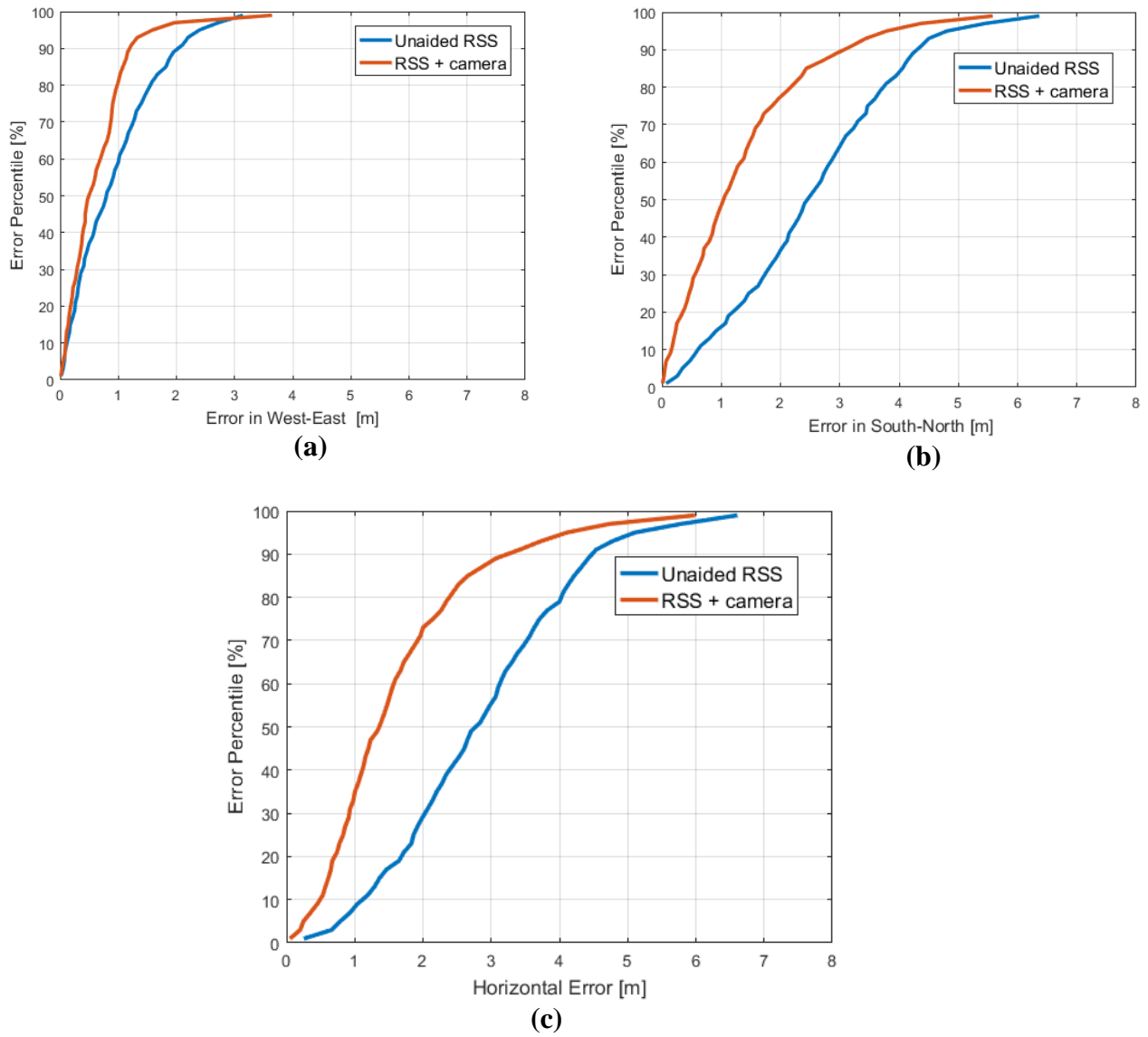


Figure 5.24: Position performance of unaided RSS and camera-aided RSS systems (a) errors in west-east (cross track), (b) errors in south-north (along track) and (c) horizontal errors

Table 5.1. Position RMSE for unaided RSS and camera-aided RSS systems

Positioning systems	West-east RMSE [m]	South-north RMSE [m]	Horizontal RMSE [m]
Unaided RSS	1.2	2.9	3.2
Camera-aided RSS	0.9	1.8	2.0

5.3 Fusing Building Map and Security Cameras to Enhance RSS-based Positioning

As discussed in the experimental result analysis for the camera-aided RSS positioning system, further improvement in positioning performance is possible if building map information can be incorporated. This can be done using map-matching techniques. As introduced in the beginning of this chapter, building map information is a form of constraint that helps better model the state propagation and provides state prior distribution. This distribution then weighs the measurement likelihood function to produce more accurate state a posteriori distribution and hence a more accurate state estimate of position. This section aims to combine RSS, a security camera and building map information for indoor positioning. A map-camera-aided RSS positioning system is proposed based on a particle filter. To evaluate the performance improvement obtained by further incorporating map information, the experimental data used in the last section is re-processed using this system. Positioning performances metrics of the unaided RSS, camera-aided RSS and map-camera-aided RSS systems are then compared and analyzed.

5.3.1 Map Constraint Information Representation

As discussed in Chapter 1, when using map-matching techniques, one key component is the map information representation. A commonly used map representation is Computer Aided Drawing (CAD) floor plan that provides information on building walls and corridors. Figure 5.25(a) shows an example of one such CAD floor plan. As can be seen, hallways, cubicles, rooms, etc. can be identified. Similar to (Walder and Bernoulli, 2010), the information needed from a floor plan to create map constraints for the following map-matching approaches consists of:

- Polygons of the outlines of different areas such as the desks, rooms, etc.

- Walkability of each polygon that indicates if the corresponding area is walkable and/or accessible. For example, desk areas are not walkable. More information can contribute to these properties—for example, a visitor is not allowed to enter any room, and the polygons representing rooms are labeled as non-accessible accordingly.



Figure 5.25: (a) Floor plan and (b) map constraints (polygons with different outline colors represent different regions)

The polygons extracted from the floor plan along with the corresponding walkability property of each polygon can be used to construct map constraints for map-matching. Note that although

map information representation is an essential part of map-matching algorithms, it is not the focus of this thesis, and most of the information can be extracted from a CAD floor plan or Computer Aided Facility Management (CAFM) using existing algorithms (Walder and Bernoulli, 2010). To isolate the noise embedded in the floor plan and better evaluate the map-matching approaches developed, this thesis chooses to generate the polygons manually from the floor plan. Furthermore, it assumes a visitor tracking scenario, therefore some rooms are not accessible. Figure 5.25(b) shows the map constraints derived from the floor plan shown in Figure 5.25(a), in terms of polygon and corresponding walkability, where the shaded regions represent the corresponding areas that are not walkable. These map constraints will be used for the map-matching approaches described in the sequel.

5.3.2 Map-camera-aided RSS Positioning System based on Particle Filtering

Another key component of map-matching techniques is the matching method. The most widely used matching method for indoor positioning is the probabilistic method based on Bayesian filter theory (Xiao et al 2014). As introduced in Chapter 2, in probabilistic map-matching, the map information is used to constrain the state transition model for state estimation improvement. Normally, the map constraints are high-nonlinear (Xiao et al 2014) and hence the state transition model is as well. In this case, the assumption for using a Kalman filter to implement the Bayesian filter does not hold any more. However, a particle filter is known for its ability to model nonlinear transformation of random variables and thus is widely used in indoor map-matching techniques as discussed in Chapter 2.

Next, consider how to integrate the map constraint and camera data into the RSS positioning system. The observation model and the state transition model used in the camera-aided RSS

system can still be used, but in addition to the PDR model, the map constraint also needs to be integrated to the state transition model. Moreover, due to the use of the particle filter, the state distributions are no longer represented by Gaussian variables as in the Kalman filter case. Instead, they are approximated by a set of particles. Figure 5.26 proposes a map-camera-aided RSS positioning system based on such a particle filter.

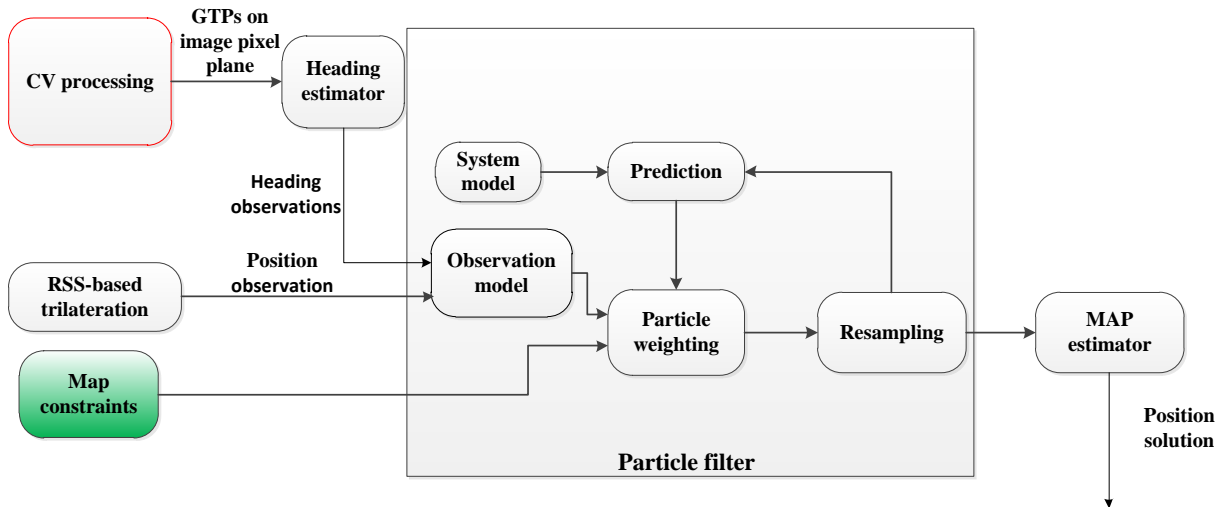


Figure 5.26: Map-camera-aided RSS positioning system based on particle filtering

Denote the particles' state vector at time step k as $\mathbf{x}_k^n, n=1,2,\dots,N$ where N is the number of particles. Similar to the state vector definition of the camera-aid RSS Kalman filter in (5.13), each particle in the particle filter shown in Figure 5.26 represents a state vector:

$$\mathbf{x} = [E \ N \ v_h \ \theta]^T \quad (5.21)$$

The corresponding weights associated with the particles are denoted as $\omega_k^n, n=1,2,\dots,N$. The key idea of map-matching utilizing a particle filter is that the map constraints are used to weigh the particles before the importance resampling stage. Specifically, a particle representing a position in a non-walkable area is assigned a weight of zero. The main steps in implementing a

particle filter were introduced generally in Chapter 2. The follow discussion focuses on the details in each of the components, specifically for realizing the map-camera-aided RSS positioning system.

- Prediction Sampling

In prediction sampling step, the a posteriori distribution of the previous step is propagated according to a system dynamic model. This is done by propagating the set of particles drawn from the a posteriori distribution of the previous step to a new set of particles that approximates the predicted distribution. The same system state model as that used in the camera-aided RSS system can be used, namely

$$\begin{aligned}\dot{E} &= v_h \sin \theta \\ \dot{N} &= v_h \cos \theta \\ \dot{v}_h &= \eta_{v_h} \\ \dot{\theta} &= \eta_\theta\end{aligned}\tag{5.22}$$

Specifically, the particles are propagated as follows:

$$\mathbf{x}_k^n = \begin{bmatrix} 1 & 0 & \Delta t \sin \theta & 0 \\ 0 & 1 & \Delta t \cos \theta & 0 \\ 0 & 0 & 1 & 0 \\ 0 & 0 & 0 & 1 \end{bmatrix} \mathbf{x}_{k-1}^n + \begin{bmatrix} \frac{\Delta t^2 \sin \theta}{2} & 0 \\ \frac{\Delta t^2 \cos \theta}{2} & 0 \\ \Delta t & 0 \\ 0 & \Delta t \end{bmatrix} \begin{bmatrix} \eta_{v_h} \\ \eta_{v_\phi} \end{bmatrix}\tag{5.23}$$

- Importance Weighting

The weight associated with each particle drawn from the predicted distribution is calculated in this stage. These weights are used to incorporate observations and map-constraints into the particle set. Specifically, the weight of a particle is calculated by

$$\omega_k^n = \omega_{obs}^n(k) \omega_{map}^n(k) \omega_{k-1}^n \quad (5.24)$$

where $\omega_{obs}^n(k)$ is the weight of the particle based on observations and $\omega_{map}^n(k)$ based on map constraint at k time step. The $\omega_{obs}^n(k)$ are computed by the likelihood of the observation \mathbf{z}_k under the particle \mathbf{x}_k^n , which is

$$\omega_{obs}^n(k) = p(\mathbf{z}_k | \mathbf{x}_k^n) \quad (5.25)$$

For the weights derived from map constraints, it is computed by

$$\omega_{map}^n(k) = \begin{cases} 0 & \text{particle is in non-walkable area} \\ 1 & \text{particle is in walkable area} \end{cases} \quad (5.26)$$

which finishes the incorporation of map constraints into the particle set.

- Resampling

In the resampling stage, the particle set that approximates the prediction distribution is transformed into a new set by incorporating the particle weights derived in the last stage. The details of the resampling algorithm can be found in Chapter 2. After resampling, the distribution of particles approximates the a posteriori distribution of the state. Note that if the resampling is triggered, the particles will be set to an equal weight as

$$\omega_k^i = \frac{1}{N} \quad (5.27)$$

since the particle weight information has been incorporated in resampling. If a resampling is not performed, the particle weights will be propagated to the next time step, as already indicated by (5.24).

- Positioning solution

The positioning solution can now be inferred based on the a posteriori distribution of the states approximated by the particles. A Maximum a posteriori (MAP) estimator is adopted, namely

$$\hat{\mathbf{x}}(k) = \sum_{n=1}^N \omega_k^n \mathbf{x}_k^n \quad (5.28)$$

Note that if the resampling is triggered, the state estimation is simply the mean of the particles.

5.3.3 Experimental Results and Analysis

In order to evaluate the performance of the map-camera-aided RSS positioning system, the experimental data used previously for analyzing the unaided RSS and the camera-aided RSS systems is re-processed. The CAD floor plan of the experimental environment is used to provide map constraints, which as shown in Figure 5.25(a). The map constraints represented by polygons for different areas as well as the corresponding walkability are created and shown in Figure 5.25(b). In the data processing, the position observations from RSS trilateration, the heading observations from the proposed heading estimator and the map constraints are processed by the map-camera-aided RSS positioning system as shown in Figure 5.26.

To investigate how the map constraints improve positioning, Figure 5.27(a) first shows the position states of the particles at a certain epoch after resampling (the weights of particles are equal), without map-matching. A comparison with the true position shows that the position states of the particles are offset. This is not an uncommon scenario for RSS-based positioning due to the considerable uncertainty as discussed in previous chapters. Without using the map constraint, the position estimate is computed by (5.28) and shown as the green dot in Figure 5.27(a). It can be seen that it is offset correspondingly and results in a position error of about 3 m. By using the map-constraint to weigh the particle using (5.26), Figure 5.27 (b) shows the surviving particles

and the corresponding final position estimate which is now in error by 2 m. Map-matching appears to mitigate the position error in west-east, while there is little change in the south-north. This is because there are few features in the map that provides a constraint along the corridor. Also, the map feature provides more significant constraints along the west-east and thus improves performance.

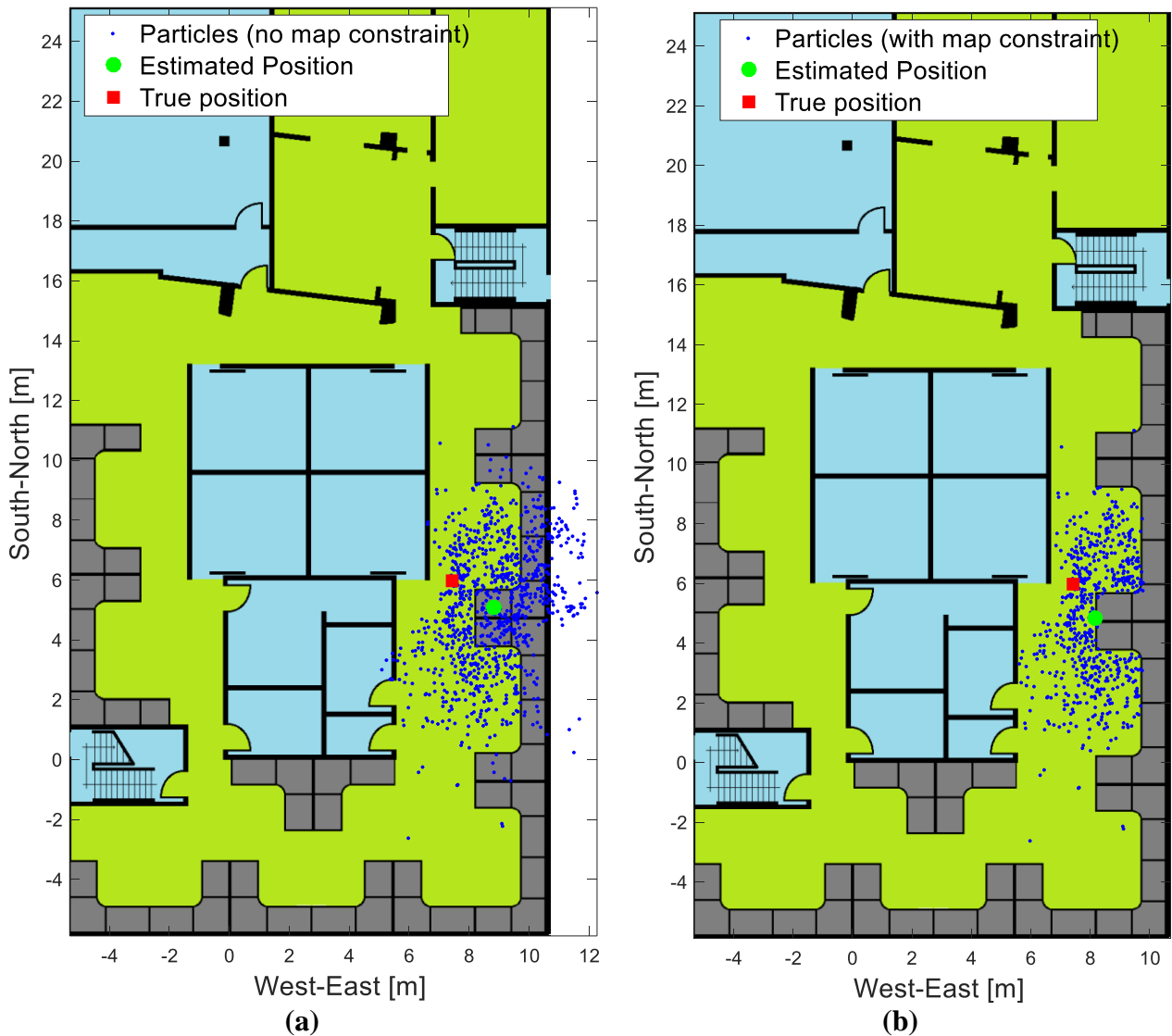


Figure 5.27: Position particle distribution and estimated positions (a) without map constraints and (b) with map constraints

Figure 5.28 shows the position errors in the west-east, south-north and horizontal. The corresponding plots for the camera-aided RSS system are also shown for comparison. It can be found that the improvement brought by the map constraint is mainly west-east. It is interesting to see that the considerable position errors in west-east due to the erroneous heading observations from camera data, as highlighted by the black ellipse in Figure 5.28(a), are mitigated by using map constraints. To see the statistical positioning performance of the map-camera-aided system, the error percentile plots corresponding to Figure 5.28 are shown in Figure 5.29. While the performance improvement obtained by incorporating both the camera data and map information is quite definite as compared to the unaided RSS system, it is interesting to examine the respective contributions from the camera data and map information. By comparing the position errors of different systems in the south-north components shown in Figure 5.29(b), it can be seen that there are obvious performance improvements in the systems that include the camera. However, the performance between the camera-aided RSS and map-camera-aided RSS systems are not significant different in this case. This indicates that the performance contribution along the south-north direction is mainly from the camera data. The map information of the test area considered herein does not contribute to the position improvement in the south-north direction, and this is because there is little feature that provides constraints along the corridor direction, as discussed previously. However, the map feature provides more significant constraints in the west-east direction and thus improves performance. As can be seen in Figure 5.29 (a), the use of map constraints enhances performance by mitigating almost all positioning errors levels in the west-east direction. Since the position errors in the south-north direction are more significant than those in the west-east direction, the overall horizontal positioning performance is dominated

by that of the south-north component. Therefore, the horizontal positioning improvement brought by map, as shown in Figure 5.29 (c), is less significant than that in the west-east direction. Figure 5.30 shows the position results overlaid on the floor plan, in which the improvement in the west-east direction is quite clear. It is worth noting, however, that the estimated trajectory in some regions seems to cross the wall, even after taking into account the map constraints. This is because the map constraint herein takes a quite simple form, namely each particle is weighed based on its position at a certain epoch, without considering the particle propagation over time. More sophisticated map constraints (e.g., considering trajectory pattern over time) can be used to further improve positioning performance. However, the focus of using map-matching in this thesis is based upon the feasibility of integrating both camera data and map information into an RSS-based system and the positioning performance improvement that can be achieved by doing so; thus more sophisticated map-matching algorithms are beyond the scope of the thesis. Based on the Table 5.1, Table 5.2 further lists the position RMSE in the west-east, south-north and horizontal component for the map-camera-aided RSS system. It is shown that the west-east position RMSE is further reduced by about 0.5 m by considering the map constraints used in the thesis.

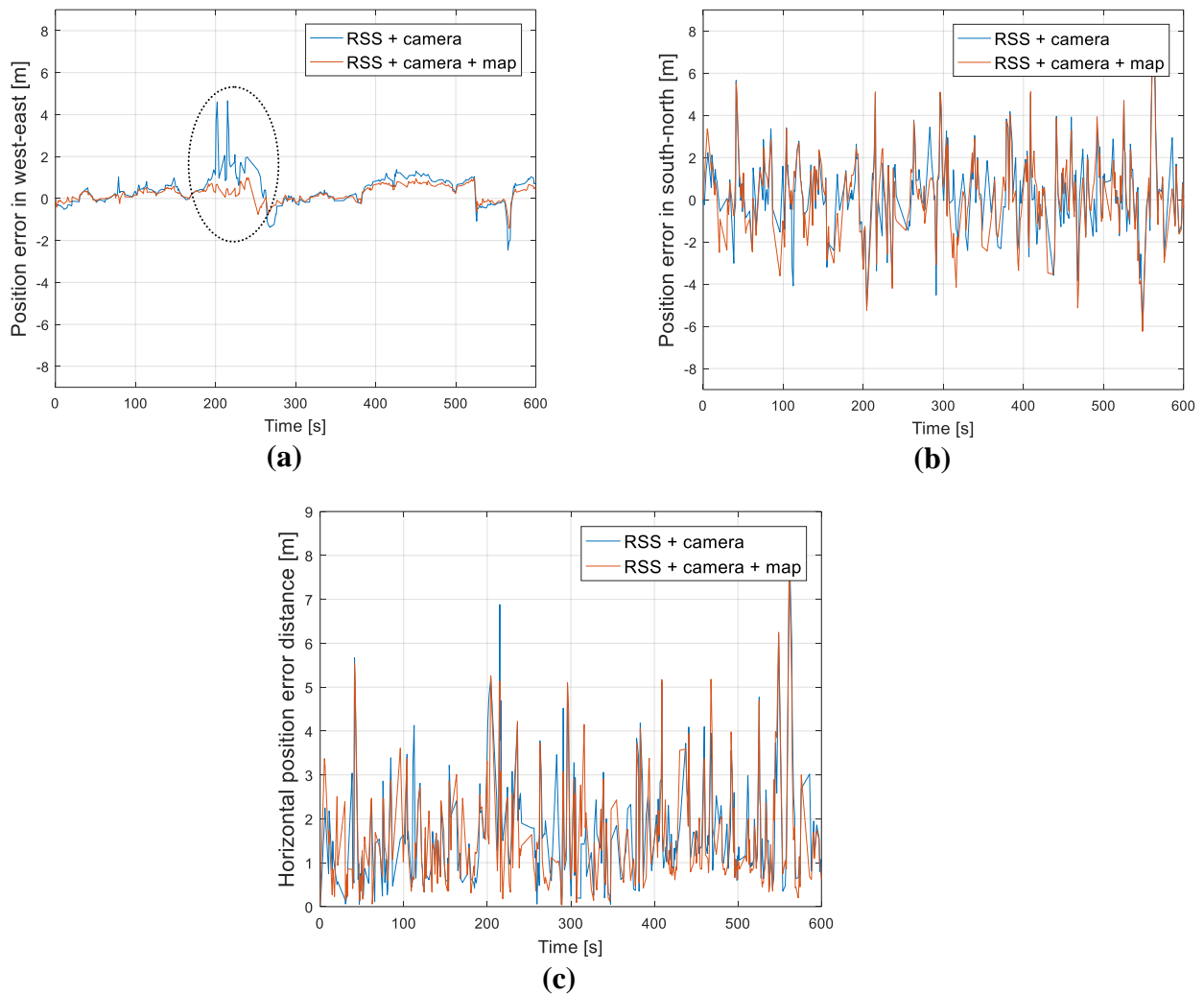


Figure 5.28: Position for camera-aided RSS and map-camera-aided RSS systems (a) errors in west-east (cross track), (b) errors in south-north (along track) and (b) horizontal errors

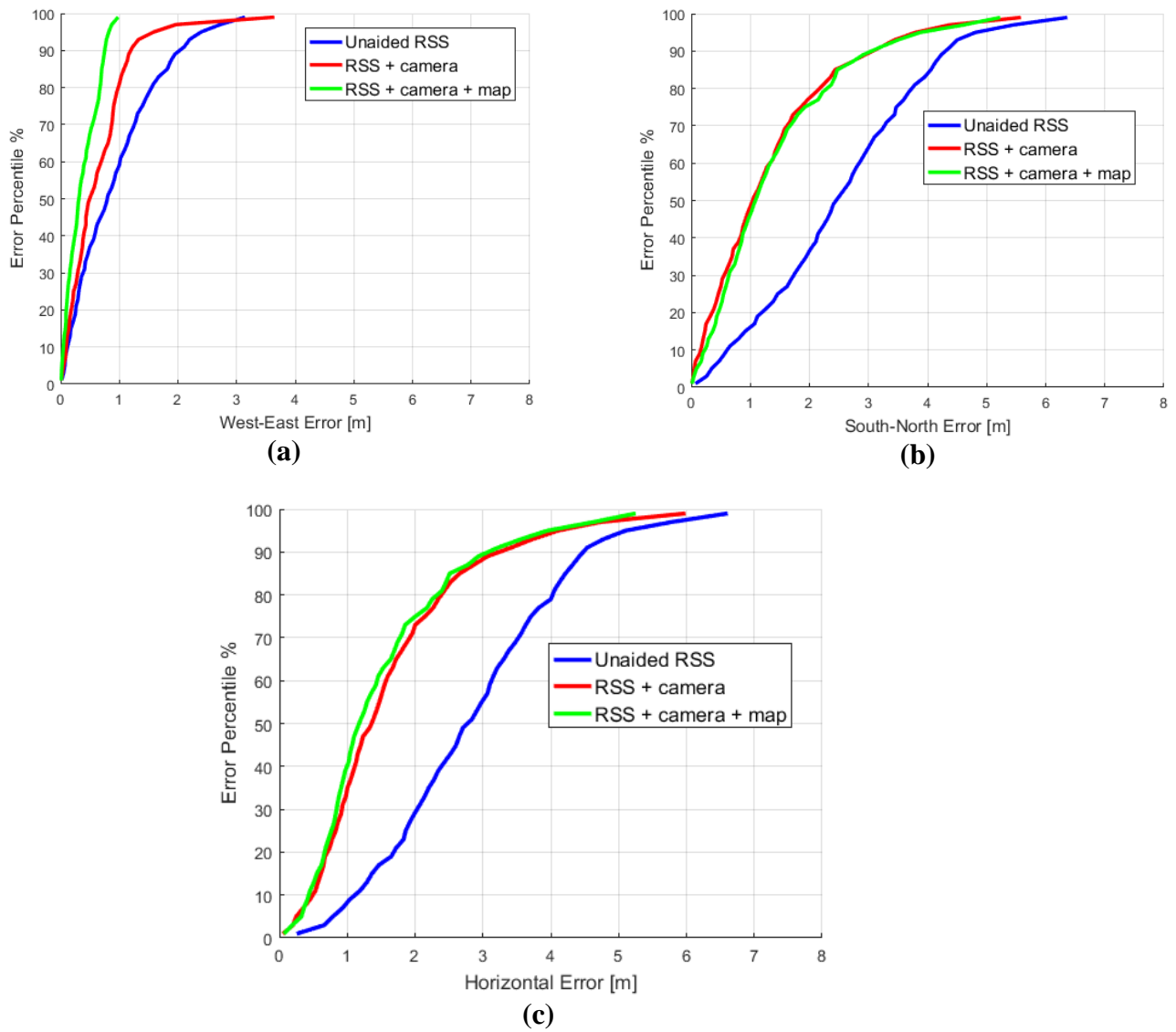


Figure 5.29: Position error percentiles of unaided RSS, camera-aided RSS and map-camera-aided systems (a) error percentiles in west-east (cross track), (b) error percentiles in south-north (along track) and (c) horizontal error percentiles

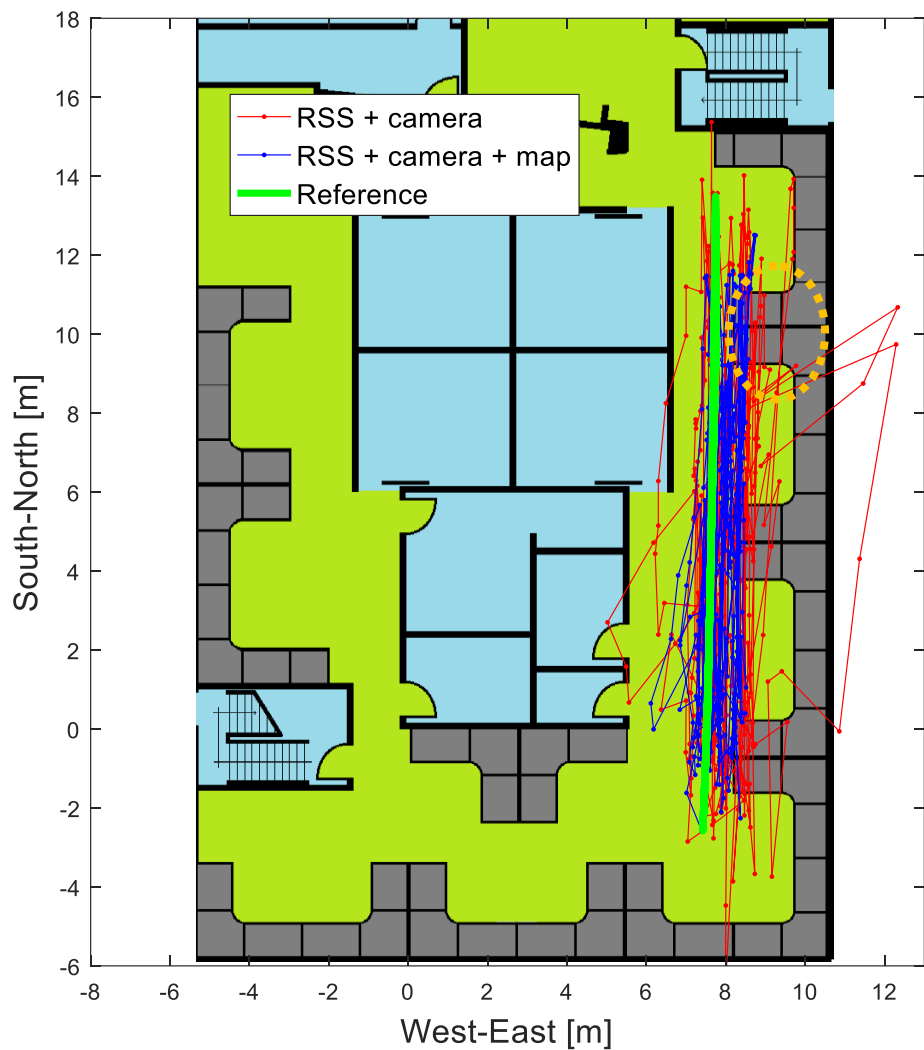


Figure 5.30: Position results of camera-aided RSS and map-camera-aided RSS systems

Table 5.2. Position RMSE for unaided RSS, camera-aided RSS and map-camera-aided RSS systems

Positioning systems	West-east RMSE [m]	South-north RMSE [m]	Horizontal RMSE [m]
Unaided RSS	1.2	2.9	3.2
Camera-aided RSS	0.9	1.8	2.0
Map-camera-aided RSS	0.5	1.8	1.9

5.4 Summary

This chapter investigated the use of prior information from security cameras and building maps to enhance RSS-based indoor positioning. It has been demonstrated that it is feasible to use an uncalibrated camera to infer a user's heading in corridors. A heading estimator based on the change of the detected object in the image pixel plane was developed. Tools have been developed to improve heading estimation by setting thresholds to eliminate erroneous estimates. A camera-aided RSS positioning system based on Kalman filtering was proposed to incorporate the heading observation in order to enhance positioning performance and simulations were conducted to assess its effectiveness. To further incorporate building map information, a map-camera-aided RSS positioning system based on particle filter was proposed. An experimental environment was set up in an office, and experiments were conducted to test the proposed algorithms. For the camera-aided RSS system, heading observations from CV processing improve heading tracking performance and thus positioning performance. There are 25% and 38% position RMSE improvements in the cross track and along track directions, respectively, resulting in 37% position RMSE improvement in the 2D horizontal plane as compared to the unaided RSS system. By further incorporating building map constraints with the map-camera-aided system, there is a 44% position RMSE improvement in the cross track direction as compared to the camera-aided RSS positioning system.

Chapter Six: Conclusions and Recommendations

This chapter first summarizes the salient conclusions made in this thesis, followed by providing recommendations for future work.

6.1 Conclusions

As discussed in Chapter 1, the major objective of this thesis was to model the body shadowing effect on RSS measurements and incorporate additional information from security cameras and building maps to enhance RSS-based indoor positioning. To this end, experimental data was collected in various outdoor and indoor environments to characterize RSS signal characteristics for both 2.4 GHz and 5 GHz Wi-Fi signals, especially the uncertainty in RSS incurred by human body shadowing. Based on the characterization, an empirical body shadowing loss model was proposed to improve RSS modeling and a MLE estimator based on this model was developed to enhance RSS positioning. To incorporate security camera for enhancing RSS positioning, a heading estimator making use of CV processing was proposed and a camera-aided RSS system based on it was developed. To further incorporate building map information, a map-camera-aided system was developed. Experiments were conducted to evaluate the proposed algorithms. Overall, it was shown that the proposed empirical body shadowing loss model can partially model the RSS body shadowing loss. When a user's heading is constrained, the proposed MLE based on this model has shown its ability to improve positioning performance. It was also demonstrated that, by incorporating security camera and building map information into the RSS positioning system using the proposed algorithms, that the positioning performance was significantly improved. The detailed conclusions arising from the thesis are as follows:

- 1) Indoor RSS measurement characterization

- i. RSS variations of Wi-Fi 2.4 GHz signals are larger than those of 5 GHz signal in both outdoor and indoor environments. When it comes to indoor environments, the harsh indoor signal propagations conditions increase RSS variations for both bands. Moreover, considerable outliers are present in the 2.4 GHz signals, which increase considerably RSS variations. However, this is not the case for the 5 GHz signals. Therefore, it is more advantageous to utilize 5 GHz RSS for positioning.
 - ii. For 2.4 GHz Wi-Fi RSS, the body shadowing loss in indoor environments is less significant as compared to the RSS uncertainties caused by other factors such as interference and multipath. Therefore for 2.4 GHz signals, it is difficult to characterize the body shadowing effect and there is negligible loss in information by ignoring the body shadowing.
 - iii. For 5 GHz RSS in indoor environments, the RSS shadowing loss becomes apparent (can be up to 10 dB) only when a person is close to a mobile or the AP (less than about 2 to 3 m). In this case, the loss can be associated with the blocking angle.
 - iv. In the case of a mobile being close to the user (less than 0.3 m), RSS shadowing loss generally decreases as the absolute value of the blocking angle increases; however, as the absolute value of the blocking angle becomes greater than a certain value (about 51 ° for the data in this thesis), the RSS shadowing loss becomes negligible. In indoor environments, the body shadowing loss is influenced by multipath, and the body shadowing loss becomes negligible when multipath dominates.
- 2) RSS body shadowing loss modeling for enhancing RSS positioning

- i. Based on the RSS body shadowing loss characterization, an empirical loss model with small number of parameters was proposed to model the dependence of body shadowing loss on the blocking angle which can be associated with user's heading (assume the user holds the mobile device out front). Moderate amount of training data was used to estimate the parameters of the body shadowing loss model.
 - ii. By incorporating the proposed body shadowing loss model with the conventional RSS measurement model that only considers pathloss, a MLE was proposed to jointly estimate the user's position and heading. It has demonstrated experimentally that the utility of the body shadowing loss model for improving positioning relies on the accuracy of heading estimates and is affected by multipath signals. If the user's heading is unknown and has to be estimated jointly with position, 70% of test cases have improvement, and the overall position RMSE has an 8% improvement. If the user's heading is constrained, then 83% test cases have improvement and the overall position RMSE has a 25% improvement.
- 3) Incorporating security cameras and building maps for enhancing RSS positioning
 - i. It is feasible to use an uncalibrated camera to infer a user's heading in corridors and a heading estimator based on the pixel change rate of the detected object on image was developed. A threshold based on the pixel change rate of the detected object can be used to remove the heading estimate errors when the detected user shows little motion. Another threshold based on SSR can be used to evaluate the heading estimate reliability and remove the heading estimate errors.

- ii. A camera-aided RSS positioning system based on Kalman filtering was proposed to incorporate heading observations in order to enhance positioning. It was experimentally shown that the heading observations from CV processing improve the heading state tracking and thus positioning performance. There are 25% and 38% position RMSE improvements in the cross track and along track directions, respectively, resulting in a 37% position RMSE improvement in horizontal as compared to an unaided RSS system.
- iii. A map-camera-aided RSS positioning system based on particle filtering was proposed to further incorporate building map information. It was experimentally shown that the use of map constraints further brings 44% position RMSE improvement in the across track direction as compared to the camera-aided RSS positioning system.

Based on these conclusions, the initial hypotheses stated in Section 1.3 have been addressed with the outcome that simple RSS models factoring in body shadowing do indeed improve the overall information provided by RSS measurements as manifested by the modest improvements in location accuracy. In addition, inclusion of uncalibrated camera data and knowledge of building maps can provide significant improvement.

6.2 Recommendations for future work

Some recommendations to improve and extend this research in future are as follows:

- 1) Different body types are supposed to influence body shadowing loss differently. To isolate this effect, the RSS measurements were collected by a single person for analyzing the body shadowing loss in this thesis. The research can be extended by collecting RSS

with different persons to analyse the effect of different body types on the RSS body shadowing loss.

- 2) Train the body shadowing loss model in more environments and analyse how the model parameters change as a function of environment, which can be used to further evaluate the practicality of the body shadowing loss model.
- 3) The body shadowing loss model becomes more effective when user's heading is constrained and constraining of heading to true values has shown to improve positioning apparently in the thesis. This work can be extended by using sensors (e.g., magnetometers, and/or gyros) to estimate user' heading and then evaluating the effectiveness of the body shadowing loss modeling and positioning performance conditioned on the heading estimates from sensors.
- 4) Extend the camera-aided RSS positioning system to more general cases by considering multiple object detection and in multiple indoor environments (e.g., spatial room). The key issues are how to maintain the heading estimation of individual persons and how to provide constraints in different environments.
- 5) Extend the use of build map information by incorporating more sophisticated map constraints, e.g., heading constraints, trajectory constraints, etc.

References

- AALTO, L., GÖTHLIN, N., KORHONEN, J. & OJALA, T. Bluetooth and WAP push based location-aware mobile advertising system. Proceedings of the 2nd international conference on Mobile systems, applications, and services, 2004. ACM, 49-58.
- AMANI, N., DEHGHANIAN, V. & NIELSEN, J. User-induced antenna variation and its impact on the performance of RSS-based indoor positioning. Electrical and Computer Engineering (CCECE), 2016 IEEE Canadian Conference on, 2016. IEEE, 1-5.
- ARULAMPALAM, M. S., MASKELL, S., GORDON, N. & CLAPP, T. 2002. A tutorial on particle filters for online nonlinear/non-Gaussian Bayesian tracking. *IEEE Transactions on signal processing*, 50, 174-188.
- ASCHER, C., KESSLER, C., WANKERL, M. & TROMMER, G. Dual IMU Indoor Navigation with particle filter based map-matching on a smartphone. Indoor positioning and indoor navigation (IPIN), 2010 international conference on, 2010. IEEE, 1-5.
- ATTIA, M., MOUSSA, A., ZHAO, X. & EL-SHEIMY, N. 2011. Assisting personal positioning in indoor environments using map matching. *Archiwum Fotogrametrii, Kartografii i Teledetekcji*, 22.
- BAHL, P. & PADMANABHAN, V. N. RADAR: An in-building RF-based user location and tracking system. INFOCOM 2000. Nineteenth Annual Joint Conference of the IEEE Computer and Communications Societies. Proceedings. IEEE, 2000. Ieee, 775-784.
- BARCELO, F., EVENNOU, F., DE NARDIS, L. & TOME, P. Advances in indoor location. LIAISON-ISHTAR Workshop, 2006.
- BENBASAT, A. Y. & PARADISO, J. A. An inertial measurement framework for gesture recognition and applications. International Gesture Workshop, 2001. Springer, 9-20.
- BRADSKI, G. & KAEHLER, A. 2008. *Learning OpenCV: Computer vision with the OpenCV library*, " O'Reilly Media, Inc.".
- BREITENSTEIN, M. D., REICHLIN, F., LEIBE, B., KOLLER-MEIER, E. & VAN GOOL, L. 2011. Online multiperson tracking-by-detection from a single, uncalibrated camera. *IEEE transactions on pattern analysis and machine intelligence*, 33, 1820-1833.
- CHEN, Y.-C., CHIANG, J.-R., CHU, H.-H., HUANG, P. & TSUI, A. W. Sensor-assisted wi-fi indoor location system for adapting to environmental dynamics. Proceedings of the 8th

ACM international symposium on Modeling, analysis and simulation of wireless and mobile systems, 2005. ACM, 118-125.

CUCCHIARA, R., GRANA, C., PICCARDI, M. & PRATI, A. 2003. Detecting moving objects, ghosts, and shadows in video streams. *IEEE transactions on pattern analysis and machine intelligence*, 25, 1337-1342.

DAVIDSON, P., COLLIN, J. & TAKALA, J. Application of particle filters for indoor positioning using floor plans. *Ubiquitous Positioning Indoor Navigation and Location Based Service (UPINLBS)*, 2010, 2010. IEEE, 1-4.

DELLA ROSA, F., PELOSI, M. & NURMI, J. 2012. Human-induced effects on rss ranging measurements for cooperative positioning. *International Journal of Navigation and Observation*, 2012.

DELLA ROSA, F., XU, L., NURMI, J., LAOUDIAS, C., PELOSI, M. & TERREZZA, A. Hand-grip and body-loss impact on RSS measurements for localization of mass market devices. *2011 International Conference on Localization and GNSS (ICL-GNSS)*, 2011.

EVENNOU, F. & MARX, F. 2006. Advanced integration of WiFi and inertial navigation systems for indoor mobile positioning. *Eurasip journal on applied signal processing*, 2006, 164-164.

EVENNOU, F., MARX, F. & NOVAKOV, E. Map-aided indoor mobile positioning system using particle filter. *IEEE Wireless Communications and Networking Conference*, 2005, 2005. IEEE, 2490-2494.

FARSHAD, A., LI, J., MARINA, M. K. & GARCIA, F. J. A microscopic look at WiFi fingerprinting for indoor mobile phone localization in diverse environments. *Indoor Positioning and Indoor Navigation (IPIN)*, 2013 International Conference on, 2013. IEEE, 1-10.

FERRIS, B., HAEHNEL, D. & FOX, D. Gaussian processes for signal strength-based location estimation. In proc. of robotics science and systems, 2006. Citeseer.

GOLDSMITH, A. 2005. *Wireless communications*, Cambridge university press.

GU, Y., LO, A. & NIEMEGEERS, I. 2009. A survey of indoor positioning systems for wireless personal networks. *IEEE Communications surveys & tutorials*, 11, 13-32.

HE, Z., PETOVELLO, M. & LACHAPELLE, G. 2014. Indoor doppler error characterization for high sensitivity GNSS receivers. *IEEE Transactions on Aerospace and Electronic Systems*, 50.

HE, Z., RENAUDIN, V., PETOVELLO, M. G. & LACHAPELLE, G. 2013. Use of high sensitivity GNSS receiver doppler measurements for indoor pedestrian dead reckoning. *Sensors*, 13, 4303-4326.

HONKAVIRTA, V., PERALA, T., ALI-LOYTTY, S. & PICHE, R. A comparative survey of WLAN location fingerprinting methods. *Positioning, Navigation and Communication*, 2009. WPNC 2009. 6th Workshop on, 2009. IEEE, 243-251.

JIANG, J.-H., LE, H.-L. & SHIE, S.-C. Lightweight Topological-Based Map Matching for Indoor Navigation. 2016 30th International Conference on Advanced Information Networking and Applications Workshops (WAINA), 2016. IEEE, 908-913.

JIMENEZ, A. R., SECO, F., PRIETO, C. & GUEVARA, J. A comparison of pedestrian dead-reckoning algorithms using a low-cost MEMS IMU. *Intelligent Signal Processing*, 2009. WISP 2009. IEEE International Symposium on, 2009. IEEE, 37-42.

KAY, S. M. 1993. Fundamentals of statistical signal processing, volume I: estimation theory.

KHAN, M. I. & SYRJARINNE, J. Investigating effective methods for integration of building's map with low cost inertial sensors and wifi-based positioning. *Indoor Positioning and Indoor Navigation (IPIN)*, 2013 International Conference on, 2013. IEEE, 1-8.

KING, T., KOPF, S., HAENSELMANN, T., LUBBERGER, C. & EFFELSBERG, W. COMPASS: A probabilistic indoor positioning system based on 802.11 and digital compasses. *Proceedings of the 1st international workshop on Wireless network testbeds, experimental evaluation & characterization*, 2006. ACM, 34-40.

KLEPAL, M. & BEAUREGARD, S. A backtracking particle filter for fusing building plans with PDR displacement estimates. *Positioning, Navigation and Communication*, 2008. WPNC 2008. 5th Workshop on, 2008. IEEE, 207-212.

KRISHNAKUMAR, A. & KRISHNAN, P. The theory and practice of signal strength-based location estimation. 2005 International Conference on Collaborative Computing: Networking, Applications and Worksharing, 2005. IEEE, 10 pp.

KRUMM, J., HARRIS, S., MEYERS, B., BRUMITT, B., HALE, M. & SHAFER, S. Multi-camera multi-person tracking for easyliving. *Visual Surveillance*, 2000. Proceedings. Third IEEE International Workshop on, 2000. IEEE, 3-10.

- LANGENDOEN, K. & REIJERS, N. 2003. Distributed localization in wireless sensor networks: a quantitative comparison. *Computer Networks*, 43, 499-518.
- LEITCHNER, J., FOX, D. & LAMARCA, A. Large-scale localization from wireless signal strength. Proceedings of the national conference on artificial intelligence, 2005. Menlo Park, CA; Cambridge, MA; London; AAAI Press; MIT Press; 1999, 15.
- LI, X. 2006. RSS-based location estimation with unknown pathloss model. *IEEE Transactions on Wireless Communications*, 5, 3626-3633.
- LI, X., PAHLAVAN, K., LATVA-AHO, M. & YLIANTTILA, M. Comparison of indoor geolocation methods in DSSS and OFDM wireless LAN systems. Vehicular Technology Conference, 2000. IEEE-VTS Fall VTC 2000. 52nd, 2000. IEEE, 3015-3020.
- LI, Y. 2014. *Spatial Coherency Estimation with a Synthetic Array*. University of Calgary.
- LI, Y. 2015. *Integration of MEMS Sensors, WiFi, and Magnetic Features for Indoor Pedestrian Navigation with Consumer Portable Devices*. University of Calgary.
- LI, Y., HE, Z., NIELSEN, J. & LACHAPELLE, G. Using Wi-Fi/magnetometers for indoor location and personal navigation. Indoor Positioning and Indoor Navigation (IPIN), 2015 International Conference on, 2015. IEEE, 1-7.
- LIU, H., DARABI, H., BANERJEE, P. & LIU, J. 2007. Survey of wireless indoor positioning techniques and systems. *IEEE Transactions on Systems, Man, and Cybernetics, Part C (Applications and Reviews)*, 37, 1067-1080.
- LO, B. & VELASTIN, S. Automatic congestion detection system for underground platforms. Intelligent Multimedia, Video and Speech Processing, 2001. Proceedings of 2001 International Symposium on, 2001. IEEE, 158-161.
- LUI, G., GALLAGHER, T., LI, B., DEMPSTER, A. G. & RIZOS, C. Differences in RSSI readings made by different Wi-Fi chipsets: A limitation of WLAN localization. 2011 International Conference on Localization and GNSS (ICL-GNSS), 2011. IEEE, 53-57.
- LUO, W., XING, J., ZHANG, X., ZHAO, X. & KIM, T.-K. 2014. Multiple Object Tracking: A Literature Review. *arXiv preprint arXiv:1409.7618*.
- MAUTZ, R. 2012. Indoor positioning technologies. ETH Zurich, Department of Civil, Environmental and Geomatic Engineering, Institute of Geodesy and Photogrammetry Zurich.

MAUTZ, R. & TILCH, S. Survey of optical indoor positioning systems. IPIN, 2011. 1-7.

MIYAKI, T., YAMASAKI, T. & AIZAWA, K. Tracking persons using particle filter fusing visual and Wi-Fi localizations for widely distributed camera. 2007 IEEE International Conference on Image Processing, 2007. IEEE, III-225-III-228.

NIELSEN, C., NIELSEN, J. & DEHGHANIAN, V. Fusion of security camera and RSS fingerprinting for indoor multi-person tracking. Indoor Positioning and Indoor Navigation (IPIN), 2016 International Conference on, 2016. IEEE, 1-7.

NIELSEN, J. & NIELSEN, C. 2016. Assessment of Receiver Signal Strength Sensing for Location Estimation Based on Fisher Information. *Sensors*, 16, 1570.

NURMINEN, H., KOIVISTO, M., ALI-LÖYTTY, S. & PICHÉ, R. Motion model for positioning with graph-based indoor map. Indoor Positioning and Indoor Navigation (IPIN), 2014 International Conference on, 2014. IEEE, 646-655.

NURMINEN, H., RAITOHARJU, M. & PICHÉ, R. An efficient indoor positioning particle filter using a floor-plan based proposal distribution. 2016 19th International Conference on Information Fusion (FUSION), 2016. IEEE, 541-548.

PAPAIOANNOU, S., WEN, H., MARKHAM, A. & TRIGONI, N. Fusion of radio and camera sensor data for accurate indoor positioning. 2014 IEEE 11th International Conference on Mobile Ad Hoc and Sensor Systems, 2014. IEEE, 109-117.

PEI, L., GUINNESS, R., CHEN, R., LIU, J., KUUSNIEMI, H., CHEN, Y., CHEN, L. & KAISTINEN, J. 2013. Human behavior cognition using smartphone sensors. *Sensors*, 13, 1402-1424.

PEI, L., LIU, J., GUINNESS, R., CHEN, Y., KUUSNIEMI, H. & CHEN, R. 2012. Using LS-SVM based motion recognition for smartphone indoor wireless positioning. *Sensors*, 12, 6155-6175.

PERŠ, J., KRISTAN, M. & KOVACIĆ, S. Fusion of non-visual modalities into the probabilistic occupancy map framework for person localization. Distributed Smart Cameras (ICDSC), 2011 Fifth ACM/IEEE International Conference on, 2011. IEEE, 1-6.

PETERSON, B. B., KMIECIK, C., HARTNETT, R., THOMPSON, P. M., MENDOZA, J. & NGUYEN, H. 1998. Spread spectrum indoor geolocation. *Navigation*, 45, 97-102.

PETOVELLO, M. 2013. Estimation for Navigation. Department of Geomatics Engineering, University of Calgary, Calgary, Canada.

PICCARDI, M. Background subtraction techniques: a review. *Systems, man and cybernetics, 2004 IEEE international conference on*, 2004. IEEE, 3099-3104.

RADAELLI, L., MOSES, Y. & JENSEN, C. S. Using Cameras to Improve Wi-Fi Based Indoor Positioning. *International Symposium on Web and Wireless Geographical Information Systems*, 2014. Springer, 166-183.

RAPPAPORT, T. S. 1996. *Wireless communications: principles and practice*, Prentice Hall PTR New Jersey.

RICHTER, P., PENA-TORRES, A. & TOLEDANO-AYALA, M. A rigorous evaluation of Gaussian process models for WLAN fingerprinting. *Indoor Positioning and Indoor Navigation (IPIN), 2015 International Conference on*, 2015. IEEE, 1-10.

RUIZ, A. R. J., GRANJA, F. S., HONORATO, J. C. P. & ROSAS, J. I. G. 2012. Accurate Pedestrian Indoor Navigation by Tightly Coupling Foot-Mounted IMU and RFID Measurements. *IEEE TRANSACTIONS ON INSTRUMENTATION AND MEASUREMENT*, 61.

SCHMITT, S., ADLER, S. & KYAS, M. The effects of human body shadowing in RF-based indoor localization. *Indoor Positioning and Indoor Navigation (IPIN), 2014 International Conference on*, 2014. IEEE, 307-313.

SHIN, E.-H. 2006. *Estimation techniques for low-cost inertial navigation*, Library and Archives Canada= Bibliothèque et Archives Canada.

SKLAR, B. 1997. Rayleigh fading channels in mobile digital communication systems. I. Characterization. *IEEE Communications magazine*, 35, 136-146.

SMAILAGIC, A., SMALL, J. & SIEWIOREK, D. P. 2000. Determining user location for context aware computing through the use of a wireless LAN infrastructure. *Institute for Complex Engineered Systems Carnegie Mellon University, Pittsburgh, PA*, 15213.

SPASSO, I. 2007. *Algorithms for map-aided autonomous indoor pedestrian positioning and navigation*. Citeseer.

STAUFFER, C. & GRIMSON, W. E. L. Adaptive background mixture models for real-time tracking. *Computer Vision and Pattern Recognition*, 1999. IEEE Computer Society Conference on., 1999. IEEE.

STOICA, P. & MOSES, R. L. 1997. *Introduction to spectral analysis*, Prentice hall Upper Saddle River.

TANG, S., ANDRILUKA, M. & SCHIELE, B. 2014. Detection and tracking of occluded people. *International Journal of Computer Vision*, 110, 58-69.

TEKTRONIX, 2013. *Wi-Fi: Overview of the 802.11 Physical Layer and Transmitter Measurements Primer*, <http://info.tek.com/www-wi-fi-overview-of-the-physical-layer-and-transmitter-measurements-primer.html>, last accessed October 05, 2015.

THRUN, S., BURGARD, W. & FOX, D. 2005. *Probabilistic robotics*, MIT press.

VAN DEN BERGHE, S., WEYN, M., SPRUYT, V. & LEDDA, A. 2011. Fusing camera and Wi-Fi sensors for opportunistic localization. *Proc. UBICOMM*, 169-174.

VAN TREES, H. L. 2004. *Detection, estimation, and modulation theory, optimum array processing*, John Wiley & Sons.

WALDER, U. & BERNOULLI, T. Context-adaptive algorithms to improve indoor positioning with inertial sensors. Indoor Positioning and Indoor Navigation (IPIN), 2010 International Conference on, 2010. IEEE, 1-6.

WHITE, C. E., BERNSTEIN, D. & KORNHAUSER, A. L. 2000. Some map matching algorithms for personal navigation assistants. *Transportation research part c: emerging technologies*, 8, 91-108.

WREN, C. R., AZARBAYEJANI, A., DARRELL, T. & PENTLAND, A. P. 1997. Pfinder: Real-time tracking of the human body. *IEEE Transactions on pattern analysis and machine intelligence*, 19, 780-785.

WU, Z., THANGALI, A., SCLAROFF, S. & BETKE, M. Coupling detection and data association for multiple object tracking. Computer Vision and Pattern Recognition (CVPR), 2012 IEEE Conference on, 2012. IEEE, 1948-1955.

XIANG, Z., SONG, S., CHEN, J., WANG, H., HUANG, J. & GAO, X. 2004. A wireless LAN-based indoor positioning technology. *IBM Journal of research and development*, 48, 617-626.

XIAO, Z., WEN, H., MARKHAM, A. & TRIGONI, N. Lightweight map matching for indoor localisation using conditional random fields. Information Processing in Sensor Networks, IPSN-14 Proceedings of the 13th International Symposium on, 2014. IEEE, 131-142.

- YILMAZ, A., JAVED, O. & SHAH, M. 2006. Object tracking: A survey. *Acm computing surveys (CSUR)*, 38, 13.
- YU, F., JIANG, M., LIANG, J., QIN, X., HU, M., PENG, T. & HU, X. 2014. 5 G WiFi Signal-Based Indoor Localization System Using Cluster-Nearest Neighbor Algorithm. *International Journal of Distributed Sensor Networks*, 2014.
- ZANCA, G., ZORZI, F., ZANELLA, A. & ZORZI, M. Experimental comparison of RSSI-based localization algorithms for indoor wireless sensor networks. Proceedings of the workshop on Real-world wireless sensor networks, 2008. ACM, 1-5.
- ZHANG, L., LI, Y. & NEVATIA, R. Global data association for multi-object tracking using network flows. Computer Vision and Pattern Recognition, 2008. CVPR 2008. IEEE Conference on, 2008. IEEE, 1-8.
- ZHUANG, Y. 2015. *Integration of WiFi and MEMS Sensors for Indoor Navigation*. University of Calgary.

APPENDIX A: ANDROID APPLICATION FOR INDOOR POSITIONING

An android application, called AppNav, was developed for indoor positioning general purpose. The main feature of this application include collecting experimental data, recording reference points (RP) for generating reference solution, position solution display, etc. This appendix introduces the main features of the application. Since the main interest of using this application for this thesis is RSS data collection and positioning making use of the RSS measurements, attention will be paid to the RSS relevant features.

A.1 Overview of the AppNav Application

Figure A.1 shows the overview of the AppNav application and the main menu the application is shown in the top-left corner. Each component of the menu corresponds to a sub-interface of this application, and Figure A.2 shows the four main sub-interfaces, which are Google map interface, floor plan interface, measurement real-time display interfaces and application configuration interface. The Google map and floor plan interface are used to display the ultimate position solution. The measurement real-time display interface is used to show the RSS, accelerometer, gyroscope and magnetometer data in real time. The ‘Setting’ interface is used to receive input to configure application parameters. The configurable features includes the name of the output measurement file, the measurement sources used for positioning (e.g., Wi-Fi, Bluetooth, Wi-Fi and sensor integration, etc.) and the RPs in predefined test route which are used to generate a reference solution for kinematic track test.

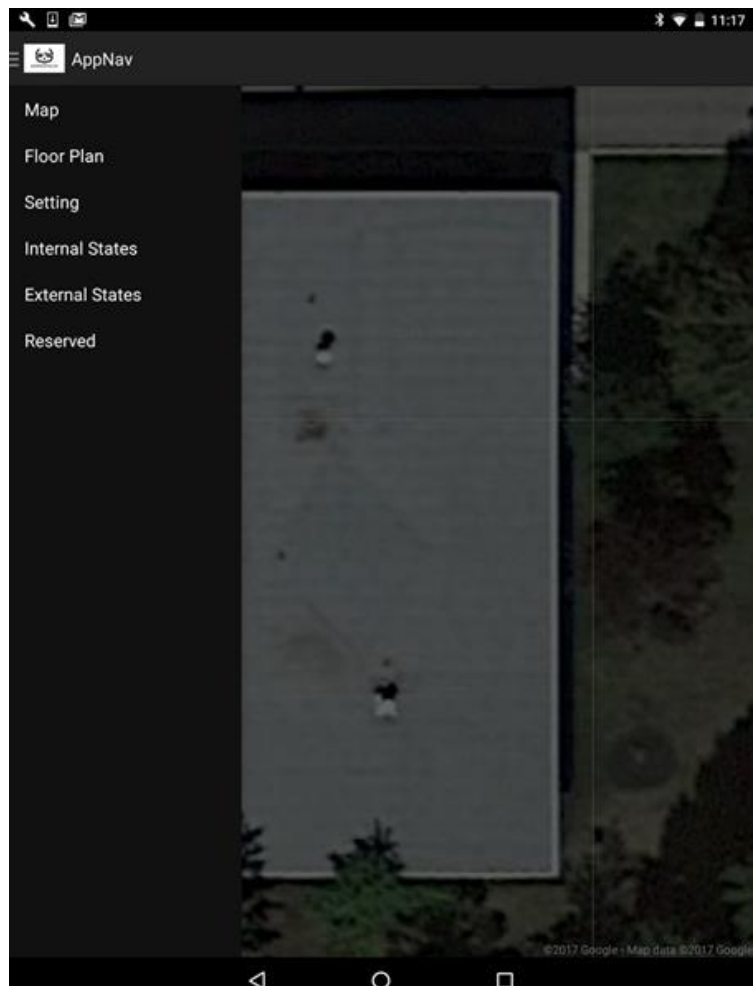


Figure A.1 Main menu of AppNav Android Application

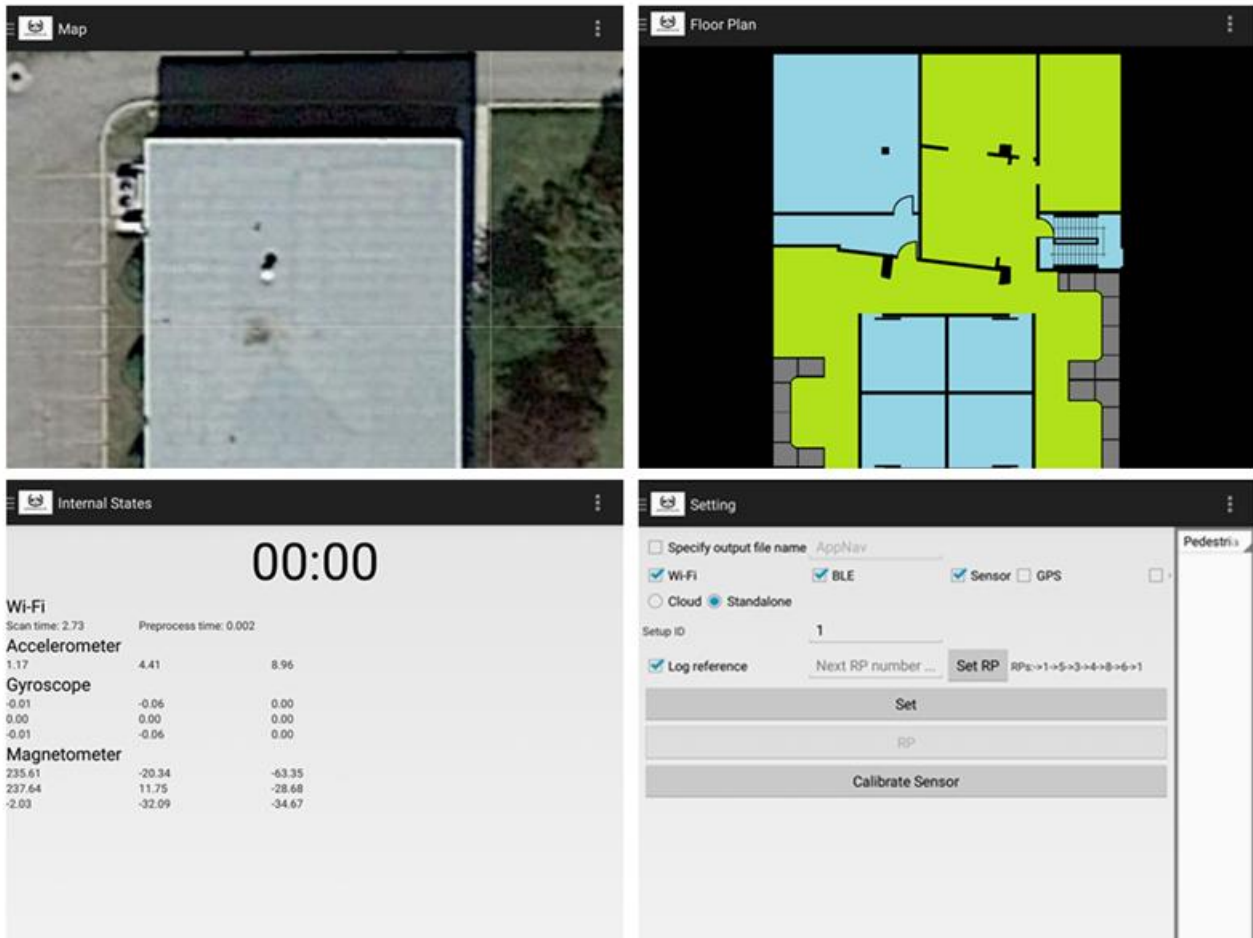


Figure A.2: Sub-interface of AppNav application: Google map (top-left), floor plan (top-right), measurement real-time display (bottom-left), setting interface (bottom-right)

A.2 AppNav Application for Wi-Fi RSS Data Collection

A user can hit the ‘Start’ bottom to start one data collection and the ‘Stop’ bottom to terminate it. Once the data collection starts, it scans beacon signals from APs that are in range with an interval depending on the Wi-Fi chipset of the device. This application is designed to scan the Wi-Fi beacon signal as fast as the Wi-Fi chipset can. The scan interval for the mobile device used in the thesis (Google Nexus 9 tablet) is about 0.7 s (i.e., 1.4 Hz RSS data rate). For each scan, the beacon signals from all the Wi-Fi APs in range are recorded, and the properties of interest (RSS,

BSSID, timestamp, SSID, frequency band) are stream to a file for post-processing. Figure A.3 shows an example of the recorded data, where the first column represents SSID, second column the BSSID, third column the timestamp, fourth column the RSS and fifth column the frequency band.

'ASUS_BEIHAI'	0862668DC438	1.8535e+10	-38	2437
'ASUS_5G_BEIHAI'	0862668DC43C	1.8535e+10	-49	5745
'WMac'	24A2E1EE9EFC	1.8535e+10	-77	2462
'eduroam'	04BD883B1983	1.8533e+10	-82	2462
'PPEREIRA'	9072401D6320	1.8535e+10	-83	2437
'TELUS3395'	4C8B30443155	1.8528e+10	-83	2437
'TELUS0733'	4C8B3028F8A5	1.8535e+10	-84	2412
'dlink'	0018E7E70584	1.8535e+10	-85	2412
'reزنet-secure'	04BD882750E2	1.8534e+10	-85	2412
'airuc'	04BD8822A600	1.8535e+10	-86	2412
'airuc-secure'	04BD8822A601	1.8535e+10	-86	2412
'eduroam'	04BD88245763	1.8535e+10	-87	2412
'airuc-guest'	04BD88245762	1.8535e+10	-87	2412
'HP-Print-AC-Officejet Pro 8610'	A02BB86B75AC	1.8534e+10	-88	2462
'DIRECT-9CC460 Series'	32CDA73182A2	1.8535e+10	-88	2462
'IDG-001'	28CFDAB7EEE5	1.8534e+10	-88	2412
'airuc'	04BD88400000	1.8534e+10	-88	2412
'airuc-secure'	04BD88245761	1.8535e+10	-88	2412
'eduroam'	04BD88261FA0	1.8528e+10	-89	2412
'HP000EB6'	02208092C58D	1.8535e+10	-89	2457
'airuc-guest'	04BD8822A602	1.8528e+10	-89	2412
'sid'	A839445D9730	1.8534e+10	-89	2412
'airuc-guest'	04BD88261FA1	1.8535e+10	-89	2412

Figure A.3: Example of recorded RSS measurements

For a kinematic track test, it is important to generate reference a solution for the field data collected. The AppNav application provides the user interface for generating such a solution. Prior to each track test, the RPs in the predefined route can be input and stored in the program through the ‘Setting’ interface as mentioned above. During the track test, every time the user

reach a RP and hit ‘RP’ button in the application, the RP and corresponding timestamp will be recorded. The reference solution then can be computed using the method discussed in Chapter 5.

APPENDIX B: CAMERA CALIBRATION FOR POSITIONING

To make use of static cameras for positioning, the objects detected on the pixel coordinate needs to be transformed to another coordinate system, e.g. a local level frame. This is done by camera calibration. In general, static camera calibration is the process of estimating the internal camera geometric parameters (intrinsic parameters) and position, orientation of camera frame relative to appropriate coordinates (extrinsic parameter). These parameters can be used to correct for lens distortion or determine the position of an object in the appropriate coordinates. This section describes some fundamentals of camera calibration.

Figure B.1 gives the coordinate system that need to be handled when calibrating a static camera.

- Local level frame, 3D coordinates denoted by $P_w = [E, N, U]$. It defines the positions of objects in the real world.
- Camera coordinates are denoted by $P_c = [X, Y, Z]$ where Z axis is the optic axis.
- Image plane (coordinates), 2D coordinates denoted by $[x, y]$. Forward projection onto the image plane. The Image plane is located f units out along the optic axis of the camera coordinate, as shown in Figure B.1.
- Pixel coordinates, 2D coordinate denoted by $[u, v]$ as shown in Figure B.1. A digital image is a 2D arrays. Each pixel is associated with $[u, v]$ coordinates representing its position within the image.

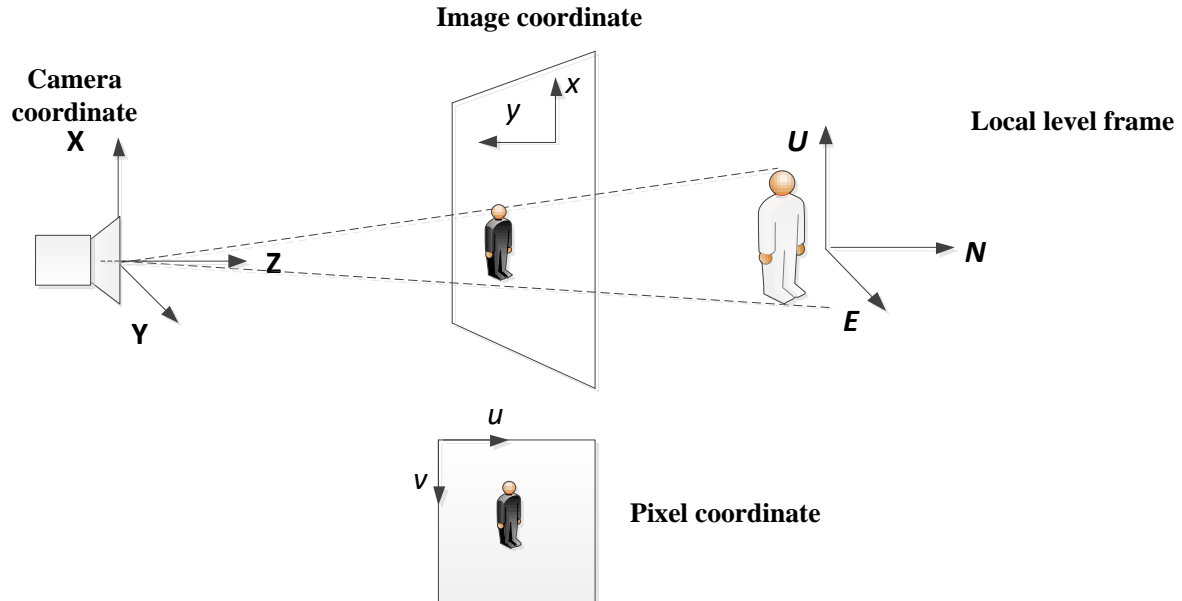


Figure B.1: Coordinate systems for static camera positioning

To derive the fundamental of camera calibration, a simple but useful model called a pinhole camera model can be used to start with. A pinhole is an imaginary wall with a tiny hole in the center, as depicted in Figure B.2. All the rays from the object are blocked by the pinhole plane except those passing through of tiny hole (Bradski and Kaehler, 2008). With this model, the transform between the camera and image coordinate can be derived from Figure B.2 as

$$\begin{aligned} x &= f \frac{X}{Z} \\ y &= f \frac{Y}{Z} \end{aligned} \tag{B.1}$$

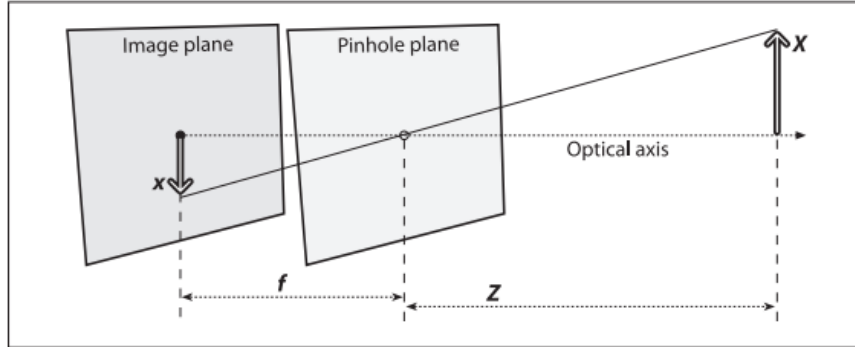


Figure B.2: Transform between camera coordinate and image coordinate (Bradski and Kaehler, 2008)

The transformation between camera and image coordinate is a 3D to 2D transformation and a homogeneous coordinate system is needed to represent (B.1) as a matrix equation, i.e., $[x, y]$ can be expressed as $[kx, ky, k]$ with non-zero k or simply $[x', y', z']$. Thus (B.1) can be written as:

$$\begin{bmatrix} x' \\ y' \\ z' \end{bmatrix} = \begin{bmatrix} f & 0 & 0 & 0 \\ 0 & f & 0 & 0 \\ 0 & 0 & 1 & 0 \end{bmatrix} \begin{bmatrix} X \\ Y \\ Z \\ 1 \end{bmatrix} \quad (\text{B.2})$$

The transformation between camera and local level frame can be represented by

$$P_C = \mathbf{R}(P_w - T) \quad (\text{B.3})$$

where \mathbf{R} is a 3×3 rotation matrix, and T a 3×1 translation vector (Bradski and Kaehler, 2008).

By denoting

$$\mathbf{R} = \begin{bmatrix} r_{11} & r_{12} & r_{13} \\ r_{21} & r_{22} & r_{23} \\ r_{31} & r_{32} & r_{33} \end{bmatrix} \quad (\text{B.4})$$

and

$$\mathbf{R}T = \begin{bmatrix} t_x \\ t_y \\ t_z \end{bmatrix} \quad (\text{B.5})$$

the transform between camera coordinate and local level frame in (B.3) can be expressed as

$$P_C = \begin{bmatrix} X \\ Y \\ Z \\ 1 \end{bmatrix} = \begin{bmatrix} r_{11} & r_{12} & r_{13} & t_x \\ r_{21} & r_{22} & r_{23} & t_y \\ r_{31} & r_{32} & r_{33} & t_z \\ 0 & 0 & 0 & 1 \end{bmatrix} \begin{bmatrix} U \\ V \\ W \\ 1 \end{bmatrix} = \begin{bmatrix} r_{11} & r_{12} & r_{13} & t_x \\ r_{21} & r_{22} & r_{23} & t_y \\ r_{31} & r_{32} & r_{33} & t_z \\ 0 & 0 & 0 & 1 \end{bmatrix} P_W \quad (\text{B.6})$$

The last transformation is between the image plane and the pixel coordinate system. Observe the relationship between the image plane and the pixel coordinates in Figure B.1, there are origin offset and a scale factor associated with them in both x and y directions, which can be expressed as

$$\begin{aligned} u &= \frac{x}{s_x} + o_x \\ v &= \frac{y}{s_y} + o_y \end{aligned} \quad (\text{B.7})$$

where $[o_x, o_y]$ is the offset of the origins of the two coordinate system, and s_x the scale factor:

$$\begin{bmatrix} x' \\ y' \\ z' \end{bmatrix} = \begin{bmatrix} \frac{f}{s_x} & 0 & o_x & 0 \\ 0 & \frac{f}{s_y} & o_y & 0 \\ 0 & 0 & 1 & 0 \end{bmatrix} \begin{bmatrix} X \\ Y \\ Z \\ 1 \end{bmatrix} \quad (\text{B.8})$$

By combining (B.2), (B.6) and (B.7), the transformation from the local level frame to pixel coordinate is established as:

$$\begin{bmatrix} u \\ v \\ 1 \end{bmatrix} = \begin{bmatrix} \frac{1}{s_x} & 0 & o_x \\ 0 & \frac{1}{s_y} & o_z \\ 0 & 0 & 1 \end{bmatrix} \begin{bmatrix} f & 0 & 0 & 0 \\ 0 & f & 0 & 0 \\ 0 & 0 & 1 & 0 \end{bmatrix} \begin{bmatrix} r_{11} & r_{12} & r_{13} & t_x \\ r_{21} & r_{22} & r_{23} & t_y \\ r_{31} & r_{32} & r_{33} & t_z \\ 0 & 0 & 0 & 1 \end{bmatrix} \begin{bmatrix} U \\ V \\ W \\ 1 \end{bmatrix} \quad (B.9)$$

which is the fundamental equation of static camera calibration. However, this is based on the use of the ideal pinhole camera. In reality, a lens is used to take the image because it can gather more light than what a pinhole can do. However, a lens is not perfect due to manufacturing factors, e.g. the shape of lens, the assembly process of the camera as a whole (Bradski and Kaehler, 2008). Generally, lens distortion effects introduced in the camera system need to be handled in the camera calibration phase, which complicates the calibration process. The details of lens distortions and how they are handled in the camera calibration be found in (Bradski and Kaehler, 2008). (B.10) expresses the essential calibration considering lens distortions.

$$\begin{bmatrix} u \\ v \\ 1 \end{bmatrix} = \underbrace{\begin{bmatrix} \frac{1}{s_x} & 0 & o_x \\ 0 & \frac{1}{s_y} & o_z \\ 0 & 0 & 1 \end{bmatrix}}_{\text{Intrinsic}} \underbrace{\begin{bmatrix} f_x & \alpha_c f_x & c_x & 0 \\ 0 & f_y & c_y & 0 \\ 0 & 0 & 1 & 0 \end{bmatrix}}_{\text{extrinsic}} \begin{bmatrix} r_{11} & r_{12} & r_{13} & t_x \\ r_{21} & r_{22} & r_{23} & t_y \\ r_{31} & r_{32} & r_{33} & t_z \\ 0 & 0 & 0 & 1 \end{bmatrix} \begin{bmatrix} U \\ V \\ W \\ 1 \end{bmatrix} \quad (B.10)$$

where f_x and f_y are the focal length in x and y , $[c_x, c_y]$ are the principal point coordinates and α_c the skew coefficient. The details of these parameters can be found in (Bradski and Kaehler, 2008). In general, the parameters in the first two matrices on the right-hand side of (B.10) describe the internal camera geometry and lens characteristics, which are referred to as camera

intrinsic parameters. The parameters in the third matrix describe the rotation and translation between the camera and local level frame, which are referred to as camera extrinsic parameters.